



# 1 Predicting the global temperature with the Stochastic Seasonal 2 to Interannual Prediction System (StocSIPS)

3 Lenin Del Rio Amador<sup>1</sup> · Shaun Lovejoy<sup>1</sup>

4 Received: 25 July 2018 / Accepted: 25 April 2019  
5 © Springer-Verlag GmbH Germany, part of Springer Nature 2019

## 6 Abstract

7 Many atmospheric fields—in particular the temperature—respect statistical symmetries that characterize the macroweather  
8 regime, i.e. time-scales between the  $\approx 10$  day lifetime of planetary sized structures and the (currently) 10–20 year scale at  
9 which the anthropogenic forcings begin to dominate the natural variability. The scale-invariance and the low intermittency of  
10 the fluctuations implies the existence of a huge memory in the system that can be exploited for macroweather forecasts using  
11 well-established (Gaussian) techniques. The Stochastic Seasonal to Interannual Prediction System (StocSIPS) is a stochastic  
12 model that exploits these symmetries to perform long-term forecasts. StocSIPS includes the previous ScaLIng Macroweather  
13 Model (SLIMM) as a core model for the prediction of the natural variability component of the temperature field. Here we  
14 present the theory for improving SLIMM using discrete-in-time fractional Gaussian noise processes to obtain an optimal  
15 predictor as a linear combination of past data. We apply StocSIPS to the prediction of globally-averaged temperature and  
16 confirm the applicability of the model with statistical testing of the hypothesis and a good agreement between the hindcast  
17 skill scores and the theoretical predictions. Finally, we compare StocSIPS with the Canadian Seasonal to Interannual Predic-  
18 tion System. From a forecast point of view, GCMs can be seen as an initial value problem for generating many “stochastic”  
19 realizations of the state of the atmosphere, while StocSIPS is effectively a past value problem that estimates the most probable  
20 future state from long series of past data. The results validate StocSIPS as a good alternative and a complementary approach  
21 to conventional numerical models. Temperature forecasts using StocSIPS are published on a regular basis in the website:  
22 <http://www.physics.mcgill.ca/StocSIPS/>.

## 23 1 Introduction

24 When taken beyond their deterministic predictability limits  
25 of about ten days, the output of General Circulation Models  
26 (GCMs) can no longer be usefully interpreted in a deter-  
27 ministic sense; they are at least implicitly stochastic and if  
28 they use stochastic parameterizations, they are explicitly  
29 so. In this “macroweather” regime, successive fluctuations  
30 tend to cancel each other out so that in control run mode,  
31 each GCM converges ultra slowly (Lovejoy et al. 2013) to its  
32 own climate. Assuming ergodicity, the control run climate  
33 is deterministic because it is the long-time average climate  
34 state, but the fluctuations about this state are stochastic.

35 Although each GCM climate may be different—and dif-  
36 ferent from that of the real world—various studies (see e.g.

the review (Lovejoy et al. 2018)) have indicated that the  
37 space–time statistics of fluctuations about the climates are  
38 statistically realistic—that they are of roughly the same type  
39 as the fluctuations observed in the real climate about the  
40 real climate state. For example, over wide ranges, and with  
41 realistic exponents, they exhibit scaling in both space and  
42 in time and at least approximately, they obey a symmetry  
43 called “statistical space–time factorization” (Lovejoy and de  
44 Lima 2015) that relates space and time. This suggests that  
45 the main defect of GCMs is that their fluctuations are around  
46 unrealistic model climates.

47 Many different stochastic processes can yield identi-  
48 cal statistics. This leads to the possibility—developed in  
49 (Lovejoy et al. 2015)—that a simple model, having the  
50 same space–time statistical symmetries as the GCMs and  
51 the real world, could be used to directly model temperature  
52 fluctuations. If in such a model, the long term behaviour  
53 and the statistics of the fluctuations are forced to match that  
54 of real-world data in the past, the model would thus com-  
55 bine realistic fluctuations with a realistic climate, leading to  
56

A1 ✉ Lenin Del Rio Amador  
A2 delrio@physics.mcgill.ca

A3 <sup>1</sup> Physics, McGill University, 3600 University St., Montreal,  
A4 QC H3A 2T8, Canada

significantly improved forecasts. Indeed, using this ScaLIng Macroweather Model (SLIMM), (Lovejoy 2015) gave some evidence for this by accurately forecasting the slow-down in the warming after 1998.

Starting with (Hasselmann 1976), various stochastic macroweather and climate models have been proposed. Today, these approaches are generally known under the rubric Linear Inverse Modelling (LIM), e.g.: (Penland and Matrosova 1994; Penland and Sardeshmukh 1995; Winkler et al. 2001; Newman et al. 2003; Sardeshmukh and Sura 2009). However, they all are based on integer order (stochastic) differential equations and these implicitly assume the existence of characteristic time scales associated with exponential decorrelation times; such models are not compatible with the scaling. To obtain models that respect the scaling symmetry, we may use fractional differential equations that involve strong, long-range memories; it is these long-range memories that are exploited in SLIMM forecasts. From a mathematical point of view, the fractional differential operators are of Weyl type (convolutions from the infinite past) so that they are not initial value problems, but rather past value problems.

In this paper we present the new Stochastic Seasonal to Interannual Prediction System (StocSIPS), that includes SLIMM as the core model to forecast the natural variability component of the temperature field, but also represents a more general framework for modelling the seasonality and the anthropogenic trend and the possible inclusion of other atmospheric fields at different temporal and spatial resolutions. In this sense, StocSIPS is the general system and SLIMM is the main part of it dedicated to the modelling of the stationary scaling series. The original technique that was used to make the SLIMM forecasts was basically correct, but it made several approximations (such as that the amount of data available for the forecast was infinite) and it was numerically cumbersome. Here, for the developing of StocSIPS, we return to it using improved mathematical and numerical techniques and validate them on ten different global temperature series since 1880 (five globally-averaged temperature series and five land surface average temperature). We then compare hindcasts with Canada's operational long-range forecast system, the Canadian Seasonal to Interannual Prediction System (CanSIPS) and we show that StocSIPS is just as accurate for 1-month forecasts, but significantly more accurate for longer lead times.

## 2 Theoretical framework

### 2.1 SLIMM

Since the works of (Hasselmann 1976), there have been many stochastic climate theories based on the idea that the high-frequency weather drives the low-frequency climate as

a stochastic forcing [for a review, see Franzke et al. (2014)]. The first and simplest approaches for solving the stochastic climate differential equations deduced from these theories were made through linear inverse models (LIM). The theoretical justification of LIM methods is based on extracting the intrinsic linear dynamics that govern the climatology of a complex system directly from observations of the system (inverse approach). However, they implicitly assume exponential decorrelations in time, whereas both the underlying Navier–Stokes equations (and hence models, GCMs) and empirical analyses respect statistical scaling symmetries [see the review in Lovejoy and Schertzer (2013)]. Due to this lack of solid physical basis, LIM approaches are referred to as “empirical approaches”. Nevertheless, its use is justified as a simpler alternative to the difficult task of improving numerical model parameterizations by appealing to physical arguments and first-principle reasoning alone.

Exponential decorrelations assumed by LIM models imply a scale break in time and—ignoring the diurnal and annual cycles—the only strong scale break is at the weather-macroweather transition scale of  $\tau_w \approx 5\text{--}15$  days (slightly varying according to location (especially latitude and land versus ocean), and also with slight variations from one atmospheric field to another. For the temperature, there is a transition in the spectrum at  $\omega \sim \omega_w \approx 1/\tau_w$ , with two different asymptotic behaviors for very high and very low frequencies [see Fig. 4 in Lovejoy and Schertzer (2012)]. Empirically we find that  $E_T(\omega) \sim \omega^{-\beta}$  with,  $\beta_h = 1.8$  ( $\omega > \omega_w$ ) and  $\beta_l \approx 0.2\text{--}0.8$  ( $\omega < \omega_w$ ) (depending on the location). The integer order differential equation for the LIM model implies that  $\beta_h = 2$  and  $\beta_l = 0$  (exactly, everywhere). Note that  $\beta_h$  is the value for a turbulent system, it corresponds to a highly intermittent process, not a process that is close to the integral of white noise (i.e. an Ornstein–Uhlenbeck process). LIM's exactly flat spectral behavior at low frequencies is a consequence of the fact that the highest order differential term is integer ordered, it implies that the low frequencies are (unpredictable) white noise. For times much larger than the decorrelation time, temperature forecasts have no skill. LIM's short memory behavior can be modeled as a Markov process, equivalently as an autoregressive or moving average process.

There are many empirical results that show a non-flat scaling behavior in the temperature spectrum (as well as in many other atmospheric variables) with values for  $\beta_l$  from 0.2 to 0.8 [see the review in Lovejoy and Schertzer (2013), also Lovejoy et al. (2018)]. This power-law behavior in the spectrum (and in the autocorrelation function) reflects the long-range memory that must be modelled. To appreciate the importance of the value of  $\beta_l$  for Gaussian processes, when  $\beta_l = 0$ , there is no predictability, and when  $\beta_l = 1$ , there is infinite predictability. The long memory effects mean that the equations become non-Markovian and that

159 also past states need to be considered in order to predict  
 160 the behavior of the system. The generalization of LIM's  
 161 integer ordered differential equations to include fractional  
 162 order derivatives already introduces power-law correlations,  
 163 the simplest option being to retain the simplest (Gaussian)  
 164 assumption about the noise forcing. This is the main idea  
 165 behind the ScaLIng Macroweather Model (SLIMM) (Love-  
 166 joy et al. 2015).

167 In the macroweather regime intermittency is generally  
 168 low enough that a Gaussian model with long-range statistical  
 169 dependency is a workable approximation [except perhaps for  
 170 the extremes; e.g. the review (Lovejoy et al. 2018)]. Some  
 171 attempts have been made to use Gaussian models for pre-  
 172 diction in the mean square prediction framework of autore-  
 173 gressive fractional integrated moving average (ARFIMA)  
 174 processes (Baillie and Chung 2002; Yuan et al. 2015). The  
 175 theory behind some of these models only applies to station-  
 176 ary series, while, for example, in the case of globally-aver-  
 177 aged temperature time series, there is clearly an increasing  
 178 trend due to the anthropogenic warming in recent decades. If  
 179 the trend is not properly removed, the assumption of random  
 180 equally distributed variables no longer applies, and the skill  
 181 of the predictions is adversely affected. The ScaLIng Mac-  
 182 roweather Model (SLIMM), (Lovejoy et al. 2015) was the  
 183 first of such models that took all these facts into considera-  
 184 tion and offered a complete evaluation of the prediction skill  
 185 based on hindcasts after the removal of the anthropogenic  
 186 warming part.

187 SLIMM is a model for the prediction of stationary series  
 188 with Gaussian statistics and scaling symmetry of the fluctu-  
 189 ations. It proposes a predictor as a linear combination of  
 190 past data (or past innovations). For the case of Gaussian  
 191 variables, it has been proven that this kind of linear predic-  
 192 tor is optimal in the mean square error sense [see the "Fun-  
 193 damental note" in page 264 of Papoulis and Pillai (2002)].  
 194 That is, if any other functional form (i.e. nonlinear) is used  
 195 to build a predictor based on past data, the mean square  
 196 error of the predictions will be larger than with the linear  
 197 combination. This is not necessarily true if the distribution  
 198 of the variables is not Gaussian, for example, in the case of  
 199 multifractal processes, where the second moment statistics  
 200 are not sufficient to describe the process.

201 Similarly to the spectrum where  $E_T(\omega) \sim \omega^{-\beta}$ , in the  
 202 macroweather regime the average of the fluctuations as a  
 203 function of the time scale also presents a power-law (scal-  
 204 ing) behavior with  $\langle \Delta T(\Delta t) \rangle \sim \Delta t^H$ . Besides the scale-  
 205 invariance, low intermittency (rough Gaussianity) in time,  
 206 is another characteristic of the macroweather regime. For  
 207 Gaussian processes, the spectrum and the fluctuation expo-  
 208 nents are related by  $H = (\beta_l - 1)/2$ . In Lovejoy et al. (2015)  
 209 SLIMM was introduced, based on fractional Gaussian noise

(fGn), as the simplest stochastic model that includes both  
 characteristics.

For their relevance to the current work, some properties  
 of fGn presented in that paper are summarized here; for an  
 extensive mathematical treatment see Biagini et al. (2008).

Over the range  $-1 < H < 0$ , an fGn process,  $G_H(t)$ , is  
 the solution of a fractional order stochastic differential  
 equation of order  $H + 1/2$ , driven by a unit Gaussian  $\delta$ -  
 correlated white noise process,  $\gamma(t)$ , (with  $\langle \gamma(t) \rangle = 0$  and  
 $\langle \gamma(t)\gamma(t') \rangle = \delta(t - t')$ , where  $\delta(t)$  is the Dirac function):

$$\frac{d^{H+1/2}G_H(t)}{dt^{H+1/2}} = c_H\gamma(t), \tag{1}$$

where:

$$c_H^2 = \frac{\pi}{2 \cos(\pi H)\Gamma(-2 - 2H)}, \tag{2}$$

and  $\Gamma(x)$  is the Euler gamma function. The value for the  
 constant  $c_H$  was the standard one chosen to make the expres-  
 sion for the statistics particularly simple, see below. The  
 fractional differential equation (Eq. (1)) was presented in  
 Lovejoy et al. (2015) as a generalization of the LIM inter-  
 ger order equation to account for the power-law behavior  
 observed for the spectrum at frequencies  $\omega > \omega_w \approx 1/\tau_w$ .  
 Physically it could model a scaling heat storage mechanism.

Integrating Eq. (1), we obtain:

$$G_H(t) = \frac{c_H}{\Gamma(H + 1/2)} \int_{-\infty}^t (t - t')^{-(1/2-H)} \gamma(t') dt'. \tag{3}$$

In other words,  $G_H(t)$  is the fractional integral of order  
 $H + 1/2$  of a white noise process, which can also be  
 regarded as a smoothing of a white noise with a power-  
 law filter. The process  $\gamma(t)$  is a particular case of  $G_H(t)$  for  
 $H = -1/2$ . Just as  $\gamma(t)$  is a generalized stochastic process (a  
 distribution), the process  $G_H(t)$  is also a generalized func-  
 tion without point-wise values. It is the density of the well-  
 known fractional Brownian motion (fBm) measures,  $B_{H'}(t)$ ,  
 with  $H' = H + 1$ , i.e.  $dB_{H'}(t) = G_H(t)dt$  (Wiener integrals for  
 the case  $H' = 1/2$ ). The derivative of a distribution (in this  
 case  $B_{H'}(t)$ ) is formally defined from the following:

$$\int \varphi(t)dB_{H'}(t) = \int \varphi(t)G_H(t)dt = - \int \varphi'(t)B_{H'}(t)dt, \tag{4}$$

where  $\varphi(t)$  is any locally integrable function.

From this relation to fBm, the resolution  $\tau$  (smallest sam-  
 pling temporal scale) fGn process,  $G_{H,\tau}(t)$ , can be defined,  
 either as an average of  $G_H(t)$ , or from the increments of the  
 fBm process,  $B_{H'}(t)$ , at the same resolution:

250

$$G_{H,\tau}(t) = \frac{1}{\tau} \int_{t-\tau}^t G_H(t') dt' = \frac{1}{\tau} \int_{t-\tau}^t dB_{H'}(t') = \frac{1}{\tau} [B_{H'}(t) - B_{H'}(t-\tau)]. \tag{5}$$

251 In Lovejoy et al. (2015) it was shown that, for resolution  
252  $\tau > \tau_w$ , we can model the globally-averaged macroweather  
253 temperature as:

$$254 T_\tau(t) = \sigma_T G_{H,\tau}(t), \tag{6}$$

255 where  $-1 < H < 0$  and  $\sigma_T$  is the temperature variance (for  
256  $\tau = 1$ ). The parameter  $H$ , defined in this range, is not the  
257 more commonly used Hurst exponent for fBm processes,  $H'$ ,  
258 but the fluctuation exponent of the corresponding fractional  
259 Gaussian noise process. Fluctuations exponents are used  
260 due to their wider generality; they are well defined even for  
261 strongly non-Gaussian processes. For a discussion see page  
262 643 in (Lovejoy et al. 2015).

263 Assuming  $\tau$  is the smallest scale in our system with the  
264 property  $\tau > \tau_w$  (e.g.  $\tau = 1$  month for air temperature), the  
265 temperature defined by Eq. (6) has the following properties:

- 266 (i)  $T_\tau(t)$  is a Gaussian stationary process with continuous paths.
- (ii)  $\langle T_\tau(t) \rangle = 0$  and  $\langle T_\tau(t)^2 \rangle = \sigma_T^2 \tau^{2H}$ ; for all  $t$ , the notation  $\langle \cdot \rangle$   
denotes ensemble (infinite realizations) averaging.

$$\begin{aligned} \text{(iii) } C_{H,\sigma_T}(\Delta t) &= \langle T_\tau(t) T_\tau(t + \Delta t) \rangle \\ &= \frac{\sigma_T^2}{2\tau^2} (|\Delta t + \tau|^{2H+2} + |\Delta t - \tau|^{2H+2} - 2|\Delta t|^{2H+2}); \end{aligned} \tag{7}$$

for  $\Delta t \geq \tau$ .

267 For more details see Mandelbrot and Van Ness (1968),  
268 Gripenberg and Norros (1996) and Biagini et al. (2008).

269 From Eq. (7.iii), the behavior of the autocovariance function  
270 for  $\Delta t \gg \tau$  and  $-1 < H < 0$  is:

$$271 C_{H,\sigma_T}(\Delta t) \approx \sigma_T^2 (H + 1)(2H + 1) \Delta t^{2H} \tag{8}$$

272 and the corresponding spectrum for low frequencies is:

$$273 E_T(\omega) \approx \Gamma(3 + 2H) \sin(\pi H) \omega^{-\beta_l} / \sqrt{2\pi}, \tag{9}$$

274 where  $\beta_l = 1 + 2H$ .

275 Combining Eqs. (3), (5) and (6), we get the following  
276 explicit integral expression for the temperature at resolu-  
277 tion  $\tau$ :

$$278 T_\tau(t) = \frac{1}{\tau} \frac{c_H \sigma_T}{\Gamma(H + 3/2)} \left[ \int_{-\infty}^t (t-t')^{H+1/2} \gamma(t') dt' - \int_{-\infty}^{t-\tau} (t-\tau-t')^{H+1/2} \gamma(t') dt' \right]. \tag{10}$$

279 Notice that  $T_\tau(t)$  is obtained from the difference of frac-  
280 tional integrals of order  $H + 3/2$  of a white noise process.  
281 Our definition of  $c_H$  in Eq. (2) implies that  $\langle T_\tau(t)^2 \rangle = \sigma_T^2 \tau^{2H}$ .  
282 As  $H < 0$ , it follows that, in the small-scale limit ( $\tau \rightarrow 0$ ),  
283 the variance diverges and  $H$  is the scaling exponent of the  
284 root mean square (RMS) value. This singular small-scale  
285 behavior is responsible for the strong power-law resolution  
286 effects in fGn. For a detailed discussion on this important  
287 resolution effect that leads to a “space–time reduction fac-  
288 tor” and its implications for the accuracy of global surface  
289 temperature datasets, see Lovejoy (2017).

290 Using the fact that  $T_\tau(t)$  is a Gaussian stationary process,  
291 Lovejoy et al. (2015) derived a formula for the predictor  
292 of the temperature at some time  $t \geq \tau$ , given that data are  
293 available over the entire past (i.e. from  $t = -\infty$  to 0). From  
294 Eq. (10), the mean square (MS) estimator for the tempera-  
295 ture can be expressed as:

$$296 \hat{T}_\tau(t) = \frac{1}{\tau} \frac{c_H \sigma_T}{\Gamma(H + 3/2)} \int_{-\infty}^0 [(t-t')^{H+1/2} - (t-\tau-t')^{H+1/2}] \gamma(t') dt'. \tag{11}$$

297 As a measure of the skill of the model, we can use the  
298 mean square skill score (MSSS), defined as:

$$299 \text{MSSS}(t, \tau) = 1 - \frac{\langle [T_\tau(t) - \hat{T}_\tau(t)]^2 \rangle}{\langle T_\tau(t)^2 \rangle}, \tag{12}$$

300 i.e. one minus the normalized mean square error (MSE).  
301 Here  $T_\tau(t)$  represents the verification and  $\hat{T}_\tau(t)$  the forecast  
302 at time  $t \geq \tau$ . The reference forecast would be the average  
303 of the series  $\langle T_\tau(t) \rangle = 0$ , for which the MSE is the variance  
304  $\langle T_\tau(t)^2 \rangle$ . Using Eqs. (10) and (11) in (12), an analytical  
305 expression for the MSSS can be obtained:

$$306 \text{MSSS}_H(t/\tau) = \frac{F_H(\infty) - F_H(t/\tau)}{F_H(\infty) + \frac{1}{2H+2}}, \tag{13}$$

where  $t \geq \tau$  and

$$307 F_H(t) = \int_0^{t-1} ((1+u)^{H+1/2} - u^{H+1/2})^2 du, \tag{14}$$

309 in particular,

$$310 F_H(\infty) = \frac{\Gamma(3/2 + H)\Gamma(-2H)}{(2H + 2)\Gamma(1/2 - H)} - \frac{1}{2H + 2}. \tag{15}$$

311 Although Eq. (11) is the formal expression for the pre-  
312 dictor of the temperature, from a practical point of view it  
313 has two clear disadvantages: it is expressed as an integral  
314 of the unknown past innovations,  $\gamma(t)$ , and it assumes the  
315 knowledge of these innovations for an infinite time in the



316 past. It would be more natural to express the predictor as a  
 317 function of the observed part of the process. This problem  
 318 was solved for fBm processes with  $1/2 < H' < 1$  (equiva-  
 319 lently  $-1/2 < H < 0$ ) by Gripenberg and Norros (1996).  
 320 The explicit formula they found for the predictor,  $\hat{B}_{H',a}(t)$ ,  
 321 of the fBm process,  $B_{H'}(t)$ , known in the interval  $(-a, 0)$  for  
 322  $t > 0$  and  $a > 0$ , is:

$$323 \hat{B}_{H',a}(t) = \int_{-a}^0 g_a(t, t') B_{H'}(t') dt', \quad (16)$$

324 where  $g_a(t, t')$  is an appropriate weight function given by:

$$325 g_a(t, -t') = \frac{\sin[\pi(H' - 1/2)]}{\pi} [t'(a - t')]^{-H'+1/2} \\ 326 \int_0^t \frac{[x(x+a)]^{H'-1/2}}{x+t'} dx. \quad (17)$$

326 It is important to note that the weight function goes to  
 327 infinity both at the origin and at  $-a$  [see Fig. 8 in Norros  
 328 (1995)]. In their words, this divergence when we approach  
 329  $-a$  is because “the closest witnesses to the unobserved past  
 330 have special weight”.

331 The results summarized in Eqs. (10–17) are theoretically  
 332 important, but, from the practical point of view of mak-  
 333 ing predictions, a discrete representation of the process is  
 334 needed. In the next sections, we present analogous results for  
 335 the prediction of discrete-in-time, finite past fGn processes  
 336 and its application to the modelling and prediction of global  
 337 temperature time series.

## 338 2.2 StocSIPS

339 The theory presented in the previous section and the appli-  
 340 cability of SLIMM is restricted to detrended time series with  
 341 Gaussian statistics and a scaling behavior of the fluctuations.  
 342 Real-world datasets, in particular raw temperature series,  
 343 normally include periodic signals corresponding to the diur-  
 344 nal and the seasonal cycles. They are also affected by an  
 345 increasing trend as a response to anthropogenic forcing and  
 346 usually combine different scaling regimes depending on the  
 347 temporal resolution used.

348 StocSIPS is the general system that includes SLIMM as  
 349 the core model for the long-term prediction of atmospheric  
 350 fields. In order to use SLIMM, some of the components of  
 351 StocSIPS are dedicated to the “cleaning” of the original  
 352 dataset. In particular, it includes techniques for removing  
 353 and projecting the seasonality and the anthropogenic trend.  
 354 It also degrades the temporal series to a scale where only one  
 355 scaling regime with fluctuation exponent  $-1/2 < H < 0$  is  
 356 present. The initial goal is to produce a temporal series that

357 can be modelled and predicted with the stationary fGn pro-  
 358 cess using the SLIMM theory. Some other aspects of Stoc-  
 359 SIPS—not discussed in this paper—include the addition of  
 360 another space–time symmetry [the statistical space–time  
 361 factorization (Lovejoy and de Lima 2015; Lovejoy et al.  
 362 2018)] for the regional prediction, and the combination as  
 363 copredictors of different atmospheric fields.

364 One of the objectives of this paper is to show the improve-  
 365 ments in the theoretical treatment and in the numerical meth-  
 366 ods of SLIMM as an essential part of StocSIPS. These recent  
 367 developments have helped to produce faster and more accu-  
 368 rate predictions of global temperature. The improvement  
 369 in SLIMM and some of the preprocessing techniques are  
 370 illustrated later on in Sect. 3 through an application to the  
 371 forecast of globally-averaged temperature series.

### 372 2.2.1 Discrete-in-time fGn processes

373 As we showed in Sect. 2.1, for predicting the stationary com-  
 374 ponent of the temperature with resolution  $\tau$  at a future time  
 375  $t > 0$ , the linear predictor,  $\hat{T}_\tau(t)$ , based on past data ( $T_\tau(s)$   
 376 for  $-a < s \leq 0$ ) satisfying the minimum mean square error  
 377 condition (orthogonality principle between the error and the  
 378 data) can then be written as:

$$379 \hat{T}_\tau(t) = \int_{-a}^0 M_T(t, s) T_\tau(s) ds, \quad (18)$$

or equivalently, based on the past innovations,  $\gamma(s)$ :

$$381 \hat{T}_\tau(t) = \int_{-a}^0 M_Y(t, s) \gamma(s) ds, \quad (19)$$

382 where  $M_T(t, s)$  and  $M_Y(t, s)$  are appropriated weight  
 383 functions. In SLIMM, the predictor given by Eq. (11)  
 384 is a particular case of Eq. (19) for  $a = \infty$  and  
 385  $M_Y(t, s) = c_H \sigma_T [(t - s)^{H+1/2} - (t - \tau - s)^{H+1/2}] / \tau \Gamma(H + 3/2)$ ,  
 386 while the solution in Gripenberg and Norros (1996) (Eq. (16)  
 387 here) is the case of Eq. (18) for an fBm process with  $M_T(t, s)$   
 388 analogous to  $g_a(t, t')$  given by Eq. (17).

389 The mathematical theory presented in Sect. 2.1 is gen-  
 390 eral for a continuous-in-time fGn. Moreover, the integral  
 391 representation of fGn given by Eq. (10), is based on an infi-  
 392 nite past of continuous innovations,  $\gamma(t)$ . For applications to  
 393 real-world data, a discrete version of the problem is needed  
 394 for the case of fGn with finite data in the past ( $a < \infty$ ). In  
 395 practice, in the case of temperature (and any other atmos-  
 396 pheric field) we only have measurements at discrete times  
 397 with some resolution over a limited period. For modeling  
 398 these fields, we can consider discrete-in-time fGn process  
 399 as a more suitable model.

Assuming that we have already removed the low-frequency anthropogenic component of the temperature series (see Sect. 3.2), in the discrete case, we could express the zero mean detrended component by its moving average (MA( $\infty$ )) stochastic representation given by the Wold representation theorem (Wold 1938):

$$T_t = \sum_{j=-\infty}^t \varphi_{t-j} \gamma_j, \quad (20)$$

where  $\{\varphi_t\}$  are weight parameters with units of temperature and  $\{\gamma_t\}$  is a white noise sequence with  $\gamma_t \sim \text{NID}(0, 1)$  and  $\gamma_i \gamma_j = \delta_{ij}$ , where  $\delta_{ij}$  is the Kronecker delta and  $\text{NID}(\mu, \sigma^2)$  stands for normally and independently distributed with mean  $\mu$  and variance  $\sigma^2$  (the sign  $\sim$  means equal in distribution). This equation is analogous to Eq. (10) for the continuous case.

By inverting Eq. (20) we can obtain the equivalent autoregressive (AR( $\infty$ )) representation (Palma 2007):

$$T_t = \sigma_0 \gamma_t + \sum_{j=-\infty}^{t-1} \pi_{t-j} T_j, \quad (21)$$

which is more suitable for predictions, as any value of the series is given as a linear combination of the values in the past. In this representation the weights  $\{\pi_t\}$  are unitless.

In practice, we only have a finite stretch of data  $\{T_{-t}, \dots, T_0\}$ . Under this circumstance, the optimal  $k$ -steps Wiener predictor for  $T_k$  ( $k > 0$ ), based on the finite past, is given by:

$$\hat{T}_t(k) = \sum_{j=-t}^0 \phi_{t,j}(k) T_j = \phi_{t,-t}(k) T_{-t} + \dots + \phi_{t,0}(k) T_0, \quad (22)$$

where the new vector of coefficients,  $\boldsymbol{\phi}_t(k) = [\phi_{t,-t}(k), \dots, \phi_{t,0}(k)]^T$  (the superscript  $T$  denotes transpose operation) satisfies the Yule-Walker equations [see page 96 in Hipel and McLeod (1994)]:

$$\mathbf{R}_{H,\sigma_T}^t \boldsymbol{\phi}_t(k) = \mathbf{C}_{H,\sigma_T}^t(k), \quad (23)$$

with  $\mathbf{C}_{H,\sigma_T}^t(k) = [C_{H,\sigma_T}(k-i)]_{i=-t,\dots,0}^T = [C_{H,\sigma_T}(t+k), \dots, C_{H,\sigma_T}(k)]^T$  and  $\mathbf{R}_{H,\sigma_T}^t = [C_{H,\sigma_T}(i-j)]_{i,j=-t,\dots,0}$  being the autocovariance matrix. The elements  $C_{H,\sigma_T}(\Delta t)$  are obtained from Eq. (7.iii) where we assume  $\tau = 1$  is the smallest scale in our system with the property  $\tau \gg \tau_w$  (e.g.  $\tau = 1$  month).

Notice that the coefficients  $\{\phi_{t,j}\}$  will only depend on  $H$  [ $\sigma_T$  cancels in both sides of Eq. (23)] and further that they are not the same as the coefficients  $\{\pi_t\}$ , for which the complete knowledge of the infinite past is assumed. The coefficients  $\{\pi_t\}$  decrease monotonically as we go further in the past, while this is not the case for the coefficients  $\{\phi_{t,j}\}$ , as we can see in Fig. 1 for the cases where

$H = -0.1, -0.25, -0.4$ , and we predict  $k = 12$  steps in the future by using a series of  $t + 1 = 36$  values. Notice how the memory effect (the weight of the coefficients) increases with the value of  $H$ . This behavior of the coefficients is analogous to the one mentioned earlier for the function  $g_a(t, t')$  (Eq. (17)). As found in Gripenberg and Norros (1996) for the continuous-in-time case, not only is there a strong weighting of the recent data, but the most ancient available data also have singular weights [compare Fig. 1 here with Fig. 3.1 in (Gripenberg and Norros 1996)].

This behavior of the coefficients for fGn is the main difference (and a clear advantage) over other autoregressive models (AR, ARMA) which do not include fractional integrations accounting for the long-term memory and do not consider the information from the distant past. An additional limitation of these approaches is that for each  $\Delta t$ , the values for  $C(\Delta t) = \langle T_\tau(t) T_\tau(t + \Delta t) \rangle$  must be estimated directly from the data. Each  $C(\Delta t)$  will have its own error, this effectively introduces a large “noise” in the predictor estimates. In addition, it is computationally expensive if a large number of coefficients are needed. In our fGn model the coefficients have an analytic expression which only depends on the fluctuation exponent,  $H$ , obtained directly from the data exploiting the scale-invariance symmetry of the fluctuations; our problem is a statistically highly constrained problem of parametric estimation ( $H$ ), not an unconstrained one (the entire  $C(\Delta t)$  function).

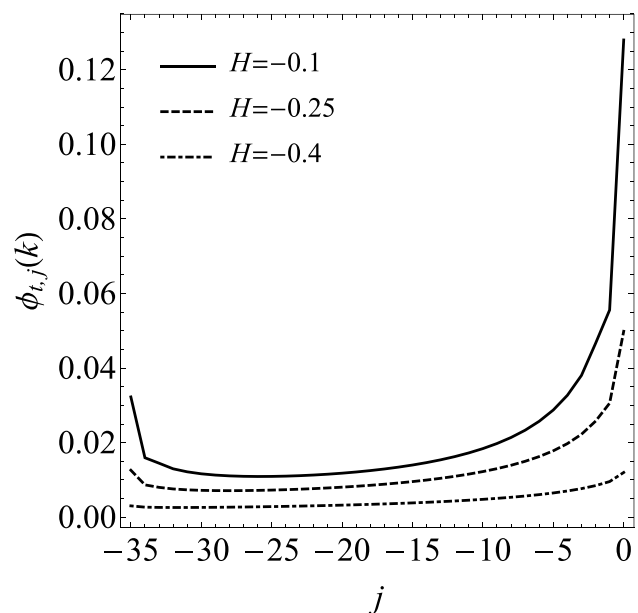


**Fig. 1** Optimal coefficients,  $\phi_{t,j}$ , in Eq. (17) with  $H = -0.1, -0.25, -0.4$  (top to bottom) for predicting  $k = 12$  steps in the future by using the data for  $j = -35, \dots, 0$  in the past. Notice the strong weighting on both the most recent (right) and the most ancient available data (left) and how the memory effect decreases with the value of  $H$ . Compare to Fig. 3.1 in Gripenberg and Norros (1996)

468 In the discrete case, the mean square skill score, defined  
 469 by Eq. (12), has the following analytical expression:

470 
$$\text{MSSS}'_H(k) = \tilde{\mathbf{C}}_H^t(k)^T (\tilde{\mathbf{R}}_H^t)^{-1} \tilde{\mathbf{C}}_H^t(k), \tag{24}$$

471 where  $\tilde{\mathbf{C}}_H^t(k) = [\tilde{C}_H(k-i)]_{i=-t, \dots, 0}^T$  is a vector formed by the  
 472 autocorrelation function  $\tilde{C}_H(\Delta t) = C_{H, \sigma_T}(\Delta t) / \sigma_T^2$  (see Eq. (7.  
 473 iii)) and  $\tilde{\mathbf{R}}_H^t = \mathbf{R}_{H, \sigma_T}^t / \sigma_T^2 = [\tilde{C}_H(i-j)]_{i,j=-t, \dots, 0}$  is the autocor-  
 474 relation matrix. For a given horizon in the future,  $k$ , the  
 475 MSSS will only depend on the exponent,  $H$ , and the exten-  
 476 sion of our series in the past,  $t$ .

477 In the previous equations, the full length of our known  
 478 series was  $t + 1$ , but we don't necessarily have to use the  
 479 complete series to build our predictor. It is enough to use  
 480 a number  $m + 1$  of points in the past (memory) with  $m < t$ .  
 481 The new predictor and skill score are obtained by just replac-  
 482 ing  $t$  by  $m$  in Eqs. (22–24). By doing this, we can use the  
 483 remaining  $t - m - 1$  points for hindcast verifications.

484 For the case where  $H = -0.25$  and  $k = 3$ , Fig. 2 shows  
 485 how the MSSS approaches the asymptotic value correspond-  
 486 ing to an infinite past as we increase the amount of memory  
 487 we use. The dashed line represents the MSSS for  $m = 500$   
 488 and the dotted line is the value we obtain using Eq. (13)  
 489 for the continuous-in-time case with the infinite past known.  
 490 The difference between the two is not due to the finite mem-  
 491 ory ( $m = 500$ ) we have in the discrete case with respect to  
 492 the infinite past assumed in Eq. (13), but to intrinsic dif-  
 493 ferences due to the discretization and more related to the

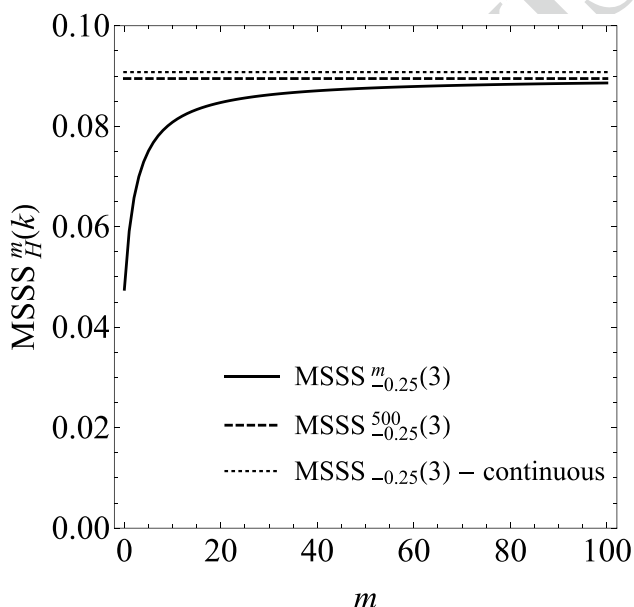


Fig. 2 MSSS<sup>m</sup><sub>H</sub>(k) as a function of the memory,  $m$ , for the case where  $H = -0.25$  and  $k = 3$ . The dashed line represents the MSSS for  $m = 500$  and the dotted line is the value obtained with Eq. (12) for the continuous-in-time case. For  $m = 22$ , more than 95% of the asymptotic skill is achieved

high-frequency information loss because of the smoothing  
 from a continuous to a discrete process. Note that we do  
 not need to use a large memory to achieve a skill close to  
 the asymptotic value. In this example where  $H = -0.25$ , we  
 only need to use  $m \geq 22$  for  $k = 3$  to get more than 95% of  
 the maximum skill.

The amount of memory needed depends on the value of  
 $H$ , as we can see in Fig. 3, where we plot the minimum  
 memory needed,  $m_{95\%}$ , to get more than 95% of the asymp-  
 totic value (corresponding to  $m = \infty$ ) as a function of the  
 horizon,  $k$ , for different values of  $H$ . The line  $m = 15k$  was  
 also included for reference. The larger the value of the expo-  
 nent,  $H$ , (the closer to zero) the less memory we need to  
 approach the maximum possible skill. This fact seems counter-  
 intuitive, but the explanation is simple: for larger values  
 of  $H$  (closer to zero), the influence of values farther in the  
 past is stronger, but at the same time, more information of  
 those values is included in the recent past, so less memory is  
 needed for forecasting. Following the rule of thumb found by  
 Norros (1995) for the continuous case: “one should predict  
 (...) the next second with the latest second, the next minute  
 with the latest minute, etc.” Actually, from Fig. 3 we can  
 conclude that, for predicting  $k$  steps into the future, a mem-  
 ory  $m = 15k$  would be a safe minimum value for achieving  
 almost the maximum possible skill for any value of  $H$  in the  
 range  $(-1/2, 0)$ , which is the case for temperature and many  
 other atmospheric fields. Of course, if  $H$  is close to zero a

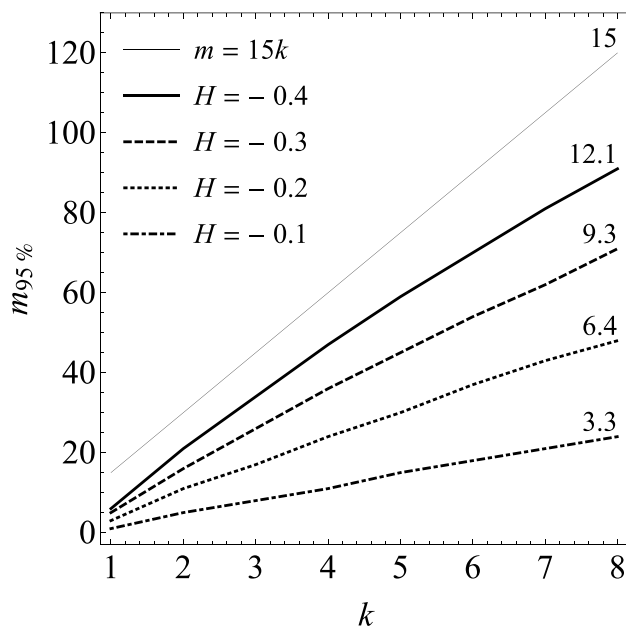


Fig. 3 Minimum memory,  $m$ , needed to get more than 95% of the asymptotic value (corresponding to  $m = \infty$ ) as a function of the horizon,  $k$ , for different values of  $H$ . The larger the value of  $H$  (the closer to zero) the less memory is needed for a given horizon. The approximate ratio  $m_{95\%}/k$  for each  $H$  was included at the top of the respective curve

much smaller value could be taken. The approximate ratio  $m_{95\%}/k$  for each  $H$  was included at the top of the respective curve. From the point of view of the availability of data for the predictions, this result is important. Once the value for  $H$  is estimated, assuming it remains stable in the future, we only need a few of recent datapoints to forecast the future temperature. The information of the unknown data from the distant past is automatically considered by the model.

Previously, we showed that an fGn process is fully characterized by its autocovariance function, which in turn depends only on the covariance,  $\sigma_T^2$ , and the fluctuation exponent  $H$ . To extend our description to more general cases, we could allow our series to have a non-zero ensemble mean,  $\mu$ . This family of three parameters defines our fGn process and represents the link between the mathematical model and real-world historical data.

In Appendix 1 we discuss how to obtain maximum likelihood estimates (MLE) for these parameters on a given time series. For the fluctuation exponent, we show other approximate (and less computationally expensive) methods. We can use Eq. (9) to obtain  $\hat{H}_s = (\beta_l - 1)/2$  from the spectrum exponent at low frequencies. This method, as well as the Haar wavelet analysis to obtain an estimate  $\hat{H}_h$  from the exponent of the Haar fluctuations, was used in Lovejoy and Schertzer (2013) and Lovejoy et al. (2015) to obtain estimates of  $H$  for average global and Northern Hemisphere anomalies. A Quasi Maximum Likelihood Estimate (QMLE) method is also discussed in Appendix 1. The latter is more accurate than the Haar fluctuations and the spectral analysis methods and is obtained as part of the hindcast verification process. Nevertheless, those two have the advantage of being more general and applicable to any scaling process (even highly nonGaussian ones).

All these methods were applied to fGn simulations and the parameters estimated were summarized in Table 4. The technical details for producing exact simulations are also discussed in Appendix 1. Finally, we show how to check the adequacy of the fitted fGn model to real-world data and we derive some ergodic properties of fGn processes. Specifically, we show that the temporal average standard deviation squared,  $SD_T^2 = \sum_{t=1}^N (T_t - \bar{T}_N)^2/N$ , is a strongly biased estimate of the variance of the process,  $\sigma_T^2$ , for values of  $H$  close to zero (the overbar denotes temporal averaging:  $\bar{T}_N = \sum_{t=1}^N T_t/N$ ). The sample and the ensemble estimates are related by:

$$SD_T^2 = \sigma_T^2(1 - N^{2H}). \quad (25)$$

When  $H = -0.06$ ,  $N = 1656$  (values for the monthly series since 1880) there is a huge difference between the sample and the ensemble estimates ( $SD_T^2/\sigma_T^2 = 0.59$ ). Some skill scores (e.g. the MSSS or the normalized mean squared error NMSE) use the variance for normalization.

The implications of the difference in the estimates of the variance on the definition of the MSSS will be discussed in Sect. 3.4.3.

### 3 Forecasting global temperature anomalies

#### 3.1 The data

The general framework presented here is applicable to forecasting any time series that satisfies, (a) the conditions of stationarity, (b) Gaussianity and (c) long-range dependence given by power-law behavior of the correlation function with fluctuation exponents in the range  $(-1/2, 0)$ . These three properties are well satisfied for globally-averaged temperature anomaly time series in the macroweather regime, from 10 days to some decades (Lovejoy and Schertzer 2013; Lovejoy et al. 2013, 2015). In the last three decades, there has been a growing literature showing that the temperature (and other atmospheric fields) are scaling in the macroweather regime (Koscielny-Bunde et al. 1998; Blender et al. 2006; Huybers and Curry 2006; Franzke 2012; Rypdal et al. 2013; Yuan et al. 2015) and see the extensive review in Lovejoy and Schertzer (2013). Strictly speaking, in the last century, low frequencies become dominated by anthropogenic effects and after 10–20 years the scaling regime changes from a negative to a positive value of  $H$ , as we will show below. As was discussed in detail in Lovejoy (2014, 2017) and Lovejoy et al. (2015), differently from preindustrial epochs, recent temperature time series can be modeled by a trend stationary process, i.e. a stochastic process from which an underlying trend (function solely of time) can be removed, leaving a stationary process. In other words, to first order, variability is unaffected by climate change. The deterministic trend representing the response to external forcings can be removed by using  $\text{CO}_2$  radiative forcing as a good linear proxy for all the anthropogenic effects [or equivalent- $\text{CO}_2$  ( $\text{CO}_2\text{eq}$ ) radiative forcing as the one used for CMIP5 simulation (Meinshausen et al. 2011)]. There is a nearly linear relation between the actual  $\text{CO}_2$  concentration and the estimated equivalent concentration which includes all anthropogenic forcings, including greenhouse gases, aerosols, etc. (Meinshausen et al. 2011).

In this paper, we limit our analysis to globally-averaged temperature anomaly time series at monthly resolution. This is a first step for checking the applicability of the model and at the same time providing an alternative method for obtaining long-term forecasts. The quality of our method can be assessed based on the skill obtained from hindcasts verification and its agreement with the theoretical prediction.



619 There are five major observation-based global tempera- 653  
 620 ture datasets which are in common use. They are (a) the 654  
 621 NASA Goddard Institute for Space Studies Surface Tem- 655  
 622 perature Analysis (GISTEMP) series, abbreviated NASA 656  
 623 and NASA-L in the following for global and land surface 657  
 624 averages respectively (Hansen et al. 2010; GISTEMP Team 658  
 625 2018), (b) the NOAA NCEI series GHCN-M version 3.3.0 659  
 626 plus ERSST dataset (Smith et al. 2008; NOAA-NCEI 2018), 660  
 627 updated in Gleason et al. (2015), abbreviated NOAA and 661  
 628 NOAA-L (global and land surface averages, as before), 662  
 629 (c) the Combined land and sea surface temperature (SST) 663  
 630 anomalies from CRUTEM4 and HadSST3, Hadley Centre— 664  
 631 Climatic Research Unit Version 4, abbreviated HAD4 665  
 632 and HAD4-L (Morice et al. 2012; Met Office Hadley Centre 666  
 633 2018), (d) the version 2 series of (Cowtan and Way 2014, 667  
 634 2018), abbreviated CowW and CowW-L, and (e) the Berke- 668  
 635 ley Earth series (Rohde et al. 2013; Berkeley Earth 2018), 669  
 636 abbreviated Berk and Berk-L. The average of the global and 670  
 637 the land surface series were included in the analysis and we 671  
 638 use for the abbreviations Mean-G and Mean-L, respectively. 672

639 All these series are of anomalies, i.e. the difference 673  
 640 between temperature at a given time and the average during 674  
 641 a baseline period. They tend not to be on the same baseline; 675  
 642 for NASA and Berk the reference period is 1951–1980, for 676  
 643 HAD4 and CowW it is 1961–1990, and for NOAA it is the 677  
 644 20th century (1901–2000). To compare them, we need to 678  
 645 use the same zero point. In this case we chose the 20th 679  
 646 century average as a common reference period. The average 680  
 647 temperature for 1901–2000 is nearly the same as that for 681  
 648 1951–1980, while that of more recent times (1961–1990) 682  
 649 is warmer. 683

650 Each series spans a somewhat different period: HAD4, 684  
 651 CowW and Berk start first, beginning in 1850, NASA and 685  
 652 NOAA both start in 1880. When the data were accessed on

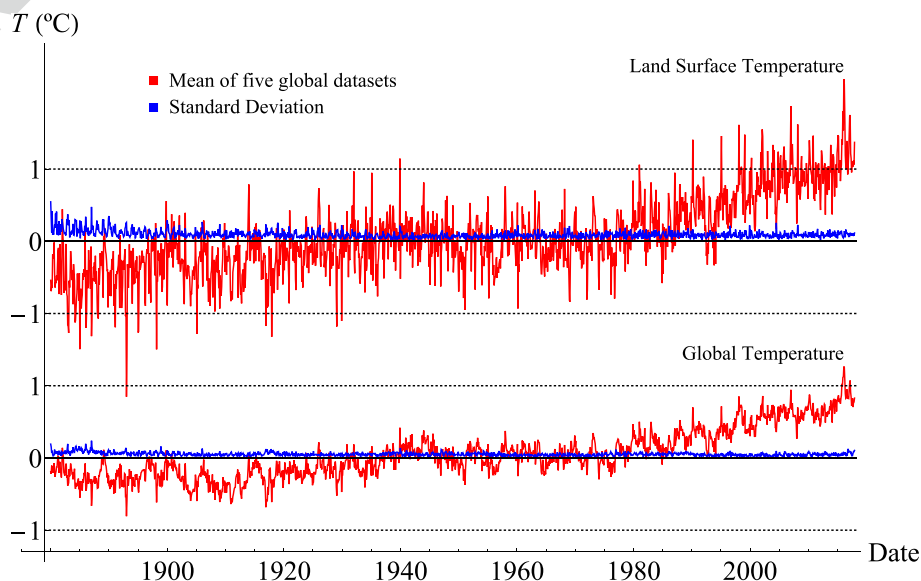
653 May 21, 2018, they were all available at monthly resolutions 654  
 655 until April 2018. Only the period January 1880–December 656  
 657 2017 was analyzed, i.e. 138 years = 1656 months (the same 658  
 659 length that was used in the simulations in Appendix 1). 660  
 661 These series (updated until 2012), together with twentieth 662  
 663 century reanalysis global average, were used in (Lovejoy 664  
 665 2017) to assess how accurate are the data as functions of 666  
 667 their time scale. As it was pointed out in the latter, each data 668  
 669 set has its strengths and weaknesses and it is precisely their 669  
 670 degree of agreement or disagreement what permits us to 670  
 671 evaluate the intrinsic absolute uncertainty in the estimates 671  
 672 of the global temperature. 672

665 In Fig. 4 we show the global average temperature (bot- 666  
 667 tom) and the land surface average temperature (top). In red 667  
 668 are the means of the five global datasets for global and for 668  
 669 land, respectively, and in blue are a measure of their level 669  
 670 of dispersion given by the standard deviations. The datasets 670  
 671 are most dissimilar before 1900, which could be due to the lack 671  
 672 of reliable measurements, but otherwise, the overall level of 672  
 673 agreement is very good [about  $\pm 0.05$  °C and is nearly inde- 673  
 674 pendent of scale for the global temperature series (Lovejoy 674  
 675 2017)]. Each series shows warming during the last decades, 675  
 676 and they all show fluctuations superimposed on the warm- 676  
 677 ing trend. 677

### 3.2 Removing the anthropogenic component

678 In the present case of globally-averaged temperatures, the 678  
 679 seasonality in the time series is weak. The deterministic 679  
 680 annual cycle component was removed first from the original 680  
 681 series. It was estimated from the average of every month for 681  
 682 the full period of 138 years (1880–2017). Cross-validation 682  
 683 effects are weak for such a long reference period and were 683  
 684 not considered. 684

**Fig. 4** Monthly surface temperature anomaly series from 1880 to 2017. In red is the mean of the five datasets for global (bottom): NASA, NOAA, HAD4, CowW, and Berk, and for land (top): NASA-L, NOAA-L, HAD4-L, CowW-L, and Berk-L. The dispersion among the series—given by the standard deviations of the five series as a function of time—is shown in blue. Each series represents the anomaly with respect to the mean of the reference period 1901–2000



Because of the anthropogenically induced trends in addition to internal macroweather variability, global temperature time series have low-frequency forced variability. A simple application of the linearity of the climate response to external forcings yields:

$$T(t) = T_{\text{anth}}(t) + T_{\text{nat}}(t), \quad (26)$$

which considers the temperature as a combination of a purely deterministic response to anthropogenic forcings,  $T_{\text{anth}}$ , plus a strict stationary stochastic component,  $T_{\text{nat}}$ , with zero mean. The low frequency component can be obtained as:

$$T_{\text{anth}}(t) = \lambda_{2 \times \text{CO}_2 \text{eq}} \log_2 [\rho_{\text{CO}_2 \text{eq}}(t) / \rho_{\text{CO}_2 \text{eq,pre}}] + T_0, \quad (27)$$

where  $\rho_{\text{CO}_2 \text{eq}}$  is the observed globally-averaged equivalent- $\text{CO}_2$  concentration with preindustrial value  $\rho_{\text{CO}_2 \text{eq,pre}} = 277$  ppm and  $\lambda_{2 \times \text{CO}_2 \text{eq}}$  is the transient climate sensitivity (that excludes delayed responses) related to the doubling of atmospheric equivalent- $\text{CO}_2$  concentrations. For  $\rho_{\text{CO}_2 \text{eq}}$  we used the CMIP5 simulation values (Meinshausen et al. 2011). The definition of  $\text{CO}_2 \text{eq}$  here includes not only greenhouse gases, but also aerosols, with their corresponding cooling effect. The reference value  $T_0$  is chosen so that  $\bar{T}_{\text{nat}} = 0$ , (the overbar indicates temporal averaging). The parameters  $\lambda_{2 \times \text{CO}_2 \text{eq}}$  and  $T_0$  are estimated from the linear regression of  $T(t)$  vs.  $\log_2 [\rho_{\text{CO}_2 \text{eq}}(t) / \rho_{\text{CO}_2 \text{eq,pre}}]$ . The residuals are the stochastic natural variability component,  $T_{\text{nat}}$ .

The natural variability includes “internal” variability and the response of the system to natural forcings: solar and volcanic. There is no gain in trying to model the responses to these two natural forcings independently. They would represent unpredictable signals while the ensemble of  $T_{\text{nat}}$  can be directly modelled using the techniques discussed in Sect. 2 for fGn processes. We made some experiments trying to predict the internal variability and the solar and the volcanic responses independently, and the combined error was larger than if we try to forecast the natural variability component as a whole. On the other hand, the relatively smooth dependence of the anthropogenic component makes it easy to project it a few years into the future with good accuracy.

As an example, the temperature anomalies for the global average dataset (Mean-G) is shown in Fig. 5 (red in the online version) together with the  $\text{CO}_2 \text{eq}$  response to anthropogenic forcings (dashed, black) and the residual natural variability component (blue). To use  $\text{CO}_2$  instead of  $\text{CO}_2 \text{eq}$  forcings leads to almost the same residuals due to the nearly linear relation between the two, but it avoids the uncertainties due to the estimation of the cooling effects of the aerosols as well as other radiative assumptions. The  $\text{CO}_2$  forcing is taken as a surrogate for all the anthropogenic forcings. The focus of this work is to model and forecast the residuals (natural variability), and for that purpose, either of the two

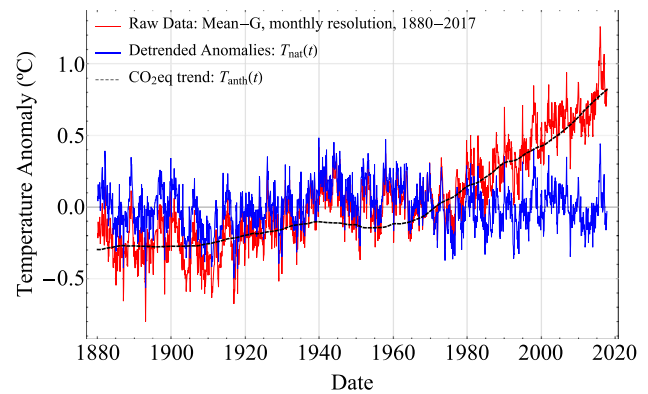


**Fig. 5** Temperature anomalies for the Mean-G dataset (red in the online version) together with the  $\text{CO}_2 \text{eq}$  trend (dashed, black) and the residual natural variability component (blue)

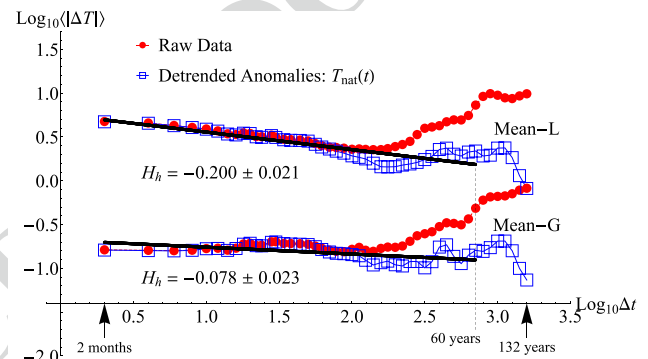


**Fig. 6** Haar fluctuation analysis for the Mean-G (bottom) and Mean-L (top) datasets before (red) and after (blue) removing the trends. The reference lines with slopes  $H_h = -0.064 \pm 0.020$  for the global series and  $H_h = -0.241 \pm 0.017$  for the land surface series were obtained from regression of the residuals between 2 months and 60 years. The last points were dropped to get better statistics. The units for  $\Delta t$  and  $\Delta T$  are months and  $^{\circ}\text{C}$ , respectively

concentrations would lead to the same residuals (they differ by a factor of 1.12 over the last century). From a direct inspection of Fig. 5, it is clear that a  $\text{CO}_2 \text{eq}$  response does a much better job of reproducing the actual trend of the temperature series than a simple regression linear in time, which is often used for estimating the warming trend.

Before making predictions, we need to verify the adequacy of the model and verify the hypothesis that the residual natural variability component has scaling fluctuations with exponent in the range  $(-1/2, 0)$ . The Haar fluctuation analysis for the Mean-G (bottom) and Mean-L (top) datasets before and after removing the anthropogenic trends are shown in Fig. 6 (red for the raw dataset fluctuations and blue for the detrended series in the online version). The reference lines with slopes  $H_h = -0.078 \pm 0.023$  for the global series and  $H_h = -0.200 \pm 0.021$  for the land surface series were obtained from regression of the residuals' fluctuations

752 between 2 months and 60 years. The points correspond-  
 753 ing to scales of more than 60 years were not considered  
 754 for estimating the parameters as there were not many fluctu-  
 755 ations to average at those time scales. In addition, some  
 756 of the low frequency natural variability was presumably  
 757 removed with the forced variability. The units for  $\Delta t$  and  
 758  $\Delta T$  are months and  $^{\circ}\text{C}$ , respectively. Notice that the anthro-  
 759 pogenic warming breaks the scaling of the fluctuations at  
 760 a time scale of around 10 years (the red and blue curves  
 761 diverge at  $\sim 100$  months). The residual natural variability,  
 762 on the other hand, shows reasonably good scaling for the  
 763 whole period analyzed (138 years). The same range of scaling  
 764 with decreasing fluctuations has been obtained in tem-  
 765 perature records from preindustrial multiproxies and GCMs  
 766 preindustrial control runs (Lovejoy 2014).

767 The global series are a composition of land surface data  
 768 and sea surface temperature data. The average temperature  
 769 over the ocean shows fluctuations increasing with the time  
 770 scale (positive  $H$ ) up to 2 years. This corresponds to the ocean  
 771 weather regime as discussed in Lovejoy and Schertzer (2013).  
 772 The same break in the scaling is found in the global tem-  
 773 perature fluctuations, but this break is subtle, and an overall  
 774 unique scaling regime can be assumed for the global data. The  
 775 influence of the ocean on the global temperature also brings  
 776 its fluctuation exponent towards higher values (closer to zero)  
 777 compared to the land surface fluctuations. This makes the  
 778 global data more predictable than the land-only series.

779 In the frequency domain, the corresponding spectra for  
 780 the Mean-G dataset are shown in Fig. 7. The raw spectrum  
 781 for the natural variability series is represented in grey. It  
 782 shows scaling, but with large fluctuations, as expected. To  
 783 get better estimates of the exponent we can average the raw  
 784 spectra using logarithmically spaced bins. These “cleaner”  
 785 spectra for the series before and after removing the anthro-  
 786 pogenic trend are shown in red and blue in the online ver-  
 787 sion, respectively. Notice that they only differ appreciably  
 788 for the low-frequency range, corresponding to the removed  
 789 deterministic trend. The frequency,  $\omega$ , is given in units  
 790 of  $(138 \text{ years})^{-1}$ . The particularly low variabilities at fre-  
 791 quencies corresponding to  $(30 \text{ years})^{-1}$  is an artefact of the  
 792 30-year detrending period used in most of the datasets. The  
 793 solid black line was obtained from a linear regression on the  
 794 residues. The exponent obtained from the absolute value of  
 795 the slope was  $\beta = 0.81 \pm 0.13$ . Using the monofractal rela-  
 796 tion  $\beta = 1 + 2H$ , we obtain the estimate for the fluctuation  
 797 exponent:  $H_s = -0.096 \pm 0.063$ . The dashed reference line  
 798 with slope corresponding to  $\beta_h = 1 + 2H_h = 0.84 \pm 0.05$   
 799 was included in the figure for comparison (using the value  
 800 obtained from the Haar fluctuation analysis in Fig. 6).

801 It is worth mentioning that this very simple approach to  
 802 removing the warming trend is a special (low memory) case  
 803 of the much more general model of linear response theory  
 804 with a scaling response function proposed by Hébert et al.

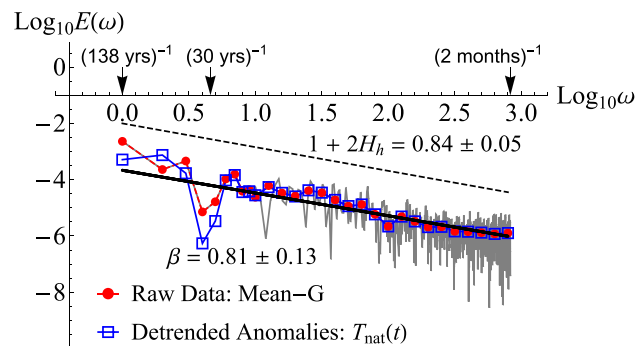


Fig. 7 Spectra for the Mean-G dataset. In grey is the raw spectrum of the residuals. Averages with logarithmically spaced bins are shown for the series before (dashed, red) and after (blue) removing the trend. The solid black line, with slope  $-\beta$ , was obtained from a linear regression on the residues. The reference dashed line with absolute value of the slope  $1 + 2H_h = 0.84 \pm 0.05$  was included for comparison (using the value obtained from the Haar fluctuation analysis in Fig. 6). The frequency,  $\omega$ , is given in units of  $(138 \text{ years})^{-1}$

(2019). In this work, the authors directly exploit the sto- 805  
 chasticity of the internal variability and the linearity and 806  
 scaling of the forced response to make projections based 807  
 on historical data and a scaling step Climate Response 808  
 Function that has a long memory. They not only include 809  
 anthropogenic effects, but also solar and volcanic forcings. 810  
 Consequently, the residuals they obtain once these forced 811  
 components are removed, do not represent the forced natu- 812  
 ral variability response, but the internal variability of the 813  
 system. The authors based their analysis on the assumption 814  
 that this internal stochastic component can be approximated 815  
 by an fGn process. This hypothesis has been confirmed on 816  
 GCMs preindustrial control runs outputs where the forcings 817  
 are not present. 818

### 3.3 Fitting fGn to global data 819

Having obtained the stationary natural variability com- 820  
 ponent,  $T_{\text{nat}}$ , for the Mean-G dataset from the residuals of 821  
 the linear regression of  $T(t)$  vs.  $\log_2 [\rho_{\text{CO}_2, \text{eq}}(t) / \rho_{\text{CO}_2, \text{eq, pre}}]$  822  
 (Eqs. (26) and (27)), we can now model this series using 823  
 the theory presented in Sect. 2 and Appendix 1. The first 824  
 step is to obtain the parameters  $\mu$ ,  $\sigma_T^2$  and  $H$ . We would like 825  
 to underline that these parameters describe the—infinite 826  
 ensemble—fGn stochastic process, but we can only obtain 827  
 estimates for them based on a single realization (our glob- 828  
 ally-averaged temperature time series). In Appendix 1 we 829  
 show how to obtain the MLE for  $\mu$  and  $\sigma_T^2$ . In the case of 830  
 the fluctuation exponent, we can repeat the methods pre- 831  
 sented in Sect. 3.2 and obtain estimates from the slopes in 832  
 the Haar fluctuations and the spectrum curves. However, 833  
 as we mentioned before, it is clear in Figs. 6 and 7 that 834  
 the error in the estimates is much higher for these methods than 835

836 by using the MLE or QMLE due to the high variability of  
 837 the fluctuations. Nevertheless, their advantage over the latter  
 838 is that they are general and apply not only to Gaussian  
 839 processes (such as fGn), but also to multifractal or other  
 840 intermittent processes with different statistics. The MLE and  
 841 QMLE methods make the extra assumption of adequacy of  
 842 the fGn model, which ultimately must be verified.

843 To get an idea of how well the stochastic model describes  
 844 the observational dataset, we created completely synthetic  
 845 time series by superimposing fGn simulations on the low-  
 846 frequency anthropogenic trend. Four randomly chosen  
 847 simulations are shown in Fig. 8 together with the Mean-  
 848 G dataset (top). The synthetic series were created using  
 849  $\lambda_{2 \times \text{CO}_2 \text{ eq}} = 2.03 \text{ }^\circ\text{C}$  and  $T_0 = -0.379 \text{ }^\circ\text{C}$  for the anthropo-  
 850 genic trend,  $T_{\text{anth}}$ , and following the procedure described  
 851 in Appendix 1-i with parameters  $\mu = 0 \text{ }^\circ\text{C}$ ,  $\sigma_T = 0.195 \text{ }^\circ\text{C}$   
 852 and  $H = -0.060$  for simulating  $T_{\text{nat}}$  (see Eqs. (26) and (27)).  
 853 All these parameters were obtained by fitting the Mean-G  
 854 observations in the period 1880–2017 ( $N = 1656$  months).  
 855 In Appendix 2 (Table 5), we summarize the parameters  
 856 obtained for the ten datasets and the corresponding mean  
 857 series for global and for land.

858 Although a visual inspection of Fig. 8 is not a convincing  
 859 proof of the applicability of the model, it is clear that if we  
 860 eyeball the completely synthetic time series with the obser-  
 861 vational Mean-G dataset, you cannot tell which is which. A  
 862 simple verification of the fGn behavior of the detrended data  
 863 can be done by checking that the biased temporal estimate of  
 864 the variance,  $SD_T^2$ , and the value obtained using maximum  
 865 likelihood,  $\hat{\sigma}_T^2$ , satisfy Eq. (25) (derived in Appendix 1-iii.).

866 Following Eq. (25), the temporal estimate of the vari-  
 867 ance should depend on the number of months,  $n$ , that is

868 used for the estimates:  $SD_T^2(n) = \sigma_T^2(1 - n^{2H})$ . For only one  
 869 time series, the estimate of  $SD_T^2(n)$  is noisy. To reduce the  
 870 noise, this value can be estimated using  $k$ -segments of the  
 871 series from  $t = k$  to  $t = k + n - 1$  (each of length  $n$ ), and  
 872 then averaged over the total ensemble of segments (in this  
 873 case  $N_{\text{segments}} = N - n_{\text{max}}$ , where  $N = 1656$  months is the full  
 874 length of the series and  $n_{\text{max}} = 120$  months is the maximum  
 875 length of the segments used):  
 876

$$\langle SD_T^2(n) \rangle = \frac{n-1}{n} SD_T^2(n) = \frac{1}{N - n_{\text{max}}} \sum_{k=1}^{N - n_{\text{max}}} \left[ \frac{1}{n} \sum_{t=k}^{k+n-1} (T_t - \bar{T}_n)^2 \right], \quad (28)$$

877 where  $\bar{T}_n = \sum_{t=1}^n T_t/n$ , the values  $T_t$  are for the natural  
 878 variability component of the Mean-G dataset and the fac-  
 879 tor  $(n-1)/n$  accounts for the bias of the length- $n$  sample  
 880 estimate,  $SD_T^2(n)$ , with respect to the length- $n$  population  
 881 variance,  $\langle SD_T^2(n) \rangle$ .

882 In Fig. 9 we show in red line with circles the empirical  
 883 values of the standard deviation  $\langle SD_T^2(n) \rangle^{1/2}$  as a function  
 884 of  $n$  (obtained using Eq. (28) for the ensemble of  $N - n_{\text{max}}$

885 segments). The function  $f_{\sigma_T, H}(n) = \sigma_T \sqrt{(1 - n^{2H})(1 - n^{-1})}$

886 (obtained by replacing the expression for  $SD_T^2(n)$  in Eq. (28)

887 and taking the square root) is plotted using

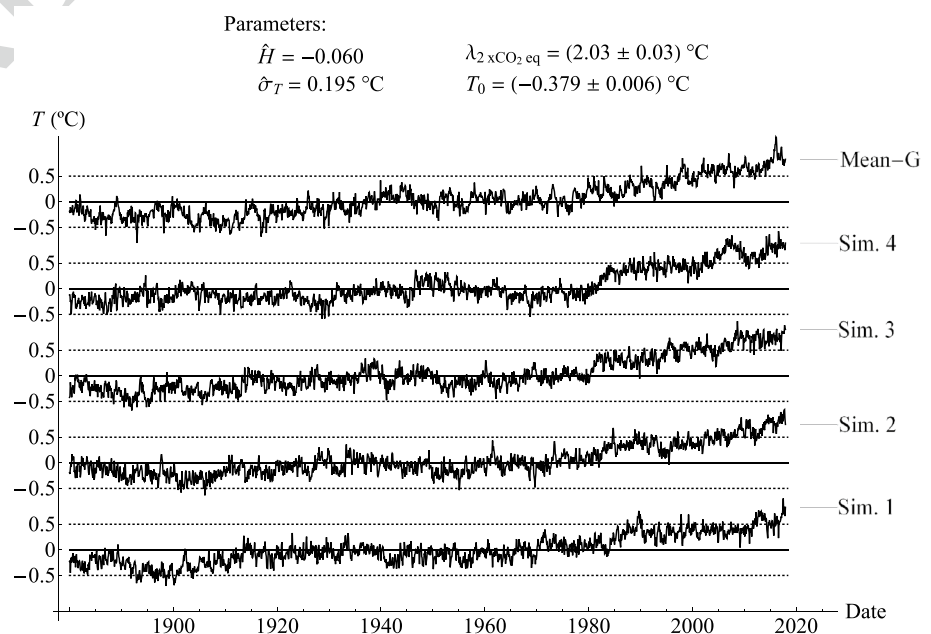
888  $\sigma_T = \hat{\sigma}_T = 0.195 \text{ }^\circ\text{C}$  and the following values of  $H$ :

889  $H_f = -0.069$  (solid black line), obtained from the fit of the

890 red curve;  $H_l = -0.060$  (dashed line), obtained using MLE,

891 and  $H_q = -0.080$  (dotted line), from the QMLE. The empiri-  
 892 cal curve for a synthetic realization of Gaussian white noise  
 893 with standard deviation  $\sigma_{\text{wn}} = 0.141 \text{ }^\circ\text{C}$  was also included  
 894 for comparison (blue line with squares).

**Fig. 8** Four randomly chosen synthetic time series together with the Mean-G dataset (top). The simulations were created by superimposing fGn simulations for  $T_{\text{nat}}$  to the low-frequency anthropogenic trend,  $T_{\text{anth}}$  (see Appendix 1 and Eqs. (26) and (27)). The parameters used for the simulation (shown in the figure) were obtained by fitting the Mean-G series in the period 1880–2017





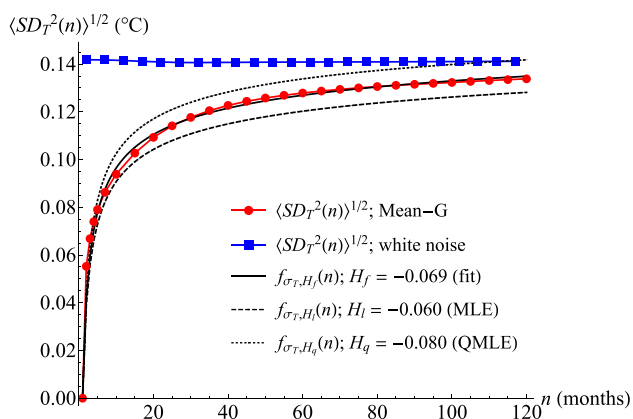


**Fig. 9** Empirical values of  $\langle SD_T^2(n) \rangle^{1/2}$  as a function of  $n$ , obtained using Eq. (28) (red line with circles). The function  $f_{\sigma_T, H}(n) = \sigma_T \sqrt{(1 - n^{2H})(1 - n^{-1})}$ , with  $\sigma_T = \hat{\sigma}_T = 0.195$  °C, is plotted for three values of  $H$ :  $H_f = -0.069$  (solid black line), obtained from the fit of the red curve;  $H_l = -0.060$  (dashed line), obtained using MLE and  $H_q = -0.080$  (dotted line), from QMLE. The empirical curve for a synthetic realization of Gaussian white noise with variance  $\sigma_{wn}^2 = 0.02$  °C was also included for comparison (blue line with squares). The agreement between the red line with circles and the solid black line is an evidence of the fGn behavior of the natural variability

895 The difference between the red curve for the observational  
 896 time series and the blue curve for the uncorrelated synthetic  
 897 series illustrates the effects of the long-range correlations in  
 898 the natural variability of the globally-averaged temperature  
 899 time series. This strong dependence of the estimates of the  
 900 variance with the length of the estimation period for  $H$  close  
 901 to zero could have an influence on statistical methods that  
 902 depend on the covariance matrix [e.g. empirical orthogonal  
 903 function (EOF) and empirical mode decompositions (EMD)].

904 The agreement between the  $\langle SD_T^2(n) \rangle^{1/2}$  curve esti-  
 905 mated from the data and the function  $f_{\sigma_T, H}(n)$ —that only  
 906 depends on the two parameters  $\sigma_T$  and  $H$ —is an evidence of  
 907 the good fit of the fGn stochastic model to the natural vari-  
 908 ability. At the same time, it could be used as an alternative  
 909 method for obtaining the parameters  $\sigma_T$  and  $H$  by fitting the  
 910 curve  $\langle SD_T^2(n) \rangle^{1/2}$  based on observations using the function  
 911  $f_{\sigma_T, H}(n)$ .

912 More detailed statistical tests to check the fit of the model  
 913 to the data are shown in Appendix 2 using the theory pre-  
 914 sented at the end of Appendix 1. The main conclusion is  
 915 that the global average temperature series can be consid-  
 916 ered Gaussian as well as their innovations, while for the  
 917 case of land average temperature, there are some deviations  
 918 from Gaussianity. Nevertheless, the residual autocorrelation  
 919 functions (RACF) satisfy the normality condition with good  
 920 enough accuracy for all datasets, corroborating the white-  
 921 ness of the innovations and hence that an fGn model can be  
 922 considered a good approximation in all cases.

### 3.4 Forecast and validation

923

#### 3.4.1 The low-frequency anthropogenic component

924

925 Ultimately, as a final step to confirm the adequacy of the  
 926 model to simulating and forecasting global temperature data,  
 927 we present the skill scores obtained from hindcast verifica-  
 928 tions and compare their values with the theoretical predic-  
 929 tions. First, we should point out that for predicting the global  
 930 temperature we need to forecast both the anthropogenic  
 931 component and the natural variability. Our final estimator  
 932 for  $k$  steps into the future, following Eq. (26), is given by:

$$\hat{T}(t+k) = \hat{T}_{\text{anth}}(t+k) + \hat{T}_{\text{nat}}(t+k), \quad (29)$$

933

934 where  $\hat{T}_{\text{nat}}$  is obtained from Eq. (22) using the theory pre-  
 935 sented in Sect. 2.2.1. The anthropogenic component, which  
 936 we model with a separate low-frequency process must also  
 937 be forecast. Nevertheless, even if we use persistence of the  
 938 CO<sub>2</sub>eq increments, the error on predicting the low-frequency  
 939 component is small compared to the error on forecasting the  
 940 natural variability (for lead times up to a year or so). For  
 941 this reason, for obtaining  $\hat{T}_{\text{anth}}(t+k)$  based on the previous  
 942 values of the trend, we just assume persistence of the incre-  
 943 ments  $\Delta T_{\text{anth}}(t, k) = T_{\text{anth}}(t) - T_{\text{anth}}(t-k)$ , that is:

$$\hat{T}_{\text{anth}}(t+k) = T_{\text{anth}}(k) + \Delta T_{\text{anth}}(t, k) \quad (30)$$

944

945 For a linear trend, the absolute error  $\langle |T_{\text{anth}}(t+k) - \hat{T}_{\text{anth}}(t+k)| \rangle = \langle |\Delta T_{\text{anth}}(t+k, k) - \Delta T_{\text{anth}}(t, k)| \rangle = 0$ . In  
 946 the case of the CO<sub>2</sub>eq trend shown in black in Fig. 5, for  
 947 small  $k$ , the function is almost linear in a  $k$ -vicinity of any  
 948  $t$ . This justifies the rejection of this error compared to the  
 949 error on forecasting the natural variability. For reference, the  
 950 root mean square error (RMSE) using this method for the  
 951 anthropogenic component, in the 1044-months hindcast  
 952 period January 1931–December 2017, performed with  
 953  $k = 24$  months in advance for every month, was of 0.01 °C  
 954 for all global datasets.

#### 3.4.2 The natural variability component

956

957 For the natural variability, the expectation of the RMSE—  
 958 taking the infinite ensemble average using the theory for  
 959 fGn—for a prediction  $k$  steps into the future is defined by:

$$\text{RMSE}_{\text{nat}}^{\text{theory}}(k) = \sqrt{\langle [T_{\text{nat}}(t+k) - \hat{T}_{\text{nat}}(t+k)]^2 \rangle}. \quad (31)$$

960

961 According to the definition of MSSS, given by Eq. (12),  
 962 and the analytical expression, Eq. (24), a theoretical ensemble  
 963 estimate of  $\text{RMSE}_{\text{nat}}(k)$ , for prediction using a memory  
 964 of  $m$  steps, is given by:

$$\text{RMSE}_{\text{nat}}^{\text{theory}}(k) = \text{RMSE}_{H, \sigma_T}^m(k) = \sigma_T \sqrt{1 - \tilde{\mathbf{C}}_H^m(k)^T (\tilde{\mathbf{R}}_H^m)^{-1} \tilde{\mathbf{C}}_H^m(k)}. \quad (32)$$

Notice that, unlike the MSSS, this is not only a function of the horizon,  $k$ , the memory,  $m$ , and the exponent,  $H$ , but also of the specific series we are forecasting due to the presence of the parameter  $\sigma_T$ , which must be estimated using Eq. (50) in Appendix 1. As expected, for given values of  $k$ ,  $m$  and  $H$ , the RMSE is proportional to the amplitude of the series we want to predict.

### 3.4.3 Validation

To validate our model, we produced series of hindcasts at monthly resolution, each for a different horizon from 1 to 12 months, in the verification period January 1931–December 2017. For this hindcast series each subsequent point plotted on the graph was independently predicted using the information available  $k$  months before. What changes from month to month is the initialization date while the forecast horizon is kept fixed. Such hindcast series are useful because they show how close the predictions are to the observations for a given value of  $k$ . The dependence with the horizon of many scores (e.g., the RMSE), are obtained from the difference between hindcasts series at a fixed  $k$  and the corresponding series of observations.

StocSIPS assumes an additive fixed annual cycle independent of the low-frequency trend; it does not make distinctions from month to month from the point of view of the statistics of the anomalies. In fact, is this month-to-month correlation that is exploited as a source of predictability in the stochastic model. Nevertheless, there is always an intrinsic multiplicative seasonality in the data that is impossible to completely remove without affecting the scaling behavior of the spectrum. To account for the effects of this seasonality, we can stratify the observations and the forecasts series to show dependences with the initialization date.

For each horizon,  $k$ , we used a memory  $m = 20k$ . For example, to predict the average temperature for January 1931 with  $k = 1$  month, we used the previous 21 months, including December 1930, and the same was done for each month up to December 2017. For  $k = 2$  months, we used the previous 41 months, including December 1930, to produce the first forecast for February 1931, and so on.

Examples of the hindcasts series initialized every month, each for a different horizon, are shown in Fig. 10 for the Mean-G natural variability. In blue, we show the hindcasts series for  $k = 1, 3$  and 6 months (bottom to top). In red we show the verification curve of observations for the natural variability starting in January 1931. The vertical gridlines correspond to the forecast and verification for each January; that is, initializing the first day of each January with data up to every December in the bottom panel, up to every October

in the middle panel and up to every July in the top one. This shows how the stratification is done for obtaining dependences of the skill with the initialization date (shown later).

As can be seen in Fig. 10, there is a reduction of the amplitude and an increasing lag between the observed and forecast time series as the horizon increases (more noticeable in the top panel). This is due to the model tendency to predict the return rate towards the mean as a function of  $H$ . Extremes can therefore only be predicted as a consequence of the anthropogenic increase. However, the general behavior of the temperature is well predicted.

Equation (31) is the definition of the infinite ensemble expectation of the RMSE, for which we get an analytical expression (Eq. (32)). The all-months verification RMSE can then be computed from the series shown in Fig. 10 as:

$$\text{RMSE}_{\text{nat}}(k) = \sqrt{\frac{1}{N - k + 1} \sum_{t=0}^{N-k+1} (T_{\text{nat}}(t+k) - \hat{T}_{\text{nat}}(t+k))^2} \quad (33)$$

where  $N = 1044$  months (from January 1931 to December 2017) and the number of terms in the sum is reduced in  $k - 1$  because the last verification date (December 2017) is the same for every  $k$  while the first verification date is  $k$  months after December 1931 ( $t = 0$ ) for each horizon. This equation can be adapted to get the RMSE for each horizon and for each initialization month.

In Fig. 11a, we show a comparison between the RMSE obtained from the hindcasts of all the months in the verification period 1931–2017 using Eq. (33) and the theoretical

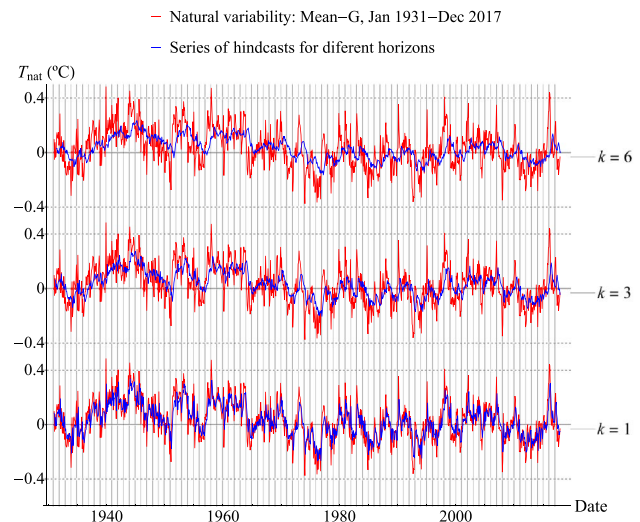


**Fig. 10** In blue, series of hindcasts for the Mean-G natural variability initialized every month for horizons  $k = 1, 3$  and 6 months (bottom to top). In red, the verification curve of observations for the natural variability starting in January 1931. The vertical gridlines correspond to the forecast and verification for each January; that is, initializing with data up to every December in the bottom panel, every October in the middle and every July in the top

1040 expected RMSE, which is only a function of  $\hat{\sigma}_T$ ,  $H$  and  $m$   
 1041 (Eq. (32)). The agreement between the theory (solid black)  
 1042 and the actual errors (red curve) is another confirmation  
 1043 of the model for the simulation and prediction of global  
 1044 temperature. In the figure, we also included the values  
 1045  $\hat{\sigma}_T = 0.195 \text{ }^\circ\text{C}$  and  $SD_T = 0.147 \text{ }^\circ\text{C}$  for the Mean-G natu-  
 1046 ral variability (dotted and dashed lines respectively). The  
 1047 value of the former is the same as shown in Table 5, while  
 1048 the value of the latter is slightly different from the value  
 1049 reported there because now it was computed for the verifica-  
 1050 tion series in the period 1931–2017 (red curve in Fig. 10).  
 1051 Notice that, for  $N = 1044$  months and  $H = -0.060$  (see

Table 5),  $SD_T/\sqrt{1 - N^{2H}} = 0.195 \text{ }^\circ\text{C}$ , in perfect agreement  
 with the value of  $\hat{\sigma}_T$  for that dataset.

The error for the anthropogenic trend forecast calculated  
 using Eq. (30) is always less than 7% of the  $RMSE_{nat}$  shown  
 in Fig. 11a (see the final paragraph of Sect. 3.4.1). Because  
 of this, its contribution to the overall error,  $RMSE_{raw}$ , on fore-  
 casting the raw temperature (natural plus anthropogenic) is  
 lower than 0.4% for all horizons (compare the red-circles and  
 the blue-squares curves in Fig. 11a). For all practical pur-  
 poses,  $RMSE_{raw} \approx RMSE_{nat}$  with a high degree of accuracy.

In Fig. 11b, we show a density plot with the RMSE as  
 a function of the forecast horizon and the initialization  
 month. The diagonal pattern from the top-left corner to the

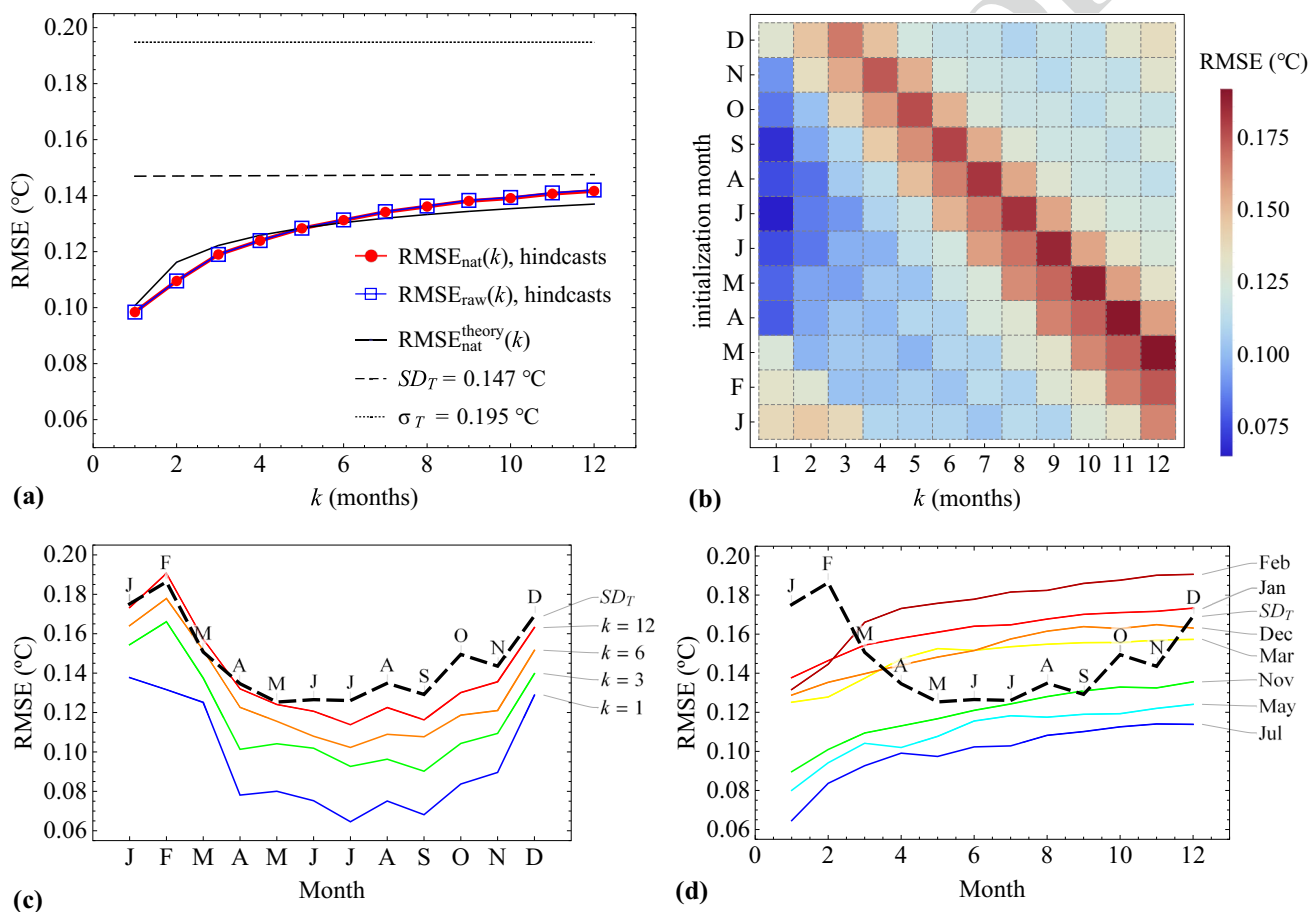


**Fig. 11** RMSE of StocSIPS forecasts for the Mean-G dataset. **a** Curves of  $RMSE_{nat}(k)$  (red circles) and  $RMSE_{raw}(k)$  (blue squares), for the natural variability component and for the raw series, respectively. The curves were obtained using Eq. (33) from the hindcasts of the Mean-G dataset including all the months in the verification period 1931–2017. The difference between the two is negligible. The theoretical expected  $RMSE_{nat}^{theory}(k)$  (solid black), given by Eq. (32), is also shown for comparison. The values of  $\hat{\sigma}_T$  (Table 5) and  $SD_T$  for the Mean-G natural variability were included for reference (dotted and dashed lines, respectively). **b** Density plot with the RMSE as a function of the forecast horizon and the initialization month. The diagonal pattern from the top-left corner to the bottom-right is an indication of

the intrinsic multiplicative seasonality in the time-series. **c** Graphs of RMSE vs. initialization month for different forecast horizons ( $k = 1, 3, 6$  and  $12$  months). There is an increase in the RMSE for the forecast of the Boreal winter months associated to the increase in the standard deviation,  $SD_T$ , of the globally-averaged temperature for those months (shown in dashed black line in the bottom panels figures). **d** Graphs of RMSE vs.  $k$  for different initialization months. For large values of  $k$  the skill of the model is small and the value of the RMSE is close to the standard deviation for that specific month (dashed black line). The RMSE graph in **a** is close to the average of the RMSE graphs in **d**

bottom-right is an indication of the intrinsic seasonality in the time-series. This is shown in detail in the bottom panels figures.

In Fig. 11c, we show graphs of RMSE vs. initialization month for different forecast horizons ( $k = 1, 3, 6$  and  $12$  months). There is an increase in the RMSE for the forecast of the Boreal winter months associated to the increase in the variability (standard deviation,  $SD_T$ ) of the globally-averaged temperature for those months (shown in dashed black line in the bottom panels figures). In Fig. 11d, we show graphs of RMSE vs.  $k$  for different initialization months. As expected, there is an increase in the RMSE with  $k$ . For large values of  $k$  the skill of the model is small and the value of the RMSE is close to the standard deviation for that specific month (dashed black line). The RMSE graph in panel (a) is close to the average of the RMSE graphs in panel (d). It is actually the all-month MSE the one that is the average of the MSEs for each month (as long as the number of years used for the average is the same for every month).

Related to the RMSE score, the mean square skill score (MSSS) is a commonly used metric:

$$\text{MSSS} = 1 - \frac{\text{MSE}}{\text{MSE}_{\text{ref}}}, \quad (34)$$

where  $\text{MSE} = \text{RMSE}^2$  is computed using Eq. (33) and  $\text{MSE}_{\text{ref}}$  is the mean square error of some reference forecast.

The climatology—constant annual cycle taken from the average in a given reference period of at least 30 years—is commonly used as reference forecast. In this case,  $\text{MSE}_{\text{ref}} = \text{SD}_{\text{raw}}^2$ , is the variance of the raw series:

$$\text{SD}_{\text{raw}}^2 = \overline{(T_{\text{anth}} + T_{\text{nat}})^2} = \overline{T_{\text{anth}}^2} + \text{SD}_T^2 \quad (35)$$

(assuming that the natural and anthropogenic variabilities are independent) and we call  $\text{MSSS} = \text{MSSS}_{\text{raw}}$ .

If we take as reference the anthropogenic trend forecast, then  $\text{MSE}_{\text{ref}} = \text{SD}_T^2$ , is the variance of the natural variability component (detrended series,  $T_{\text{nat}}$ ) and we name  $\text{MSSS} = \text{MSSS}_{\text{nat}}$ . This would be the same as the skill on forecasting the detrended series taking as reference forecast its mean value. Using the theoretical expressions for  $\text{SD}_T^2$  and for  $\text{RMSE} = \text{RMSE}_{\text{nat}}^{\text{theory}}(k)$  (Eqs. (25) and (32), respectively) we can obtain an analytical expression for  $\text{MSSS}_{\text{nat}}$ :

$$\text{MSSS}_{\text{nat}}^{\text{theory}}(k) = \frac{\text{MSSS}_H^m(k) - N^{2H}}{1 - N^{2H}}, \quad (36)$$

where  $\text{MSSS}_H^m(k)$  was defined for the infinite ensemble average in Eq. (24) [Eq. (13) for the continuous-time case]. Notice that  $\text{MSSS}_{\text{nat}}^{\text{theory}}(k)$  is not only a function of the fluctuation exponent,  $H$ , and the memory used for the forecasts,  $m$ , but also of the length of the verification period,  $N$ . For an infinite series, the ergodicity of the system is verified; i.e. the temporal average

is equal to the ensemble average:  $\text{MSSS}_{\text{nat}}^{\text{theory}}(k) = \text{MSSS}_H^m(k)$  (recall  $H < 0$ ). We can check the agreement between the theoretical result (Eq. (36)) and the  $\text{MSSS}_{\text{nat}}$  obtained from hindcast to verify the validity of the model.

The anomaly correlation coefficient (ACC) is another commonly used verification score. In this case, we can also obtain the ACC for the raw or for the detrended series:

$$\text{ACC}_{\text{nat/raw}}(k) = \frac{\overline{T_{\text{nat/raw}}(t+k)\hat{T}_{\text{nat/raw}}(t+k)}}{\text{SD}_{T/\text{raw}}\sqrt{\overline{\hat{T}_{\text{nat/raw}}(t)^2}}}, \quad (37)$$

where we assume that  $T(t)$  and the predictor  $\hat{T}(t)$  are zero mean anomalies, the overbars indicate temporal average for a constant forecast horizon,  $k$ , and either all the subscripts are “nat” or all are “raw” depending on whether we forecast the detrended or the raw anomalies, respectively. In the latter case, spurious high values of the ACC (similarly for the MSSS) are found due to the presence of the deterministic trend. This is a very common flaw found throughout the literature, where this score is routinely reported for undetrended anomalies.

It is useful to note the relationship between the ACC and MSSS obtained from minimum mean square predictions. It can be easily seen from the orthogonality principle,  $\langle \hat{T}(T - \hat{T}) \rangle = 0$ , that the stochastic predictions satisfy

$$\text{ACC}_{\text{nat}}(k) = \sqrt{\text{MSSS}_{\text{nat}}(k)} \quad (38)$$

for any horizon  $k$ . This relation can also be used to check the agreement between the theoretical predictions of the model and the actual results obtained from hindcasts verification.

In Fig. 12 we summarize the results for the MSSS (top) and the ACC (bottom). In Fig. 12a, we show curves of MSSS vs.  $k$  for the Mean-G dataset considering all months in the verification period 1931–2017. In red line with circles, the curve for  $\text{MSSS}_{\text{nat}}$  taking as reference the anthropogenic trend forecast, for which  $\text{MSE}_{\text{ref}} = \text{SD}_T^2$  ( $\text{SD}_T = 0.147^\circ\text{C}$ ). In green line with triangles, the values for  $\text{MSSS}_{\text{raw}}$  taking as reference the climatology forecast with  $\text{MSE}_{\text{ref}} = \text{SD}_{\text{raw}}^2$  ( $\text{SD}_{\text{raw}} = 0.293^\circ\text{C}$ ). The theoretical expected  $\text{MSSS}_{\text{nat}}^{\text{theory}}(k)$  (solid black), given by Eq. (36), is also shown for comparison. There is relatively good agreement between this theoretical prediction of the model and the MSSS values obtained from the verification. The asymptotic value of  $\text{MSSS}_{\text{nat}}^{\text{theory}}(k)$  for  $N \rightarrow \infty$  (given by Eq. (24)) is shown in dotted line with squares (dashed line for the continuous-time case, Eq. (13)). The longer the verification period the closer the MSSS will be to that asymptotic value. For the discrete theoretical curves (solid black line and dotted black with squares), we used a memory  $m = 20k$ . The small difference for  $k = 1$  month, between this curve and the one for the continuous case (solid black) is due to the high-frequency information loss in the discretization process.



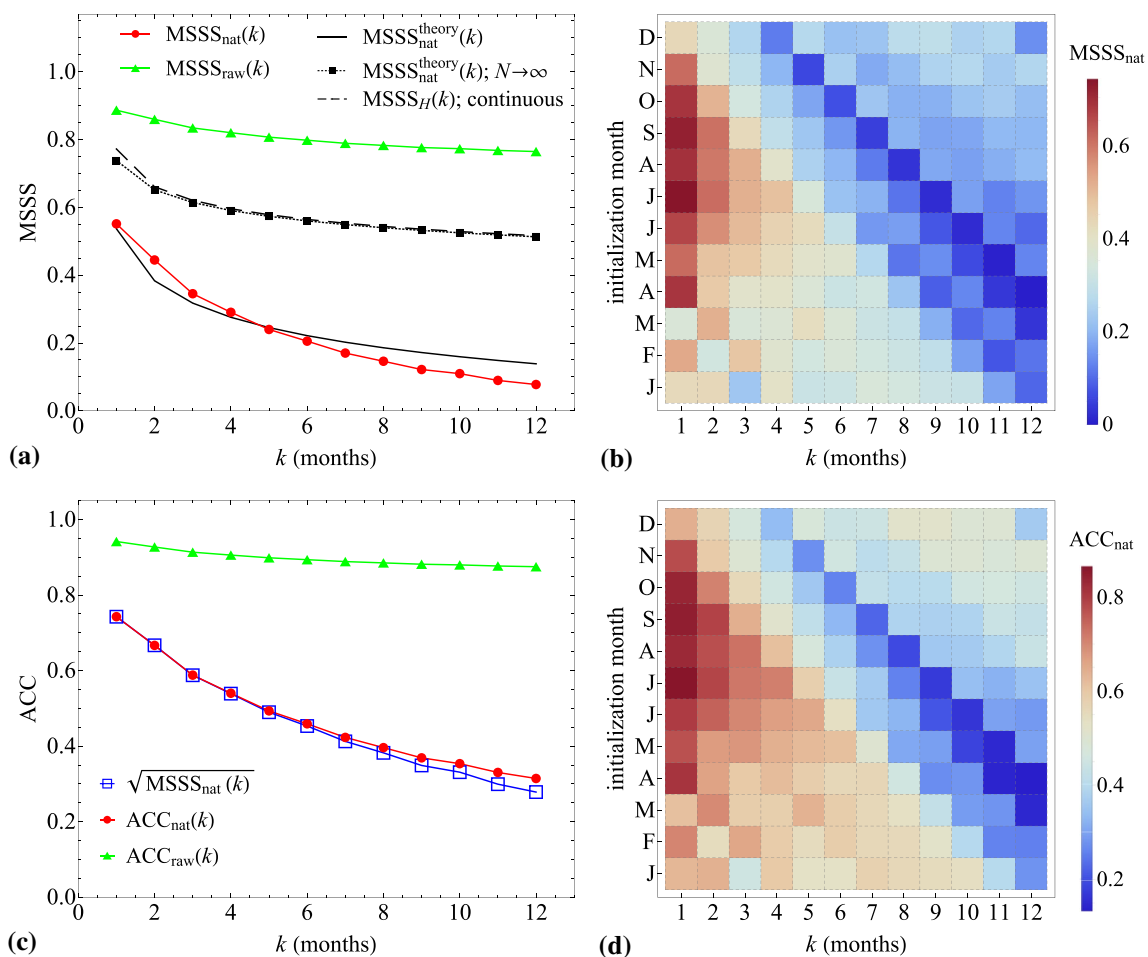


**Fig. 12** MSSS and ACC of StocSIPS forecasts for the Mean-G dataset. **a** Curves of MSSS vs.  $k$  for the Mean-G dataset considering all months in the verification period 1931–2017. In red line with circles, the curve for  $MSSS_{nat}$  taking as reference the anthropogenic trend forecast. In green line with triangles, the values for  $MSSS_{raw}$  taking as reference the climatology forecast. The theoretical expected  $MSSS_{nat}^{theory}(k)$  (solid black), given by Eq. (36), is also shown for comparison. The asymptotic value for  $N \rightarrow \infty$  (given by Eq. (24)) is shown in dotted line with squares (dashed line for the continuous-time case, Eq. (13)). The longer the verification period the closer

will be the MSSS to that asymptotic value. **b** Density plot showing the MSSS as a function of the forecast horizon and the initialization month. **c** Curves of  $ACC_{nat}$  (red circles) and  $ACC_{raw}$  (green triangles) as a function of the forecast horizon obtained from Eq. (37). The values of  $\sqrt{MSSS_{nat}}$  (blue squares) were included to check the consistency of the theoretical relationship given by Eq. (38). **d** Density plot of the ACC as a function of the forecast horizon and the initialization month. The diagonal patterns from the top-left corner to the bottom-right in **b**, **d** are consequences of the intrinsic seasonality in the time-series

In Fig. 12c, we show curves of  $ACC_{nat}$  (red circles) and  $ACC_{raw}$  (green triangles) obtained from Eq. (37). Here, we can appreciate the spuriously high correlation values of  $ACC_{raw}$  compared to the  $ACC_{nat}$  due to the presence of the anthropogenic trend. The values of  $\sqrt{MSSS_{nat}}$  (blue squares) were included to check the consistency of the theoretical relationship given by Eq. (38); we see that it is relatively well satisfied, confirming the validity of the model.

In the right panels of Fig. 12, we show density plots with the MSSS and the ACC [panels (b) and (d), respectively] as a function of the forecast horizon and the initialization month. As we already showed for the RMSE, there are diagonal patterns from the top-left corner to the bottom-right as a consequence of the seasonality in the globally-averaged

temperature anomalies. Nevertheless, for the MSSS and the ACC, these patterns are relatively less significant compared to the ones in the RMSE because—roughly speaking—both scores are functions of the ratio  $RMSE_{nat}/SD_T$ , reducing the impact of the variation of the standard deviation of each individual month (see Fig. 11c). Some results of the hindcast validation are summarized in Table 7 for the twelve datasets, including the mean series for the global and the land surface.

### 3.4.4 Parametric probability forecast

Probability forecasts from long-term prediction dynamical models are usually obtained by fitting probability

1185 distributions to the ensemble forecast for each month and  
 1186 deriving probabilities of three climatologically equiprobable  
 1187 categories: below normal, near normal and above normal  
 1188 conditions. In general, the form of the distribution and the  
 1189 skill of the forecast is affected by the size of the ensemble.  
 1190 One of the main advantages of StocSIPS over conventional  
 1191 numerical models is that, by its inherent stochastic nature,  
 1192 the infinite ensemble parametric probability forecast can be  
 1193 obtained analytically without the need of simulating any  
 1194 individual realization. Following the results presented in  
 1195 Sect. 2, the theoretical probability distribution forecast at  
 1196 horizon  $k$ , taking data up to time  $t$ , is a Gaussian with mean  
 1197  $\mu_f = \hat{T}(t+k)$  given by Eq. (29) and standard deviation  
 1198  $\sigma_f(k) = \text{RMSE}_{H,\sigma_T}^m(k)$  given by Eq. (32) (we neglected the  
 1199 error in the projection of the anthropogenic trend). In this  
 1200 section we only consider results for the full time series with-  
 1201 out stratification of the data. The theoretical expression for  
 1202  $\sigma_f(k)$ , obtained from the results for an infinite ensemble, only  
 1203 applies in this case.

1204 The “reliability” is defined as the consistency or repeat-  
 1205 ability of the probabilistic forecast. In order to evaluate  
 1206 the reliability of the probabilistic forecast of an ensemble  
 1207 model, the ensemble spread score (ESS) is commonly used  
 1208 as a summarizing metric. The ensemble spread score (ESS)  
 1209 is defined as the ratio between the temporal mean of the  
 1210 intra-ensemble variance,  $\sigma_{\text{ensemble}}^2$ , and the mean square error  
 1211 between the ensemble mean and the observations (Palmer  
 1212 et al. 2006; Keller and Hense 2011; Pasternack et al. 2018):

$$1213 \text{ESS} = \frac{\sigma_{\text{ensemble}}^2}{\text{MSE}}. \quad (39)$$

1214 In the case of StocSIPS,  $\sigma_{\text{ensemble}}^2 = \sigma_f^2$  is obtained analyti-  
 1215 cally using Eq. (32) and  $\text{MSE} = \text{RMSE}^2$  is obtained from  
 1216 the hindcasts using Eq. (33).

1217 Following Palmer et al. (2006), an ESS of 1 indicates  
 1218 perfect reliability. The forecast is “overconfident” when  
 1219  $\text{ESS} < 1$ ; i.e. the ensemble spread underestimates forecast  
 1220 error. If the ensemble spread is greater than the model error  
 1221 ( $\text{ESS} > 1$ ), the forecast is “overdispersive” and the forecast  
 1222 spread overestimates forecast error. In Fig. 11a, we showed  
 1223 that there is good agreement between the theoretical estimate  
 1224  $\text{RMSE}_{H,\sigma_T}^m(k) = \sigma_f(k)$  and the hindcast error  $\text{RMSE}_{\text{nat}}(k)$  for  
 1225 all horizons  $k$ , or—what is the same—between  $\sigma_{\text{ensemble}}^2$  and  
 1226 MSE in Eq. (39). This gives a value of  $\text{ESS} \approx 1$ , so that Stoc-  
 1227 SIPS is a nearly perfectly reliable system without needing a  
 1228 recalibration of the forecast probability distribution.

1229 Examples of probability forecasts for July 1984 for the  
 1230 natural variability component of the Mean-G dataset are  
 1231 shown in Fig. 13 for horizons  $k = 1$  and 3 months (left and  
 1232 right panels, respectively). That is, using data up to June  
 1233 1984 for the  $k = 1$  month forecast and up to April 1984 for

1234  $k = 3$  months. The normal probability density function  
 1235 (PDF) in grey represents the climatological distribution of  
 1236 the monthly temperatures for the detrended anomalies of the  
 1237 Mean-G dataset for the full period 1931–2017, for which  
 1238  $\sigma_{\text{clim}} = \text{SD}_T = 0.147$  °C. The terciles of the climatological  
 1239 distribution are indicated by vertical dashed lines. These  
 1240 vertical lines define three equiprobable categories of above  
 1241 normal, near normal, and below normal monthly tempera-  
 1242 tures observed in the verification period. The forecast distri-  
 1243 bution is indicated by the black curve with the forecast mean  
 1244  $\mu_f = \hat{T}(\text{Jul } 1984) = -0.118$  °C and standard deviation  
 1245  $\sigma_f = \text{RMSE}_{H,\sigma_T}^m(k) = 0.101$  °C for  $k = 1$  month (left panel)  
 1246 and  $\mu_f = -0.063$  °C,  $\sigma_f = 0.122$  °C for  $k = 3$  months (right  
 1247 panel). The areas under the forecast PDF in different colors  
 1248 indicate probabilities of below normal (blue), near normal  
 1249 (yellow), and above normal (pink) temperatures. These prob-  
 1250 abilities are summarized in the top-left corner as bar plots.  
 1251 The climatological probability of 33% is indicated by the  
 1252 horizontal dashed line. The observed temperature for that  
 1253 specific date,  $T_{\text{obs}} = -0.191$  °C, is represented by the verti-  
 1254 cal green line. The forecast distributions for  $k = 1$  month are  
 1255 sharper than for  $k = 3$  months. As expected, the confidence  
 1256 of the probabilistic forecast decreases as the lead time  
 1257 increases and they become more conservative.

1258 The verification of the probabilistic forecast in categories  
 1259 (above, near and below normal) is done using  $3 \times 3$  contin-  
 1260 gency tables (Stanski et al. 1989). The forecast and observed  
 1261 categories are simply classified in a table of three rows and  
 1262 three columns. There is a row for each observed category  
 1263 and a column for each forecast category. For each month  
 1264 forecast, one is added to the grid element of the contingency  
 1265 table according to the intersection of the forecast category  
 1266 and the observed category. In Table 1 we show the contin-  
 1267 gency table for the  $k = 1$  month forecast of the natural vari-  
 1268 ability anomalies,  $T_{\text{nat}}$ , of the Mean-G dataset (red curves  
 1269 in Fig. 10). The 1044 month period (Jan 1931–Dec 2017)  
 1270 was used for verification. The climatological distribution  
 1271 was defined using the mean and standard deviation of the  
 1272 detrended series over that period.

1273 There are many scores that can be obtained from the  
 1274 contingency table (Stanski et al. 1989). In this paper we  
 1275 used the percent correct (PC) obtained from the ele-  
 1276 ments in the main diagonal (shown in bold in Table 3).  
 1277 This score, often called accuracy, is very intuitive and it  
 1278 counts, overall, the percentage of the category forecasts  
 1279 that were correct. From Table 1, we obtain the values  
 1280  $\text{PC}_{\text{nat}} = 100(272 + 160 + 250)/1044 \approx 65\%$ . We can obtain  
 1281 contingency tables for all  $k$ . The dependence of the PC with  
 1282  $k$ , is shown in Fig. 14 for the forecasts of the detrended  
 1283 anomalies,  $T_{\text{nat}}$  (blue line with squares in the figure). The  
 1284 dashed line at 33.3% is a reference showing the skill of the  
 1285 climatological forecast.

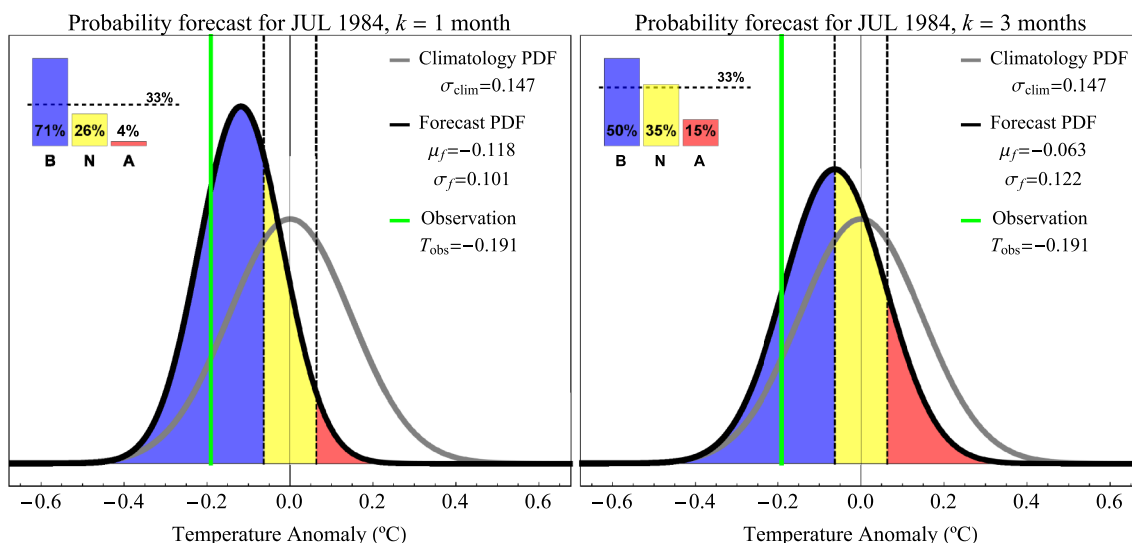


**Fig. 13** Example of parametric probability forecasts for July 1984 for the natural variability component of the Mean-G dataset for horizons  $k = 1$  and 3 months (left and right panels, respectively). That is, using data up to June 1984 for the  $k = 1$  month forecast and up to April 1984 for  $k = 3$  months. The normal probability density function in grey represents the climatological distribution of the monthly temperatures for the detrended anomalies of the Mean-G dataset for the full period 1931–2017. The terciles of the climatological distribution are

indicated by vertical dashed lines. The colored areas under the forecast density function are proportional to the forecast probabilities for each category: below normal (blue), near normal (yellow) and above normal (pink). These probabilities are summarized in the top-left corner as bar plots. The climatological probability of 33% is indicated by the horizontal dashed line. The observed temperature for that specific date,  $T_{obs} = -0.198$  °C, is represented by the vertical green line. The parameters for all the distributions are included in the legends

**Table 1** Contingency table for the  $k = 1$  month forecast of the natural variability anomalies,  $T_{nat}$ , of the Mean-G dataset (red curves in Fig. 10)

| Contingency table for the detrended anomalies, $T_{nat}$ | Forecasts  |            |            | Total       |
|--|------------|------------|------------|-------------|
|  | Below      | Normal     | Above      |             |
| Observations   |            |            |            |             |
| Below  | <b>272</b> | 77         | 9          | 358         |
| Normal   | 102        | <b>160</b> | 90         | 352         |
| Above  | 15         | 69         | <b>250</b> | 334         |
| Total  | 389        | 306        | 349        | <b>1044</b> |

The 1044 months period (Jan 1931–Dec 2017) was used for verification. The climatological distribution was defined using the mean and standard deviation of the detrended series over that period ( $\sigma_{clim} = SD_T = 0.147$  °C)

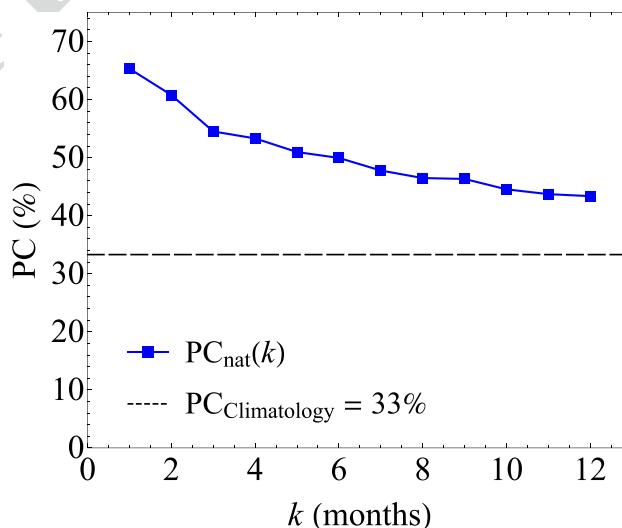


**Fig. 14** PC as a function of  $k$  for the forecasts of the detrended anomalies,  $T_{nat}$  (blue line with squares in the figure). The dashed line at 33.3% is a reference showing the skill of the climatological forecast

1286 The thresholds for the three equiprobable categories,  
 1287 above normal, near normal and below normal, will depend  
 1288 on the base-line of zero temperature and the standard deviation  
 1289 of the reference climatological distribution used. This  
 1290 will affect the distribution of events in the contingency table  
 1291 and consequently, the PC score obtained even though the  
 1292 forecast system has not changed. In that sense, the PC is a  
 1293 relative score. To avoid this dependence we could use absolute  
 1294 scores (independent of the climatology used), such as  
 1295 the ignorance score or the continuous ranked probability  
 1296 score (CRPS) (Hersbach 2000; Gneiting et al. 2005). The

latter is the one we used in this paper for evaluating the quality of the probability forecasts of StocSIPS.

The CRPS for a forecast initialized at time  $t$  with horizon  $k$  is defined as:

$$\text{crps}(t+k) = \int_{-\infty}^{\infty} [P_f(t+k, x) - P_o(t+k, x)]^2 dx, \quad (40)$$

where  $P_f(t, x)$  is the cumulative forecast distribution with mean  $\mu_f = \hat{T}(t+k)$  given by Eq. (29) and standard deviation  $\sigma_f(k) = \text{RMSE}_{H, \sigma_T}^m(k)$  and  $P_o(t+k, x) = H[x - T_{\text{obs}}(t+k)]$  is the cumulative observed distribution defined in terms of the Heaviside function  $H(x)$ . The CRPS can be determined for a single forecast, but a more accurate value is determined from a temporal average of many forecasts. The time mean CRPS as a function of horizon  $k$  is:

$$\text{CRPS}(k) = \frac{1}{N-k+1} \sum_{t=0}^{N-k} \text{crps}(t+k). \quad (41)$$

The CRPS is a negatively oriented measure of forecast accuracy, similar to the RMSE for deterministic ensemble mean forecasts; that is, smaller values indicate better skill. In fact, for deterministic forecasts, where  $\sigma_f \rightarrow 0$ , the crps in Eq. (40) reduces to the absolute error:  $\text{AE} = |T_{\text{obs}} - \hat{T}|$ . If we assume that  $P_f$  is the cumulative distribution function (CDF) of a normal distribution with mean  $\mu_f$  and standard deviation  $\sigma_f$ , a closed form for crps can be derived by repeatedly integrating by parts in Eq. (40) (Gneiting et al. 2005):

$$\text{crps}(t+k) = \sigma_f \left\{ \frac{T_{\text{obs}} - \mu_f}{\sigma_f} \left[ 2\Phi\left(\frac{T_{\text{obs}} - \mu_f}{\sigma_f}\right) - 1 \right] + 2\varphi\left(\frac{T_{\text{obs}} - \mu_f}{\sigma_f}\right) - \frac{1}{\sqrt{\pi}} \right\}, \quad (42)$$

where  $\varphi(\cdot)$  and  $\Phi(\cdot)$  denote the PDF and the CDF, respectively, of the normal distribution with mean 0 and variance 1 evaluated at the normalized prediction error,  $\varepsilon_n = (T_{\text{obs}} - \mu_f)/\sigma_f$ . This expression is very useful for obtaining the CRPS of large or many verification series and for calibrating ensemble forecasts from its optimization. In this paper, we will use it for deriving a general result that relates the CRPS with the RMSE of the ensemble mean of Gaussian probability forecasts.

Let us assume that the ensemble-mean forecast error,  $\varepsilon = T_{\text{obs}} - \mu_f$ , follows a Gaussian distribution with zero mean and standard deviation  $\sigma_\varepsilon$ . Notice that  $\sigma_f \neq \sigma_\varepsilon$ ; the former is given by the intra-ensemble spread,  $\sigma_f = \sigma_{\text{ensemble}}$ , and the latter can be estimated from the RMSE between ensemble mean and observation. The CRPS and the RMSE can be related by averaging Eq. (42) for all possible values of the error,  $\varepsilon$ :

$$\langle \text{crps}(t+k) \rangle_\varepsilon = \int_{-\infty}^{\infty} \varphi\left(\frac{\varepsilon}{\sigma_\varepsilon}\right) \text{crps}(t+k) d\left(\frac{\varepsilon}{\sigma_\varepsilon}\right), \quad (43)$$

where  $\varphi(\cdot)$  is defined as in Eq. (42). If we now replace Eq. (42) in Eq. (43) and integrate by parts, we obtain:

$$\langle \text{crps}(t+k) \rangle_\varepsilon = \frac{\sigma_\varepsilon}{\sqrt{\pi}} \left[ \sqrt{2\left(1 + \sigma_f^2/\sigma_\varepsilon^2\right)} - \sigma_f/\sigma_\varepsilon \right]. \quad (44)$$

The average for all possible values of the error,  $\langle \cdot \rangle_\varepsilon$ , can be approximated by the time average, Eq. (41), for long enough verification periods. Moreover, we can approximate  $\sigma_f$  and  $\sigma_\varepsilon$  by their corresponding time-average estimates:

$\sigma_f^2 \approx \overline{\sigma_{\text{ensemble}}^2}$  and  $\sigma_\varepsilon = \text{RMSE}$ . Using the definition of ESS =  $\overline{\sigma_{\text{ensemble}}^2}/\text{MSE}$  (Eq. (41)), we can finally rewrite Eq. (44) as:

$$\text{CRPS}(k) = \frac{\text{RMSE}(k)}{\sqrt{\pi}} \lambda(\text{ESS}), \quad (45)$$

where  $\lambda(\text{ESS}) = \sqrt{2(1 + \text{ESS})} - \sqrt{\text{ESS}}$ . The function  $\lambda(\text{ESS})$  takes the minimum value  $\lambda_{\text{min}} = 1$  for a system with perfect reliability where  $\text{ESS} = 1$ . For any other value of ESS,  $\text{CRPS} > \text{RMSE}/\sqrt{\pi}$ . This result shows that, for ensemble prediction systems, the optimal way of producing parametric probabilistic forecasts, assuming a Gaussian distribution, is by calculating the standard deviation of the forecast distribution from the hindcast period rather than just from the current forecast ensemble. This result agrees with previous studies (Kharin and Zwiers 2003; Kharin et al. 2009, 2017), which reach the same conclusion from the optimization of other standard probabilistic skill measures (e.g., the Brier skill score).

As we mentioned before, StocSIPS is a system with nearly perfect reliability and it assumes, by hypothesis, the Gaussianity of the errors. In that sense, the analytical expression for  $\text{RMSE}_{H, \sigma_T}^m(k)$  (Eq. (32)) can be used to obtain a theoretical expression for  $\text{CRPS}(k)$  in Eq. (45). At the same time, the verification of this expression through a comparison between the values of  $\text{RMSE}(k)$  and  $\text{CRPS}(k)$  obtained from hindcasts can be used to check the validity of the model.

In Fig. 15 we show the time mean CRPS as a function of  $k$ , calculated in the verification period 1931–2017 for the probabilistic forecast of the monthly temperature anomalies of the Mean-G dataset. In the figure we show the results of the forecast of the raw anomalies (red circles), for which both the natural variability and the anthropogenic trend have to be forecast. Similarly to the previous results for the RMSE, the difference with the score of the forecast of the detrended anomalies is negligible ( $\text{CRPS}_{\text{raw}} \approx \text{CRPS}_{\text{nat}}$ ), corresponding to the very small error on the projection of the trend compared to the error on the prediction of the detrended anomalies. The line in blue with empty squares, almost coincident with the red line, shows the function



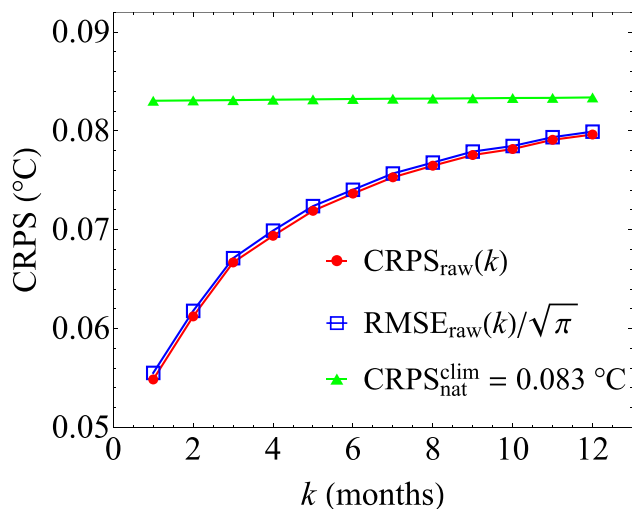


**Fig. 15** CRPS as a function of the forecast horizon,  $k$ , calculated in the verification period 1931–2017 for the probabilistic forecast of the monthly temperature anomalies of the Mean-G dataset. In red circles we show the CRPS for the forecast of the raw anomalies, for which both the natural variability and the anthropogenic trend have to be forecast. The line in blue with squares, almost coincident with the red line, shows the function  $\text{RMSE}_{\text{raw}}(k)/\sqrt{\pi}$ , in perfect agreement with the theoretical prediction for the optimal value  $\lambda_{\min} = 1$  in Eq. (45). In green triangles we included the CRPS of the reference climatology forecast of the detrended anomalies,  $\text{CRPS}_{\text{nat}}^{\text{clim}} = 0.083 \text{ } ^\circ\text{C}$

1383  $\text{RMSE}_{\text{raw}}(k)/\sqrt{\pi}$ , in perfect agreement with the theoretical  
 1384 prediction for the optimal value  $\lambda_{\min} = 1$  in Eq. (45), cor-  
 1385 responding to perfect reliability. In the green triangles we  
 1386 included the CRPS of the reference climatology forecast of  
 1387 the natural variability component ( $\text{CRPS}_{\text{nat}}^{\text{clim}} = 0.083 \text{ } ^\circ\text{C}$ ).  
 1388 That is, using the fixed climatological probability distribu-  
 1389 tion (shown in grey in Fig. 13), with zero mean and standard  
 1390 deviation  $\sigma_{\text{clim}} = 0.147 \text{ } ^\circ\text{C}$ , to forecast the detrended anomalies.  
 1391 If we use the same climatological distribution for fore-  
 1392 casting the raw anomalies, we obtain the much larger value  
 1393  $\text{CRPS}_{\text{raw}}^{\text{clim}} = 0.181 \text{ } ^\circ\text{C}$ .

### 1394 3.5 Comparison with GCMs

1395 According to the World Meteorological Organization  
 1396 (WMO) (<http://www.wmo.int/pages/prog/wcp/wcas/gpc/gpc.php>), there are currently fifteen major centers providing  
 1397 global seasonal forecasts. Thirteen of them have been offi-  
 1398 cially designated by the WMO as Global Producing Centres  
 1399 for Long-Range Forecasts (GPCLRFs). The Meteorological  
 1400 Service of Canada (MSC) contributes with the Canadian  
 1401 Seasonal to Interannual Prediction System (CanSIPS) (Mer-  
 1402 riefeld et al. 2011, 2013).

1404 CanSIPS is a multi-model ensemble (MME) sys-  
 1405 tem using 10 members from each of two climate models

(CanCM3 and CanCM4) developed by the Canadian Cen-  
 1406 tre for Climate Modelling and Analysis (CCCma) for a  
 1407 total ensemble size of 20 realizations. It is a fully coupled  
 1408 atmosphere–ocean–ice–land prediction system relying  
 1409 on operational data assimilation for the initial state of the  
 1410 atmosphere, sea surface temperature and sea ice.  
 1411

To evaluate forecasts and compare StocSIPS with Can-  
 1412 SIPS, we accessed the publicly available series of hindcasts  
 1413 of CanSIPS covering the period 1981–2010 (CanSIPS 2016).  
 1414 The fields, available on  $145 \times 73$  latitude–longitude grids at  
 1415 resolutions of  $2.5^\circ \times 2.5^\circ$  for each of the 20 ensemble mem-  
 1416 bers, were area-weight averaged to obtain global mean series  
 1417 of hindcasts at monthly resolution. CanSIPS produces fore-  
 1418 cast at the beginning of every month for the average value of  
 1419 that month and the next 11 months; i.e. for lead times from  
 1420 0 to 11 months for each initialization date. In our case, that  
 1421 would correspond to forecast horizons (number of periods  
 1422 ahead that are forecasted) from 1 to 12 months. In the ver-  
 1423 ification for  $k = 1$  month (lead zero), the hindcast period is  
 1424 January 1981–December 2010; for  $k = 2$  months (lead one),  
 1425 the hindcast period is February 1981–January 2011, and so  
 1426 on. This way, all the 12 series of hindcasts (one for each  
 1427 horizon) have a length of 360 months.  
 1428

An optimal use of the dynamical model can be obtained  
 1429 after advanced postprocessing and calibration to reduce the  
 1430 bias of the model (Crochemore et al. 2016; Kharin et al.  
 1431 2017; Van Schaeybroeck and Vannitsem 2018; Pasternack  
 1432 et al. 2018). We do not pretend here to make an exhaustive  
 1433 use of these calibration techniques. To keep the compari-  
 1434 son simple, we followed the postprocessing for CanSIPS  
 1435 described in Sects. 3.a and 3.b of (Kharin et al. 2017) for  
 1436 deterministic and parametric probability forecasts, respec-  
 1437 tively. The statistical adjustment used by the authors is based  
 1438 on a linear rescaling of the ensemble mean and standard  
 1439 deviation of the anomaly forecast. The regression coeffi-  
 1440 cients are obtained by minimizing the MSE and CRPS of  
 1441 the ensemble forecast in some verification period.  
 1442

It can be easily shown that, after the recalibration, their  
 1443 method will lead to the optimal expression for CRPS given  
 1444 by Eq. (45) when  $\text{ESS} = 1$ :  $\text{CRPS} = \text{RMSE}/\sqrt{\pi}$ . The recal-  
 1445 ibration method can be reduced to using—as optimal deter-  
 1446 ministic predictor—the projection of the ensemble mean that  
 1447 minimizes the MSE in some verification period. Then, for  
 1448 the probability distribution forecast, the standard deviation  
 1449 is made equal to the RMSE of the adjusted deterministic  
 1450 forecast instead of calculating it from the intra-ensemble  
 1451 spread. In that sense, the ensemble members are only useful  
 1452 for obtaining the ensemble mean. They do not contribute  
 1453 further to the forecast as the optimal probabilistic scores are  
 1454 obtained from the condition  $\text{ESS} = 1$ .  
 1455

In their paper, (Kharin et al. 2017) also show that the opti-  
 1456 mal average skill scores are obtained when time-invariant  
 1457 (independent of the season) coefficients are used. We will  
 1458

1459 use this result here and, instead of using only 30 years for  
 1460 estimating individual coefficients for each month, we use  
 1461 the monthly series to estimate constant coefficients based  
 1462 on 360 months that only depend on the lead time. These  
 1463 coefficients are more stable and do not significantly degrade  
 1464 the accuracy of the forecast due to sampling errors as would  
 1465 season-dependent coefficients.

1466 In Fig. 16, we show an example of a forecast for the  
 1467 12 months following April 1982 for both StocSIPS and  
 1468 CanSIPS. In red we show the verification curve of obser-  
 1469 vations for the Mean-G dataset. In blue, the median hind-  
 1470 casts for StocSIPS, with the corresponding 95% confidence  
 1471 interval based on the RMSE for the verification period. The  
 1472 ensemble mean for CanSIPS is shown in black, with each  
 1473 of the 20 members shown in dashed light colors and the  
 1474 95% confidence interval based on the RMSE of the hindcasts  
 1475 represented in grey. The CO<sub>2</sub>eq trend for the Mean-G dataset  
 1476 (green line) was added as a reference of the long-term equi-  
 1477 librium of the temperature fluctuations.

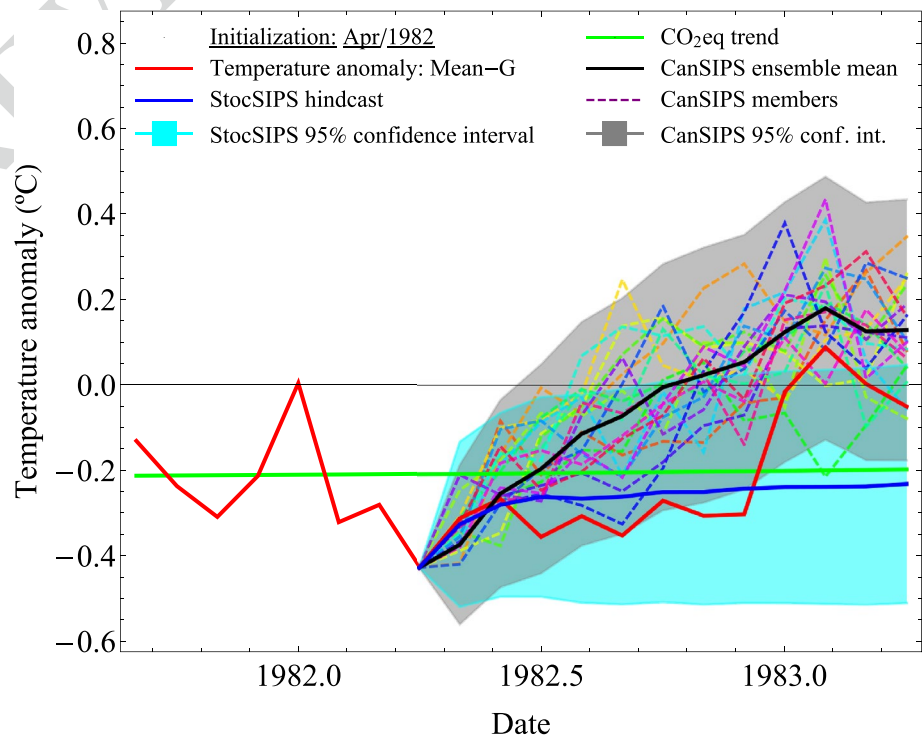
1478 As expected, the dispersion of the different ensemble  
 1479 members for the dynamical model increases as the hori-  
 1480 zon increases, which shows the stochastic-like character of  
 1481 GCMs for long-term predictions with the consequent loss  
 1482 in skill. Despite this increase in the spread of the ensemble,  
 1483 the dynamical model is underdispersive for all horizons. The  
 1484 ESS (see Eq. (39) in Sect. 3.4.4) is in the range 0.57–0.74  
 1485 for all lead times, except for zero months lead time where ESS =  
 1486 0.40. (Kharin et al. 2017) show that inflating the ensemble  
 1487 spread to satisfy the condition ESS = 1, results in more

1488 conservative estimates for the forecast probabilities of the  
 1489 three categories and improved reliability of the probability  
 1490 forecast and overall probabilistic skill scores.

### 1491 3.5.1 Deterministic forecast comparison and seasonality

1492 In this section we present scores for the deterministic fore-  
 1493 cast (ensemble mean forecast) for both models using for  
 1494 verification the Mean-G dataset in the period 1981–2010. In  
 1495 all cases we used the calibrated ensemble mean for CanSIPS,  
 1496 unless stated otherwise. In Fig. 17, we show density plots  
 1497 of the RMSE as a function of the forecast horizon and the  
 1498 initialization month for StocSIPS and CanSIPS [panels (a)  
 1499 and (b), respectively]. For both models, there is a seasonality  
 1500 pattern with large errors during the Boreal winter months.  
 1501 In the case of StocSIPS, the largest values of the RMSE are  
 1502 found for February, January and March, in that order, while  
 1503 CanSIPS has the largest errors for the forecasts of November  
 1504 and February. In Fig. 17c, we show the difference between  
 1505 CanSIPS RMSE and StocSIPS RMSE; positive values indi-  
 1506 cate that StocSIPS has better skill. StocSIPS outperforms  
 1507 CanSIPS for most of the horizons and initialization months,  
 1508 except for the forecasts of January and February and some  
 1509 other initialization dates for  $k = 1$  month. The overall values  
 1510 of RMSE vs.  $k$ —averaging for all the months in the verifi-  
 1511 cation period independently of the initialization date—are  
 1512 shown in Fig. 17d. The curve for StocSIPS is represented in  
 1513 red line with solid squares. For CanSIPS, we show in solid  
 1514 blue line with empty squares the RMSE for the calibrated

**Fig. 16** One example of forecast for the 12 months following April 1982 for both StocSIPS and CanSIPS. In red we show the verification curve of observations for the Mean-G dataset. In blue, the median hindcasts for StocSIPS, with the corresponding 95% confidence interval based on the RMSE for the verification period. The ensemble mean for CanSIPS is shown in black, with each of the 20 members shown in dashed light colors and the 95% confidence interval based on the RMSE of the hindcasts represented in grey. The CO<sub>2</sub>eq trend for the Mean-G dataset (green line) was added as a reference of the long-term equilibrium of the temperature fluctuations



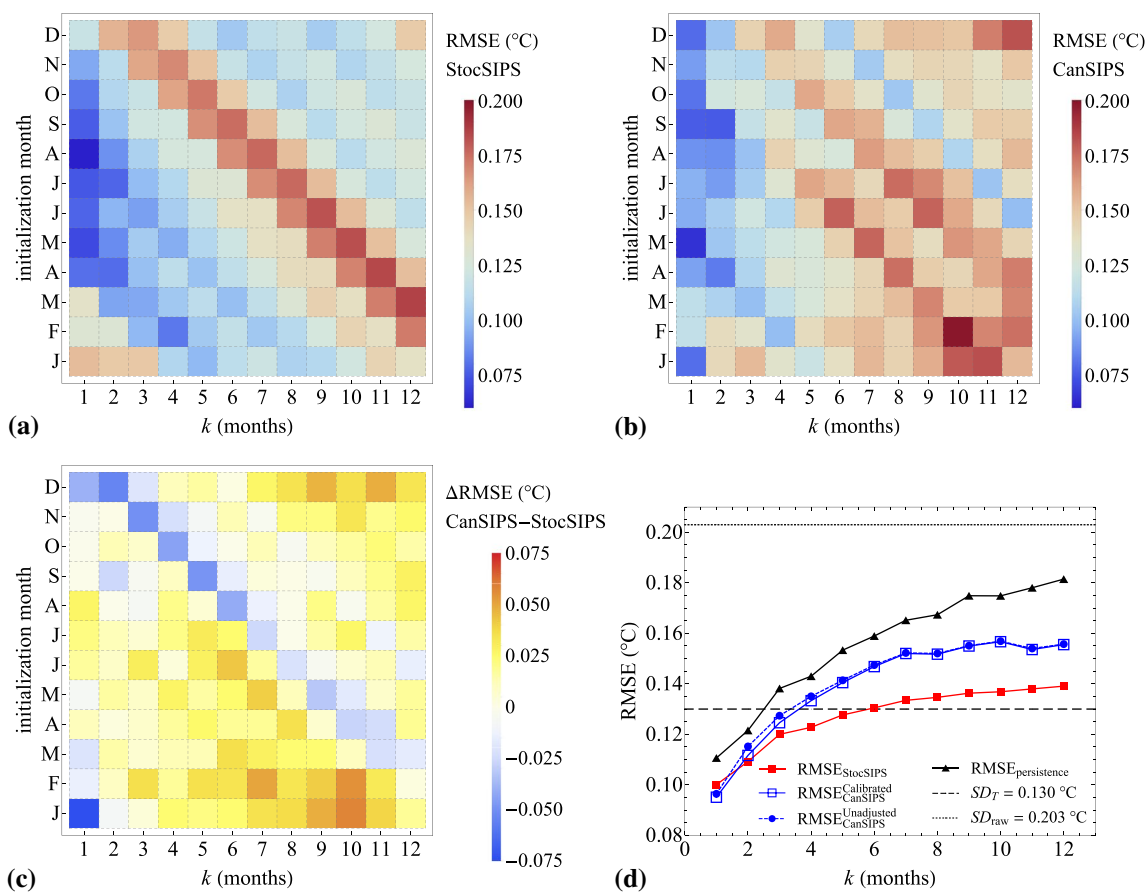


**Fig. 17** Density plots of the RMSE as a function of the forecast horizon,  $k$ , and the initialization month for StocSIPS and CanSIPS (a, b, respectively). For both models, there is a seasonality pattern with large errors during the Boreal winter months. In c, we show the difference between CanSIPS and StocSIPS RMSE; positive values indicate that StocSIPS has better skill. StocSIPS outperforms CanSIPS for most of the horizons and initialization months, except for the forecasts of January and February and some other initialization dates for  $k = 1$  month. The overall values of RMSE vs.  $k$ —averaging for all the months in the verification period independently of the initialization

date—are shown in d. The curve for StocSIPS is represented in red squares. For CanSIPS, we show in solid blue line with empty squares the scores for the calibrated ensemble mean and in dashed blue line with solid circles the RMSE for the unadjusted model. We can see that the improvement in the RMSE due to the recalibration is very small. We included, for comparison, the curve obtained from hindcasts using persistence (black-triangles). The standard deviations for the detrended and for the raw series in the verification period were also included for reference ( $SD_T$  and  $SD_{raw}$ , respectively)

1515 ensemble mean and in dashed blue line with solid circles  
 1516 the values for the unadjusted model. We can see that the  
 1517 improvement in the RMSE due to the recalibration is very  
 1518 small. We included, for comparison, the curves obtained  
 1519 from hindcasts using persistence (black-triangles). That is,  
 1520 for horizon  $k$ , assuming that the temperature  $k$  months into  
 1521 the future is predicted by the present value. The standard  
 1522 deviations for the detrended and for the raw series in the  
 1523 verification period were also included for reference ( $SD_T$   
 1524 and  $SD_{raw}$ , respectively).

1525 Similar results are reported in Fig. 18 for the MSSS and  
 1526 for the ACC. From the density plots [panels (a) and (c)]  
 1527 we can reach the same conclusion based on these scores:  
 1528 StocSIPS is better than CanSIPS for most of the horizons  
 1529 and initialization months, except for the forecasts of January

and February. In panels (b) and (d), we show the all-months  
 1530 average scores without considering the initialization dates.  
 1531 The results for StocSIPS are shown in red line with solid  
 1532 squares and for CanSIPS in blue line with circles. In the  
 1533 MSSS graphs, we only show the results for the calibrated  
 1534 model. For the ACC, as the calibration for CanSIPS is just  
 1535 a rescaling of the ensemble mean, the correlations with or  
 1536 without the calibration are the same. The curves obtained  
 1537 from hindcasts using persistence were also included for com-  
 1538 parison (black-triangles).  
 1539

For the MSSS, we choose the climatology as reference  
 1540 forecast with  $MSE_{ref} = SD_{raw}^2$  being the variance of the raw  
 1541 series. We use accordingly the notation  $MSSS = MSSS_{raw}$ .  
 1542 The horizontal line (green empty squares) included  
 1543 in the graph represents the value of skill obtained by  
 1544

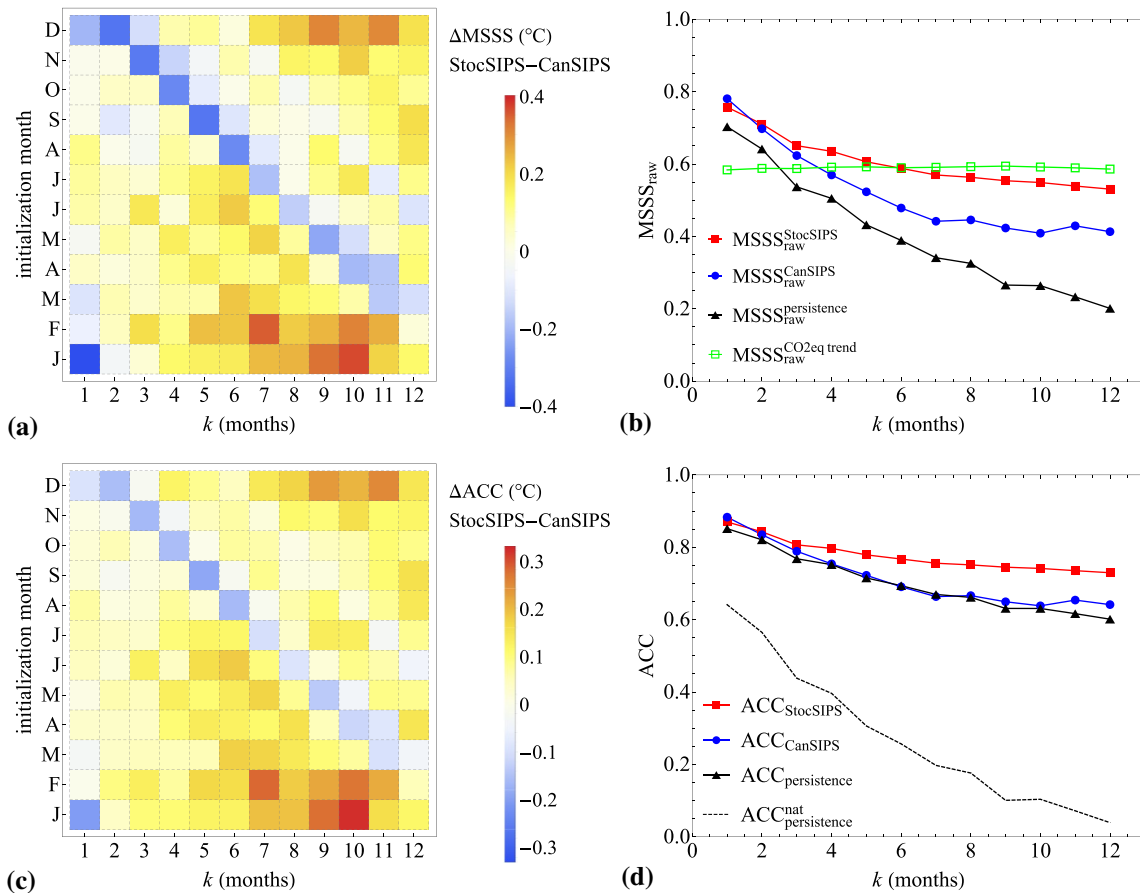


**Fig. 18** Density plots for the MSSS and for the ACC (a, c, respectively) as a function of the forecast horizon and the initialization date. The positive values indicate that StocSIPS is better than CanSIPS for most of the horizons and initialization months, except for the forecasts of January and February. In b, d, we show the all-months average scores without considering the initialization dates. The results for StocSIPS are shown in red line with solid squares and for CanSIPS in blue line with circles. In the MSSS graphs, we only show the results for the calibrated model. The horizontal line (green line with empty squares) included in the graph represents the value of skill obtained

by projecting the  $\text{CO}_2\text{eq}$  trend with respect to the climatological forecast. For the ACC, as the calibration for CanSIPS is just a rescaling of the ensemble mean, the correlations with or without the calibration are the same. The curves obtained from hindcasts using persistence were also included for comparison (black-triangles). The autocorrelation function for the detrended series (natural variability component), which is the same as the ACC for the forecast of that series using persistence, was included for comparison as a dashed black curve ( $\text{ACC}_{\text{persistence}}^{\text{nat}}$  in the figure)

1545 projecting the  $\text{CO}_2\text{eq}$  trend with respect to the climato-  
 1546 logical forecast. The MSSS can be easily computed as  
 1547  $\text{MSSS}_{\text{raw}}^{\text{CO}_2\text{eq trend}} = 1 - \text{SD}_T^2 / \text{SD}_{\text{raw}}^2$  ( $\approx 0.59$  for the Mean-  
 1548 G dataset) because the errors of the forecast would be the  
 1549 amplitude of the detrended anomalies. The values obtained  
 1550 using this equation do not vary significantly for different  
 1551 horizons in the period analyzed. The extra contribution in  
 1552 the skill for StocSIPS comes from the forecast of the natural  
 1553 variability component.

1554 The ACC, in the case of persistence, is the same as the  
 1555 autocorrelation function with lag  $k$  of the reference series.  
 1556 As mentioned before, the values obtained for the ACC (even  
 1557 for the poor persistence forecasts), are spuriously high due  
 1558 to the anthropogenic trends superimposed on the series.  
 1559 Many authors report similarly high values without taking

1560 this fact into consideration. More realistic values would be  
 1561 obtained for the forecast of the detrended series, but there is  
 1562 no impartial way of removing the anthropogenic component  
 1563 for CanSIPS. The anthropogenic forcing is an intrinsic part  
 1564 of the GCM and to have a prediction of the natural variabil-  
 1565 ity only, we would have to remove its contribution before  
 1566 running the dynamical model. The autocorrelation function  
 1567 for the detrended series (natural variability component),  
 1568 which is the same as the ACC for the forecast of that series  
 1569 using persistence, was included for comparison as a dashed  
 1570 black curve ( $\text{ACC}_{\text{persistence}}^{\text{nat}}$  in the figure).

1571 With respect to the comparison of the two models for  
 1572 the deterministic forecast, the conclusion is clear: StocSIPS  
 1573 presents better skill than CanSIPS on average for all the



1574 measures used and for all horizons except for  $k = 1$  month,   
 1575 where CanSIPS is slightly better. This was expected as, for   
 1576 the case of GCMs, 1 month is still close to the deterministic   
 1577 predictability limit imposed by the chaotic behavior of the   
 1578 system ( $\sim 10$  days for the atmosphere and 1–2 years for the   
 1579 ocean). After 1 month, the relative advantage of StocSIPS   
 1580 increases as the horizon increases. The reduced skill of Stoc-   
 1581 SIPS for January and February are related to the intrinsic   
 1582 seasonality of the globally-averaged temperature. In future   
 1583 work, this seasonality in the variability could be removed   
 1584 by pre-processing, presumably resulting in further error   
 1585 reduction.

### 1586 3.5.2 Probabilistic forecast comparison

1587 In the previous section we showed how the two systems   
 1588 (CanSIPS and StocSIPS) compare for deterministic fore-   
 1589 casts where the scores only depend on the ensemble mean.   
 1590 In Fig. 17d, we showed that the reduction in the RMSE of   
 1591 CanSIPS due to the recalibration is very small. In this sec-   
 1592 tion we show how this improvement is more noticeable if   
 1593 probabilistic scoring rules are used, as they are influenced   
 1594 not only by the ensemble mean, but also by the ensemble   
 1595 spread which is readjusted to maximize the CRPS using the   
 1596 condition  $ESS = 1$  mentioned before.

1597 Examples of probabilistic forecasts for July 1994 are   
 1598 shown in Fig. 19 for StocSIPS (left) and for CanSIPS

1599 (right) for horizon  $k = 2$  months (one month lead time; i.e.   
 1600 using data up to May 1994). The normal PDF in grey rep-   
 1601 represents the climatological distribution of the monthly tem-   
 1602 peratures for the Mean-G dataset for the verification period   
 1603 1981–2010. The terciles of the climatological distribution   
 1604 are indicated by vertical dashed lines. These vertical lines   
 1605 define three equiprobable categories of above normal, near   
 1606 normal, and below normal monthly temperatures observed   
 1607 in the verification period. In the left, the forecast distribu-   
 1608 tion for StocSIPS is indicated by the black curve with the   
 1609 forecast mean  $\mu_f = \hat{T}(\text{July } 1994) = -0.105^\circ\text{C}$  and standard   
 1610 deviation  $\sigma_f = \text{RMSE}_{\text{StocSIPS}} = 0.109^\circ\text{C}$  for  $k = 2$  months.   
 1611 In the right, the distribution in dashed black line repre-   
 1612 sents the unadjusted forecast of CanSIPS for  $k = 2$  months   
 1613 with parameters  $\mu_f = -0.051^\circ\text{C}$  (ensemble mean) and   
 1614  $\sigma_f = \sigma_{\text{ensemble}} = 0.084^\circ\text{C}$  (intra-ensemble standard devia-   
 1615 tion). The calibrated forecast PDF for CanSIPS is shown   
 1616 in solid black in the right panel. The adjusted mean for this   
 1617 distribution is  $\mu_f = -0.062^\circ\text{C}$  and the inflated standard   
 1618 deviation  $\sigma_f = \text{RMSE}_{\text{CanSIPS}}^{\text{Calibrated}} = 0.112^\circ\text{C}$ . The areas   
 1619 under the forecast PDF's in different colors indicate probabilities   
 1620 of below normal (blue), near normal (yellow), and above   
 1621 normal (pink) temperatures. These probabilities are sum-   
 1622 marized in the top-left corner as bar plots. The climato-   
 1623 logical probability of 33% is indicated by the horizontal   
 1624 dashed line. The observed temperature for that specific date,   
 1625  $T_{\text{obs}} = -0.127^\circ\text{C}$ , is represented by the vertical green line.

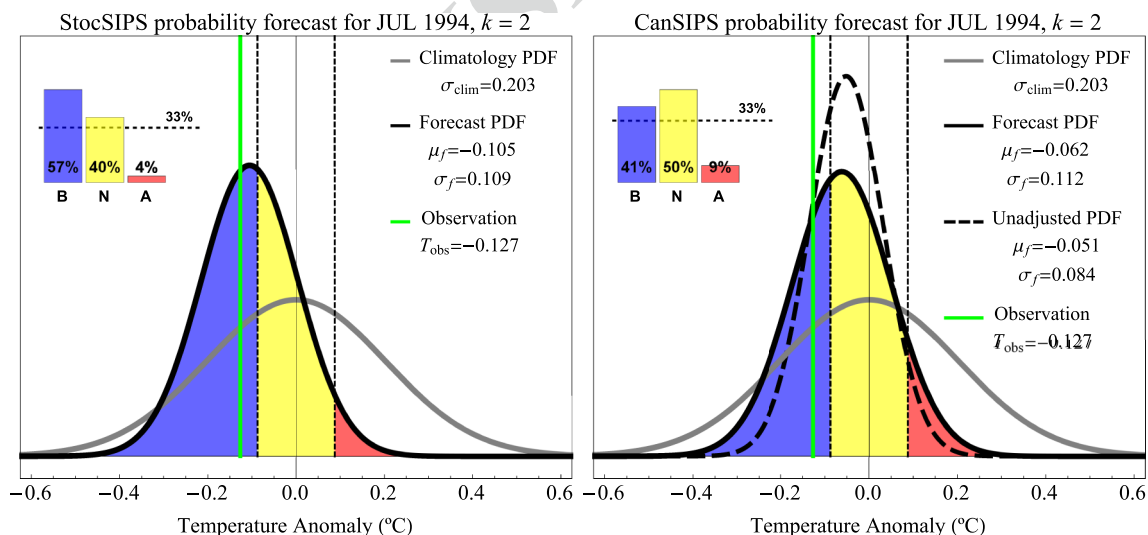


**Fig. 19** Examples of probabilistic forecasts for July 1994 are shown for StocSIPS (left) and for CanSIPS (right) for horizon  $k = 2$  months (1 month lead time; i.e. using data up to May 1994). The normal probability density function in grey represents the climatological distribution of the monthly temperatures for the Mean-G dataset for the verification period 1981–2010. The terciles of the climatological distribution are indicated by vertical dashed lines. The colored areas under the forecast density function are proportional to the forecast probabilities for each category: below normal (blue), near normal

(yellow) and above normal (pink). These probabilities are summarized in the top-left corner as bar plots. The climatological probability of 33% is indicated by the horizontal dashed line. The observed temperature for that specific date,  $T_{\text{obs}} = -0.127^\circ\text{C}$ , is represented by the vertical green line. In the right, the distribution in dashed black line represent the unadjusted forecast of CanSIPS for  $k = 2$  months and the calibrated forecast PDF is shown in solid black. The parameters for all the distributions are included in the legends

For the unadjusted distribution of CanSIPS, the standard deviation for each specific month and lead time is estimated from the intra-ensemble spread and, as the model is underdispersive, it is generally lower than the standard deviation of the calibrated forecast distribution, which is estimated from the whole verification period and is constant for all months for a particular lead time.

The combined contingency table for the forecasts of StocSIPS (grey rows) and CanSIPS (white rows with the values of the unadjusted forecast in parenthesis) for  $k = 1$  month is shown in Table 2. For observational reference we used the Mean-G dataset for verification in the period January 1981–December 2010 (360 months). The number of hits and total number of events are shown in bold in the main diagonal.

The reduced number of observation events in the near-normal category is a consequence of the deviation from Gaussianity of the undetrended anomalies in the verification period 1981–2010. Specifically, there is a reduced kurtosis caused by the presence of the anthropogenic trend, as can be clearly seen in Fig. 5. The distribution of the detrended anomalies,  $T_{\text{nat}}$ , is much closer to a Gaussian (see Appendix 2). In Table 3, we show the contingency table for the forecast of this series using StocSIPS. Now the total number of observations are almost equally distributed among the three categories obtained using the climatological distribution based on the detrended series.

From the diagonal elements in Table 2 we get the following PC scores for  $k = 1$  month: for StocSIPS,  $\text{PC}_{\text{StocSIPS}} \approx 78\%$  and for CanSIPS we get  $\text{PC}_{\text{CanSIPS}}^{\text{Calibrated}} \approx 76\%$  and  $\text{PC}_{\text{CanSIPS}}^{\text{Unadjusted}} \approx 74\%$  for the calibrated and the unadjusted forecasts, respectively. These values are spuriously high due to the presence of the trend in the raw series. Just from direct inspection of the reference series (red curve in Fig. 5), by projecting the trend we could predict that most of the

**Table 3** Contingency table for StocSIPS 3 category probabilistic forecasts (below normal, near normal and above normal) for the detrended series ( $T_{\text{nat}}$ , red curves in Fig. 10) of the Mean-G dataset with zero months lead time ( $k = 1$  month)

| Contingency table for the detrended anomalies, $T_{\text{nat}}$ | Forecasts |           |           | Total      |
|---|-----------|-----------|-----------|------------|
|   | Below     | Normal    | Above     |            |
| Observations  |           |           |           |            |
| Below   | <b>83</b> | 25        | 12        | 120        |
| Normal  | 39        | <b>39</b> | 40        | 118        |
| Above   | 12        | 27        | <b>83</b> | 122        |
| Total   | 134       | 91        | 135       | <b>360</b> |

The verification period is January 1981–December 2010 (360 months). The number of hits and total number of events are shown in bold in the main diagonal. Here we use the climatology obtained from the detrended anomalies with  $\sigma_{\text{clim}} = \text{SD}_T = 0.130$  °C

temperature values in the decade 2001–2010 would fall in the above normal category, while most of the events in the decade 1981–2000 would fall in the below normal category. The PC score obtained from Table 3 for the forecast of the natural variability component with  $k = 1$  month using StocSIPS is more realistic:  $\text{PC}_{\text{StocSIPS}}^{\text{Nat}} \approx 57\%$ . As we mentioned before, we cannot perform a similar forecast using CanSIPS since the anthropogenic forcing is an intrinsic part of the GCM. To obtain a prediction of the natural variability only, we would have to remove its contribution before running the dynamical model.

The PC scores for all horizons from  $k = 1$  to 12 months are shown in Fig. 20. In blue squares we show the PC scores for StocSIPS and in red circles and green triangles for CanSIPS, calibrated and unadjusted forecasts, respectively. The solid black line shows the skill of StocSIPS for the forecast of the detrended series. The values obtained in this case are lower than those obtained for the raw anomalies. Those

**Table 2** Contingency table for 3 category probabilistic forecasts (below normal, near normal and above normal) for the raw (undetrended) Mean-G dataset with zero months lead time ( $k = 1$  month)

| Combined contingency table for the forecasts of StocSIPS (grey rows) and CanSIPS (white rows) for $k = 1$ month. |        |                      | Forecast       |                |                 | Total      |
|--|--------|----------------------|----------------|----------------|-----------------|------------|
|  |        |                      | Below          | Normal         | Above           |            |
| Observations   | Below  | StocSIPS             | <b>102</b>     | 25             | 1               | 128        |
|  |        | CanSIPS (Unadjusted) | <b>99 (95)</b> | 28 (33)        | 1 (0)           |            |
|  | Normal | StocSIPS             | 23             | <b>61</b>      | 18              | 102        |
|  |        | CanSIPS (Unadjusted) | 20 (15)        | <b>69 (74)</b> | 13 (13)         |            |
|  | Above  | StocSIPS             | 2              | 11             | <b>117</b>      | 130        |
|  |        | CanSIPS (Unadjusted) | 0 (0)          | 24 (31)        | <b>106 (99)</b> |            |
| Total  |        | StocSIPS             | 127            | 97             | 136             | <b>360</b> |
|  |        | CanSIPS (Unadjusted) | 119 (110)      | 121 (138)      | 120 (112)       |            |

The verification period is January 1981–December 2010 (360 months). The number of hits and total number of events are shown in bold in the main diagonal. Here we compacted in one table the results for the forecasts of StocSIPS (grey rows) and CanSIPS (white rows with the values of the unadjusted forecast in parentheses)

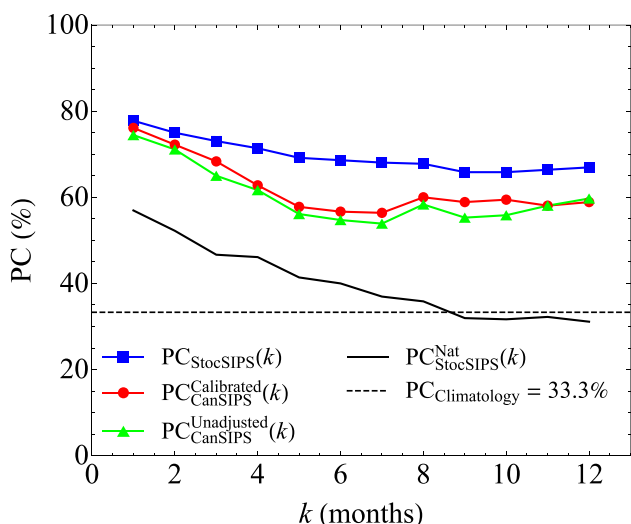


**Fig. 20** PC as a function of  $k$  for StocSIPS (blue squares) and for CanSIPS, calibrated and unadjusted forecasts in red circles and green triangles, respectively. The solid black line shows the skill of StocSIPS for the forecast of the detrended series. The dashed line at 33.3% is a reference showing the skill of the climatological forecast

1679 values are a better measure of the actual quality of the fore-  
 1680 casting system since the spurious effects of the trend are  
 1681 removed. The dashed line at 33.3% is a reference showing  
 1682 the skill of the climatological forecast.

1683 Three main conclusions can be obtained from the analysis  
 1684 of Fig. 20. First, there is an improvement on the probabilistic  
 1685 forecast skill of CanSIPS thanks to the recalibration. This  
 1686 improvement is small but is more noticeable than the one  
 1687 obtained for the deterministic scores (e.g. RMSE, MSSS).  
 1688 Second, StocSIPS performs better than CanSIPS for all lead  
 1689 times and the relative advantage increases with the forecast  
 1690 horizon up to  $k = 7$  months. Finally, from the comparison of  
 1691 the blue and the solid black curves for the StocSIPS forecasts  
 1692 of the raw and the detrended series, respectively, we can  
 1693 notice that most of the skill comes from the projection of the  
 1694 trend and for  $k > 8$  months this is the only source of skill.

1695 Although the PC score for StocSIPS is larger for all hori-  
 1696 zons, it is difficult to evaluate the relative advantage over the  
 1697 probabilistic CanSIPS forecasts based on that score alone.  
 1698 The PC is influenced by the climatological distribution used  
 1699 for defining the categories and mainly by the presence of  
 1700 the trend. A more realistic comparison should be based in  
 1701 absolute scores that only depend on the forecast system and  
 1702 are independent of the base-line or the climatology chosen.  
 1703 The dependence of the CRPS with the forecast horizon is  
 1704 shown in Fig. 21 for both models in the verification period  
 1705 1981–2010 for the Mean-G dataset. In red, we show the  
 1706 CRPS for StocSIPS and in blue for CanSIPS with dotted line  
 1707 and solid circles for the unadjusted forecast and solid line  
 1708 with open squares for the calibrated forecast. The function

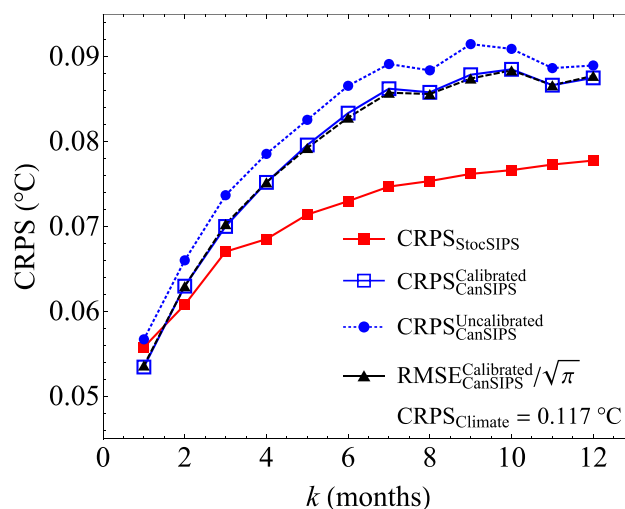


**Fig. 21** CRPS vs.  $k$  for both models in the verification period 1981–2010 for the Mean-G dataset. In red, we show the CRPS for StocSIPS and in blue for CanSIPS with dotted line and solid circles for the unadjusted forecast and solid line with open squares for the calibrated forecast. The function  $RMSE_{CanSIPS}^{Calibrated}(k)/\sqrt{\pi}$  is shown in dashed black line with triangles. There is perfect agreement between these optimal values and the CRPS of CanSIPS after the calibration, in correspondence with Eq. (45). The score for the climatological forecast was included in the legend ( $CRPS_{Climate} = 0.117 \text{ } ^\circ\text{C}$ )

1709  $RMSE_{CanSIPS}^{Calibrated}(k)/\sqrt{\pi}$  is shown in dashed black line with  
 1710 triangles. There is perfect agreement between these opti-  
 1711 mal values and the CRPS of CanSIPS after the calibration,  
 1712 in correspondence with Eq. (45). The score for the clima-  
 1713 tological forecast was included in the legend for reference  
 1714 ( $CRPS_{Climate} = 0.117 \text{ } ^\circ\text{C}$ ).

1715 If we compare Fig. 21 with Fig. 17d, we can see that  
 1716 the effect of the calibration of the CanSIPS output is more  
 1717 noticeable for the CRPS than for the RMSE. The probab-  
 1718 ilistic forecast gains from both the inflation of the standard  
 1719 deviation and the scaling of the ensemble mean, while  
 1720 only the latter influences the deterministic forecast. After  
 1721 the adjustment, CanSIPS forecast is better for zero months  
 1722 lead time, but for the rest of the forecast horizons StocSIPS  
 1723 shows more skill. The relative advantage of the stochastic  
 1724 model over the GCM increases the further we forecast into  
 1725 the future. For the first month, the numerical model forecast  
 1726 still falls in the deterministic predictability limit.

## 4 Discussion

1727  
 1728 Over the last decades, conventional numerical approaches  
 1729 have developed to the point where they are now skillful at  
 1730 lead times that approach their theoretical (deterministic)  
 1731 predictability limits—itsself close to the lifetimes of plan-  
 1732 etary structures (about 10 days). This threshold is due to the

1733 nonlinearity and complexity of the equations of atmospheric  
 1734 dynamics and their sensitive dependence on initial condi-  
 1735 tions (butterfly effect) (Lorenz 1963, 1972), and it cannot  
 1736 be overcome using purely deterministic models, not even by  
 1737 using combinations of deterministic-stochastic approaches  
 1738 such as recent stochastic parameterization models (Berner  
 1739 et al. 2017). In the macroweather regime (from 10 days to  
 1740 decades), GCMs become stochastic: the model integrations  
 1741 are extended far beyond their predictability limits produc-  
 1742 ing “random” outputs that are finally averaged to obtain the  
 1743 forecast as the model ensemble mean.

1744 The convergence of the dynamical models to their own  
 1745 climate follows from the macroweather property of internal  
 1746 fluctuations to decrease with time scale (see Fig. 6 for the  
 1747 case of natural variability—including volcanic and solar  
 1748 forcings). This scaling behavior with negative fluctuation  
 1749 exponent is present in real data and in GCM control runs, so  
 1750 the statistics of conventional numerical models’ variability  
 1751 is of similar type to that found in the real-world temperature  
 1752 series. The main problem is that each GCM converges to  
 1753 its own model climate, which is different from the actual  
 1754 climate. Also, the models cannot fully reproduce the actual  
 1755 high frequency weather noise even if the statistics of the  
 1756 noise they generate is similar to the real-world one.

1757 In that sense, the SLIMM model, developed in Lovejoy  
 1758 et al. (2015), uses real data to generate the high-frequency  
 1759 noise with the correct statistical symmetries for the fluctua-  
 1760 tions and with a realistic climate. The main characteristics  
 1761 of SLIMM were summarized in Sect. 2.1. In this paper we  
 1762 presented the Stochastic Seasonal to Interannual Prediction  
 1763 System (StocSIPS), which includes SLIMM as the core  
 1764 model to forecast the natural variability component of the  
 1765 temperature field. StocSIPS also represents a more general  
 1766 framework for modelling the seasonality and the anthropo-  
 1767 genic trend and the possible inclusion of other atmospheric  
 1768 fields at different temporal and spatial resolutions. In this  
 1769 sense, StocSIPS is the general system and SLIMM is the  
 1770 main part of it dedicated to the modelling of the stationary  
 1771 scaling series.

1772 StocSIPS is based on some statistical properties of the  
 1773 macroweather regime such as: the Gaussianity of tempera-  
 1774 ture fluctuations (as justified in Appendix 2) and the tempo-  
 1775 ral scaling symmetry of the natural variability with negative  
 1776 fluctuation exponents, as shown in Sect. 3.2. It also assumes  
 1777 the independence between the high frequency natural vari-  
 1778 ability of the temperature field and the low frequency com-  
 1779 ponent dominated by anthropogenic effects. The anthropo-  
 1780 genic component is represented as a short memory linear  
 1781 response to equivalent CO<sub>2</sub> forcing. The natural variability  
 1782 component is modeled and predicted using the stochastic  
 1783 approach originally proposed in SLIMM.

1784 The scaling of the fluctuations implies that there are  
 1785 power-law decorrelations in the system and hence a large

1786 memory effect that can be exploited. The simplest stochastic  
 1787 model that includes both the Gaussianity and the scaling of  
 1788 the fluctuations is the fGn process. The Gaussian statistics  
 1789 of the temperature natural variability fluctuations allowed  
 1790 us to use the mean square prediction framework to build an  
 1791 optimal conditional expectation predictor based on a linear  
 1792 combination of past data.

1793 In Sects. 2 and 2.1 we discuss how fGn can be obtained  
 1794 in SLIMM as the solution of a fractional order differential  
 1795 equation, which in turn is a generalization of the integer  
 1796 order stochastic differential equation in LIM models. The  
 1797 fractional derivative is introduced to account for the large  
 1798 memory effect given by the power-law behavior of the cor-  
 1799 relation function, in contrast, integer order derivatives imply  
 1800 short memory autoregressive moving average processes with  
 1801 asymptotic exponential decorrelations. The fractional dif-  
 1802 ferential equation can be obtained as the high frequency  
 1803 limit of a fractional energy balance equation in which the  
 1804 usual (exponential) temperature relaxation to equilibrium  
 1805 is replaced by power-law relaxation (work in progress). The  
 1806 main characteristics of SLIMM are summarized in Sect. 2.1,  
 1807 including the formal expression for the predictor as an inte-  
 1808 gral of innovations going an infinite time into the past.  
 1809 Physically, the source of the long-range memory is energy  
 1810 stored in ocean gyres, eddies, at depth, or over land, in ice,  
 1811 soil moisture, etc.

1812 The original technique that was used to make the SLIMM  
 1813 forecasts was basically correct, but it made several approxi-  
 1814 mations (such as that the amount of data available for the  
 1815 forecast was infinite) and it was numerically cumbersome.  
 1816 Most of this work was dedicated to improving the math-  
 1817 ematical treatment and the numerical techniques of SLIMM  
 1818 and validate them on ten different global temperature series  
 1819 since 1880 (five globally averaged and five over land).

1820 The main improvement included in StocSIPS for the pre-  
 1821 diction of temperature series is the application of discrete-  
 1822 in-time fGn to obtain an optimal predictor based on a finite  
 1823 amount of past data. In Sect. 2.2.1 we give the theoretic-  
 1824 al expressions for the predictor coefficients and the skill  
 1825 as functions of the fluctuation exponent alone. This repre-  
 1826 sents an advantage over other autoregressive models (AR,  
 1827 ARMA) which do not include fractional integrations that  
 1828 account for the long-term memory and hence do not consider  
 1829 the information from the distant past. An additional limita-  
 1830 tion of these approaches is that, in order to predict, the auto-  
 1831 correlation function for each time lag,  $C(\Delta t)$ , must be esti-  
 1832 mated directly from the data. Each  $C(\Delta t)$  will have its own  
 1833 sampling error, this effectively introduces a large “noise”  
 1834 in the predictor estimates and a large computational cost if  
 1835 many coefficients are needed. In our fGn model the coef-  
 1836 ficients have an analytic expression which only depends on  
 1837 the fluctuation exponent,  $H$ , obtained directly from the data  
 1838 exploiting the scale-invariance symmetry of the fluctuations;



our problem is a statistically highly constrained problem of parametric estimation ( $H$ ), not an unconstrained one (the entire  $C(\Delta t)$  function).

Other technical details of discrete-in-time fGn models are given in Appendix 1. We discuss how to produce exact realizations of fGn processes with a given length,  $N$  and family of parameters  $\sigma$ ,  $\mu$  and  $H$ . The inverse process of obtaining those parameters for a given time series is also discussed. Other important results shown in Appendix 1 are an algorithm called quasi maximum likelihood estimation (QMLE) for obtaining the parameter  $H$ , and the derivation of some ergodic properties of fGn processes. The QMLE method is slightly less accurate—but much more efficient computationally—than the usual maximum likelihood method. It has the advantage of being part of the verification process as it minimizes the mean square error of the hindcasts. The ergodicity of the variance of the process, expressed in Eq. (62), besides proving the convergence of the temporal average estimate of the variance to the ensemble variance, also shows that this convergence is ultra slow for values of  $H$  close to zero. This fact implies a strong dependence of the value of the resulting skill score with the length of the hindcast series used for verification. It could potentially impact statistical methods that depend on the covariance matrix, e.g. empirical orthogonal functions (EOF) and empirical mode decomposition (EMD).

The main result of this work is the application of StocSIPS to the modeling and forecasting of global temperature series. With that purpose, we selected the five major observation-based global temperature data series which are in common use (see Sect. 3.1).

Over the last century, low frequencies are dominated by anthropogenic effects and after 10–20 years the scaling regime changes from a negative to a positive value of  $H$  (see Fig. 6). The anthropogenic component was modelled as a linear response to equivalent  $\text{CO}_2$  forcing and removed. The residual natural variability component was then modeled and predicted using the theory presented in Sect. 2 and Appendix 1. The quality of the fit of the fGn model to the real data was evaluated in detail in Appendix 2.

To validate our model, we produced series of hindcasts for the period 1931–2017 with forecast horizons from 1 to 12 months. These series were stratified to obtain the dependence of the forecast skill with the forecast horizon and the initialization time. The RMSE of the hindcasts was lower than the standard deviation of the verification series for all horizons, showing positive skill. The values obtained for the all-month average results were in good agreement with the theoretical predictions. Other skill scores, such as the MSSS and the ACC were obtained.

StocSIPS source of predictability is based on the strong long-range correlations present in the temperature time series. In that sense, there is no source of skill coming from interannual variations since the model assumes that the

seasonality, as well as the low frequency trend in the raw data, are deterministic. Theoretically, we should not expect a dependence of the skill on the initialization time. However, the stratification of the data shows that there is a multiplicative seasonality effect that makes the variability different for each individual month (see Fig. 11). The standard deviation of the temperature for the Boreal winter months is considerably larger than for the rest. This affects the skill of StocSIPS for those months and is a discrepancy with respect to the stationarity hypothesis. In future work, we could compensate for this effect through preprocessing of the time series and study the implications in StocSIPS forecast skill.

In Sect. 3.4.4 we showed how to make parametric probability forecasts using StocSIPS. For a prediction system with Gaussian errors, we derived a theoretical relation between the deterministic score RMSE and the probabilistic CRPS. We also showed that StocSIPS is—by definition—a nearly perfectly reliable system and that this theoretical relation is satisfied by the verification results.

Finally, in Sect. 3.5 we compared StocSIPS with the Canadian Seasonal to Interannual Prediction System (CanSIPS), which is one of the GCMs contributing to the Long-Range Forecast project of the World Meteorological Organization. Deterministic and probabilistic forecast skill scores for StocSIPS and for the CanSIPS were compared for the verification period 1981–2010.

The main conclusion is that, for the overall forecast including all the months in the verification period and without considering different initialization times, StocSIPS has higher skill than CanSIPS for all the metrics used and for all horizons except for  $k = 1$  month, where CanSIPS is slightly better. This was not surprising since for GCMs, 1 month is still close to the deterministic predictability threshold imposed by the chaotic behavior of the system ( $\sim 10$  days for the atmosphere and 1–2 years for the ocean). Beyond 1 month, the relative advantage of StocSIPS increases as the horizon increases. The seasonal stratification of the verification shows that, due to the interannual variability, CanSIPS performs better than StocSIPS for the forecasts of January and February. For other months (beyond zero months lead times) StocSIPS has better skill.

## 5 Conclusions

In this paper we presented the Stochastic Seasonal to Interannual Prediction System (StocSIPS), which is based on some statistical properties of the macroweather regime such as: the Gaussianity of temperature fluctuations and the temporal scaling symmetry of the natural variability. StocSIPS includes SLIMM as the core model to forecast the natural variability component of the temperature field. Here we

improved the theory and numerical methods of SLIMM for its direct application to macroweather forecast.

In summary, StocSIPS models the temperature series as a superposition of a periodic signal corresponding to the annual cycle, a low frequency deterministic trend from anthropogenic forcings and a high frequency stochastic natural variability component. The annual cycle can be estimated directly from the data and is assumed constant in the future, at least for horizons of a few years. The anthropogenic component is represented as a linear response to equivalent CO<sub>2</sub> forcing and can be projected very accurately 1 year into the future by using two parameters, the climate sensitivity and an offset, which can be obtained from linear regression given historical emissions. Finally, the natural variability is modeled as a discrete-in-time fGn process which is completely determined by the variance and the fluctuation exponent. That gives a total of only four parameters for modeling and predicting the temperature series. Those parameters are quite stable and can be estimated with good accuracy from past data.

The comparison with CanSIPS validates StocSIPS as a good alternative and a complementary approach to conventional numerical models. The reason is that whereas CanSIPS and StocSIPS have the same type of statistical variability around the climate state, the CanSIPS model climate is different from the real-world climate. In comparison, StocSIPS uses historical data to force the forecast to the real-world climate. From a forecast point of view, in general, GCMs can be seen as an initial value problem for generating many “stochastic” realizations of the state of the atmosphere, while StocSIPS is effectively a past value problem that directly estimates the most probable future state.

The prediction of global average temperature series presented in this paper is based on some symmetries of the macroweather regime: scale-invariance and low intermittency (rough Gaussianity). In a future paper (currently in preparation), we show how another macroweather symmetry, the statistical space time factorization (Lovejoy and de Lima 2015), can be included to extend the application of StocSIPS to temperature forecasts at a regional level with any arbitrary spatial resolution without need for downscaling. Another future application of StocSIPS that can be derived from this work is that, due to its qualitatively different approach with respect to traditional GCMs, it is possible to combine CanSIPS and StocSIPS into a single hybrid forecasting system that improves on both, especially at zero lead times. We have already obtained some predictions with the combined model, “CanStoc”, and we are currently working on a future publication on these results. We are also working on the application of StocSIPS to the forecast of GCMs preindustrial control runs to show that they satisfy the same macroweather symmetries as real-world data and hence, together with their deterministic predictability limits, there are also stochastic predictability limits applicable to GCMs. These

limits correspond to the maximum possible skill that can be achieved by a stochastic Gaussian scaling system with a given scaling exponent (measure of the memory and the predictability in the data).

In May 2016, we created the website: <http://www.physic.cs.mcgill.ca/StocSIPS/>, where global average and regional temperature forecasts at monthly, seasonal and annual resolutions using StocSIPS are published on a regular basis.

## Appendix 1: Simulation, parameters estimation, ergodicity and model adequacy

### Simulation

When modeling real time series and testing numerical algorithms, it is often useful to obtain synthetic realizations of fGn processes. There are many methods for simulating approximate samples of fGn, e.g.: (1) type 1 (Mandelbrot and Wallis 1969), (2) type 2 (Mandelbrot and Wallis 1969), (3) fast fGn (Mandelbrot 1971), (4) filtered fGn (Matalas and Wallis 1971), (5) ARMA(1,1) (O’Connell 1974), (6) broken line (Garcia et al. 1972; Mejia et al. 1972; Rodriguez-Iturbe et al. 1972; Mandelbrot 1972), (7) ARMA-Markov models (Lettenmaier and Burges 1977) and some approximate, more efficient, recent methods (Paxson 1997; Jeong et al. 2003). We can choose among these methods based on their strengths and weaknesses, depending on the specific application we need.

Nevertheless, instead of using short memory approximations for simulating fGn, it is possible to generate exact realizations by applying the following procedure (Hipel and McLeod 1994; Palma 2007). In Eq. (20) we gave the MA representation of our series for any time,  $t$ , based on the knowledge of an infinite past of innovations,  $\{\gamma_{t-j}\}_{j=1,\dots,\infty}$  with  $\gamma_t \sim \text{NID}(0, 1)$  and  $\langle \gamma_i \gamma_j \rangle = \delta_{ij}$ . If we want a series with specific length,  $N$ , mean  $\mu$ , variance  $\sigma_T^2$  and fluctuation exponent  $H$ , we can work in a similar way as we did with the AR representation for obtaining the predictor. By replacing the coefficients,  $\varphi_j$ , we could write instead the finite sum:

$$T_t = \mu + \sum_{j=1}^t m_{ij} \gamma_{t+1-j} = \mu + m_{t1} \gamma_t + \dots + m_{tt} \gamma_1, \quad (46)$$

for  $t = 1, \dots, N$ , where the optimal coefficients  $m_{ij}$  are the elements of the lower triangular matrix  $\mathbf{M}_{H,\sigma_T}^N$  given by the Cholesky decomposition of the autocovariance matrix,  $\mathbf{R}_{H,\sigma_T}^N = [C_{H,\sigma_T}(i-j)]_{i,j=1,\dots,N}$ ; that is:

$$\mathbf{R}_{H,\sigma_T}^N = \mathbf{M}_{H,\sigma_T}^N \left( \mathbf{M}_{H,\sigma_T}^N \right)^T, \quad (47)$$

with  $m_{ij} = 0$  for  $j > i$ . In summary, for obtaining an fGn realization of length  $N$ , we need to generate a white-noise process  $\{\gamma_t\}_{t=1,\dots,N}$  with an appropriate method, obtain the autocovariance matrix  $\mathbf{R}_{H,\sigma_T}^N$  using Eq. (7.iii), then get  $\mathbf{M}_{H,\sigma_T}^N$  from the Cholesky decomposition of  $\mathbf{R}_{H,\sigma_T}^N$ , and finally apply Eq. (46) for every  $t$  to obtain our  $\{T_t\}$  series. The variables  $T_t$  will be NID( $\mu, \sigma_T^2$ ) and the process will have fluctuation exponent  $H$  in the interval  $(-1, 0)$ .

### Maximum likelihood estimation

If instead of simulating an fGn process, we are interested in the opposite operation of finding the parameters that best fit a given time series, the most accurate method to use is based on maximizing the log-likelihood function (Hipel and McLeod 1994). Suppose that we have our vector  $\mathbf{T}_N = [T_1, \dots, T_N]^T$  that represents a stationary Gaussian process. Then the log-likelihood function of this process is given by:

$$\mathfrak{L}(\mu, \sigma_T, H) = -\frac{1}{2} \log [\det(\mathbf{R}_{H,\sigma_T}^N)] - \frac{1}{2} \tilde{\mathbf{T}}_{N,\mu}^T (\mathbf{R}_{H,\sigma_T}^N)^{-1} \tilde{\mathbf{T}}_{N,\mu} \quad (48)$$

where  $\tilde{\mathbf{T}}_{N,\mu} = [T_1 - \mu, \dots, T_N - \mu]^T$  is a vector formed by our original series after removing the mean.

For fixed  $H$ , the maximum likelihood estimators (MLE) of  $\mu$  and  $\sigma_T$  are:

$$\hat{\mu} = \frac{\mathbf{1}_N^T (\tilde{\mathbf{R}}_H^N)^{-1} \mathbf{T}_N}{\mathbf{1}_N^T (\tilde{\mathbf{R}}_H^N)^{-1} \mathbf{1}_N} \quad (49)$$

and

$$\hat{\sigma}_T^2 = \frac{1}{N} \tilde{\mathbf{T}}_{N,\hat{\mu}}^T (\tilde{\mathbf{R}}_H^N)^{-1} \tilde{\mathbf{T}}_{N,\hat{\mu}}, \quad (50)$$

where  $\mathbf{1}_N = [1, 1, \dots, 1]^T$  is an  $N \times 1$  vector with all the elements equal to 1 and  $\tilde{\mathbf{R}}_H^N = \mathbf{R}_{H,\sigma_T}^N / \sigma_T^2$  is the autocorrelation matrix, which only depends on  $H$ .

Substituting these values into Eq. (48), we obtain the maximized log-likelihood function of  $H$ :

$$\mathfrak{L}_{\max}(H) = -\frac{1}{2} \log [\det(\tilde{\mathbf{R}}_H^N)] - \frac{N}{2} \log \left[ \frac{1}{N} \tilde{\mathbf{T}}_{N,\hat{\mu}}^T (\tilde{\mathbf{R}}_H^N)^{-1} \tilde{\mathbf{T}}_{N,\hat{\mu}} \right]. \quad (51)$$

The estimate for the fluctuation exponent,  $\hat{H}_l$ , is obtained by maximizing  $\mathfrak{L}_{\max}(H)$  and can be used then to obtain  $\hat{\mu}$  and  $\hat{\sigma}_T^2$  using Eqs. (49) and (50).

### Ergodicity

It is worth noticing here that  $\hat{\mu}$  and  $\hat{\sigma}_T^2$  are estimates of the ensemble mean  $\mu = \langle T_t \rangle$  and variance  $\sigma_T^2 = \langle (T_t - \mu)^2 \rangle$  of the fGn process, respectively (see Sect. 2.1). If we try to

estimate these parameters based on temporal averages of a single realization, some differences may arise with the values obtained using Eqs. (49) and (50). To explain these differences, we briefly discuss some ergodic properties of fGn processes.

Let

$$\bar{T}_N = \frac{\sum_{t=1}^N T_t}{N} \quad (52)$$

and

$$SD_T^2 = \frac{\sum_{t=1}^N (T_t - \bar{T}_N)^2}{N} = \overline{(T_N - \mu)^2} - (\bar{T}_N - \mu)^2 \quad (53)$$

be the temporal average estimates of the mean and the variance of our process, respectively (the overbar indicates temporal averaging,  $N$  is considered large here), SD indicates "standard deviation".

Using the relationship between fBm and fGn (Eq. (5)), we can write the temperature as:

$$T_t = \sigma_T [B_{H'}(t) - B_{H'}(t-1)]. \quad (54)$$

The fBm process has the following properties:

(i)  $B_{H'}(t)$  is Gaussian with stationary increments;

(ii)  $\langle B_{H'}(t) \rangle = \mu t / \sigma_T$  for all  $t$

(the notation  $\langle \cdot \rangle$  denotes ensemble averaging)

(iii)  $C_{B_{H'}}(t, s) = \langle [B_{H'}(t) - \mu t / \sigma_T] [B_{H'}(s) - \mu s / \sigma_T] \rangle = (|t|^{2H'} + |s|^{2H'} - |t-s|^{2H'}) / 2$

Usually, the condition  $B_{H'}(0) = 0$  is added to this definition. Using this and Eq. (54), by telescopic sum all addends cancel except for the last one and we obtain:

$$\bar{T}_N = \frac{1}{N} \sigma_T B_{H'}(N). \quad (56)$$

Taking ensemble averages and using Eqs. (55) (ii) and (iii) we get:

$$\langle \bar{T}_N \rangle = \mu \quad (57)$$

and

$$\langle (\bar{T}_N - \mu)^2 \rangle = \frac{1}{N^2} \sigma_T^2 \langle [B_{H'}(N) - \mu N / \sigma_T]^2 \rangle = \sigma_T^2 N^{2H}, \quad (58)$$

where we replaced  $H' = H + 1$ .

**Table 4** Average estimates of  $H$  for 200 realizations of simulated fGn with length  $N = 1656$  and parameters  $\mu = 0, \sigma_T = 1$  and  $H$  corresponding to the values in the first column

| $H$   | $\hat{H}_q$  | $\hat{H}_l$  | $\hat{H}_{l,ens}$ | $\hat{H}_h$  | $\hat{H}_{h,ens}$ | $\hat{H}_s$  | $\hat{H}_{s,ens}$ | $\hat{\sigma}_T$ | $SD_T$ | $\frac{SD_T}{\sqrt{1-N^{2H}}}$ |
|-------|--------------|--------------|-------------------|--------------|-------------------|--------------|-------------------|------------------|--------|--------------------------------|
| -0.45 | -0.45 (0.02) | -0.45 (0.02) | -0.45             | -0.48 (0.07) | -0.45             | -0.51 (0.06) | -0.44             | 1.00             | 1.00   | 1.00                           |
| -0.40 | -0.40 (0.01) | -0.40 (0.01) | -0.40             | -0.42 (0.07) | -0.40             | -0.45 (0.05) | -0.39             | 1.00             | 1.00   | 1.00                           |
| -0.35 | -0.35 (0.02) | -0.35 (0.02) | -0.35             | -0.37 (0.07) | -0.35             | -0.40 (0.06) | -0.33             | 1.00             | 1.00   | 1.00                           |
| -0.30 | -0.30 (0.02) | -0.30 (0.02) | -0.30             | -0.34 (0.08) | -0.30             | -0.35 (0.06) | -0.28             | 1.00             | 0.99   | 1.00                           |
| -0.25 | -0.26 (0.02) | -0.25 (0.02) | -0.25             | -0.28 (0.08) | -0.25             | -0.29 (0.05) | -0.24             | 1.00             | 0.99   | 1.00                           |
| -0.20 | -0.21 (0.02) | -0.20 (0.02) | -0.20             | -0.24 (0.08) | -0.20             | -0.24 (0.06) | -0.18             | 1.00             | 0.97   | 1.00                           |
| -0.15 | -0.17 (0.02) | -0.15 (0.02) | -0.15             | -0.18 (0.09) | -0.15             | -0.19 (0.06) | -0.12             | 0.99             | 0.94   | 1.00                           |
| -0.10 | -0.12 (0.02) | -0.10 (0.02) | -0.10             | -0.12 (0.07) | -0.10             | -0.13 (0.05) | -0.07             | 1.00             | 0.88   | 1.00                           |
| -0.05 | -0.08 (0.01) | -0.06 (0.02) | -0.05             | -0.08 (0.08) | -0.05             | -0.09 (0.06) | -0.02             | 0.98             | 0.71   | 0.99                           |

The values in parentheses represent the standard deviation for each ensemble. The following methods were used: QMLE ( $\hat{H}_q$ ), MLE ( $\hat{H}_l$ ), Haar fluctuations ( $\hat{H}_h$ ) and spectral analysis ( $\hat{H}_s$ ). For these last three methods, direct ensemble estimates were also obtained ( $\hat{H}_{-,ens}$ );  $\hat{H}_-$  could be seen as the mean of all the  $\hat{H}_-$ 's while  $\hat{H}_{-,ens}$  is the  $\hat{H}_-$  of the mean. The last three columns show the average estimates  $\hat{\sigma}_T, SD_T$  and the confirmation of their relationship given by Eq. (62)

**Table 5** Values of the parameters obtained for the ten datasets and the corresponding mean series for global and for land

| Dataset | $\hat{H}_l$ | $\hat{H}_q$ | $\hat{H}_h$  | $\hat{H}_s$  | $\hat{\sigma}_T$ | $SD_T$ | $\frac{SD_T}{\sqrt{1-N^{2H}}}$ | $\lambda_{2 \times CO_2,eq}$ | $T_0$          |
|---------|-------------|-------------|--------------|--------------|------------------|--------|--------------------------------|------------------------------|----------------|
| NASA    | -0.08       | -0.10       | -0.11 (0.02) | -0.08 (0.04) | 0.183            | 0.155  | 0.184                          | 2.10 (0.03)                  | -0.391 (0.006) |
| NOAA    | -0.06       | -0.09       | -0.06 (0.02) | -0.03 (0.04) | 0.183            | 0.144  | 0.187                          | 2.00 (0.02)                  | -0.372 (0.006) |
| HAD4    | -0.07       | -0.08       | -0.06 (0.02) | -0.10 (0.06) | 0.194            | 0.159  | 0.201                          | 1.89 (0.03)                  | -0.353 (0.006) |
| CowW    | -0.09       | -0.10       | -0.09 (0.03) | -0.10 (0.05) | 0.183            | 0.163  | 0.193                          | 1.98 (0.03)                  | -0.369 (0.006) |
| Berk    | -0.08       | -0.09       | -0.07 (0.02) | -0.12 (0.07) | 0.197            | 0.174  | 0.209                          | 2.20 (0.03)                  | -0.410 (0.007) |
| Mean-G  | -0.06       | -0.08       | -0.08 (0.02) | -0.10 (0.06) | 0.195            | 0.153  | 0.199                          | 2.03 (0.03)                  | -0.379 (0.006) |
| NASA-L  | -0.25       | -0.24       | -0.21 (0.02) | -0.29 (0.04) | 0.373            | 0.371  | 0.376                          | 2.96 (0.06)                  | -0.551 (0.015) |
| NOAA-L  | -0.25       | -0.25       | -0.24 (0.02) | -0.27 (0.03) | 0.331            | 0.325  | 0.329                          | 2.95 (0.05)                  | -0.550 (0.013) |
| HAD4-L  | -0.18       | -0.19       | -0.19 (0.02) | -0.24 (0.04) | 0.297            | 0.285  | 0.295                          | 2.70 (0.05)                  | -0.503 (0.011) |
| CowW-L  | -0.22       | -0.22       | -0.18 (0.03) | -0.27 (0.04) | 0.337            | 0.333  | 0.339                          | 2.84 (0.06)                  | -0.529 (0.013) |
| Berk-L  | -0.23       | -0.23       | -0.21 (0.02) | -0.25 (0.03) | 0.348            | 0.342  | 0.349                          | 2.81 (0.06)                  | -0.523 (0.014) |
| Mean-L  | -0.22       | -0.22       | -0.20 (0.02) | -0.26 (0.04) | 0.327            | 0.321  | 0.327                          | 2.85 (0.05)                  | -0.531 (0.013) |

From left to right we have estimates of  $H$  using the following methods: MLE ( $\hat{H}_l$ ), QMLE ( $\hat{H}_q$ ), Haar fluctuations ( $\hat{H}_h$ ) and spectral analysis ( $\hat{H}_s$ ); estimate of the standard deviation of the ensemble using MLE ( $\hat{\sigma}_T$ ); amplitude of each series ignoring the correlations ( $SD_T$ ); confirmation of the relationship between  $\hat{\sigma}_T$  and  $SD_T$  given by Eq. (25); the climate sensitivity and offset used to remove the anthropogenic trend,  $\lambda_{2 \times CO_2,eq}$  and  $T_0$ , respectively (Eq. (27)). Uncertainty estimates are given in parentheses

2102 Consequently, since the process  $B_{H^r}(t)$  is Gaussian, we  
 2103 conclude that, the temporal average estimate of the mean  
 2104 satisfies:

$$\bar{T}_N \sim N(\mu, \sigma_T^2 N^{2H}). \tag{59}$$

2106 Now, taking the ensemble average of Eq. (53), we get:

$$\langle SD_T^2 \rangle = \left\langle \overline{(T_N - \mu)^2} \right\rangle - \left\langle (\bar{T}_N - \mu)^2 \right\rangle. \tag{60}$$

2108 The ensemble and the time averaging operations com-  
 2109 mute in the first term of the right-hand side of Eq. (60):

$$\left\langle \overline{(T_N - \mu)^2} \right\rangle = \overline{\langle (T_N - \mu)^2 \rangle} = \sigma_T^2. \tag{61}$$

Using this and Eq. (58) for the last term in Eq. (60), we  
 finally get:

$$SD_T^2 = \sigma_T^2 (1 - N^{2H}), \tag{62}$$

2114 meaning that the temporal average  $SD_T$  is a biased estimate  
 2115 of the variance of the process,  $\sigma_T^2$ . An unbiased estimate  
 2116 would then be  $SD_T^2 / (1 - N^{2H})$ . The variance of this estima-  
 2117 tor is more difficult to obtain. Its derivation, together with  
 2118 potential applications for treating climate series, will be pre-  
 2119 sented in a future paper (currently in preparation).

2120 In the limit  $N \rightarrow \infty$ , as  $-1 < H < 0$ , we have  $SD_T^2 \rightarrow \sigma_T^2$ ,  
 2121 meaning that the process is ergodic (the temporal average  
 2122 and the ensemble average coincide for infinitely long series).  
 2123 Nevertheless, for  $H \rightarrow 0$  this convergence is very slow, and



2124 a very long series would be needed in order to estimate the  
 2125 variance of the process from the sample variance without  
 2126 any correction. For example, for  $H = -0.1$  and  $N = 1656$   
 2127 months = 138 years (realistic values for globally-averaged  
 2128 temperatures, see Sect. 3), we have  
 2129  $SD_T^2/\sigma_T^2 = (1 - N^{2H}) = 0.772$ , i.e. a 23% difference between  
 2130 both estimates. In the same sense, if we want to estimate  $\sigma_T^2$   
 2131 from the sample variance with 95% accuracy, we would need  
 2132 a series with  $N = 3.2 \cdot 10^6$  (if  $N$  is in months that would be  
 2133  $N = 266,667$  years!). The last three columns of Table 4 show  
 2134 the average estimates  $\hat{\sigma}_T = \sqrt{\hat{\sigma}_T^2}$  (Eq. (50)),  $SD_T$  (Eq. (53))  
 2135 and the confirmation of their relationship (Eq. (62)), for  
 2136 simulations of fGn with length  $N = 1656$  and parameters  
 2137  $\mu = 0$ ,  $\sigma_T = 1$  and values of  $H$  in the range  $(-1/2, 0)$ . In each  
 2138 case, 200 realizations were analyzed, but only the average  
 2139 values of the estimates are shown. The standard deviations  
 2140 are always 2–7% of the respective mean values and were not  
 2141 reported. Notice that the difference between  $\hat{\sigma}_T$  and  $SD_T$   
 2142 increases as  $H$  goes close to zero and the memory effects  
 2143 become more important.

2144 Let us return now to the estimates  $\hat{\mu}$  and  $\hat{\sigma}_T^2$  given by  
 2145 Eqs. (49) and (50), respectively. These ensemble estimates  
 2146 are still obtained from the information of only one finite  
 2147 series,  $\mathbf{T}_N = [T_1, \dots, T_N]^T$ , but the presence of the correlation  
 2148 matrix,  $\hat{\mathbf{R}}_H^N$ , automatically includes all the information  
 2149 from the infinite unknown past. If we make  $\hat{\mathbf{R}}_H^N = \mathbf{I}_N$  ( $\mathbf{I}_N$  is  
 2150 the  $N \times N$  identity matrix) in Eqs. (49) and (50) (or equivalently  
 2151  $H = -1/2$ ), we obtain:

$$2152 \hat{\mu} = \frac{\mathbf{1}_N^T \mathbf{T}_N}{\mathbf{1}_N^T \mathbf{1}_N} = \frac{\sum_{t=1}^N T_t}{N} = \bar{T}_N \quad (63)$$

2153 and

$$2154 \hat{\sigma}_T^2 = \frac{1}{N} \tilde{\mathbf{T}}_{N,\hat{\mu}}^T \tilde{\mathbf{T}}_{N,\hat{\mu}} = \frac{\sum_{t=1}^N (T_t - \hat{\mu})^2}{N} = SD_T^2. \quad (64)$$

2155 This means that the temporal average estimates based on  
 2156 one realization of the process are only valid for uncorrelated  
 2157 process, for which the ensemble and the sample averages are  
 2158 equal. When both correlations and memory effects are present,  
 2159 this information must be considered. In the case of fGn  
 2160 processes, the memory effects are introduced by including  
 2161 the correlation matrix which only depends on the fluctuation  
 2162 exponent  $H$ . The value of this parameter for the process can  
 2163 also be obtained from only one realization of the same as  
 2164 shown below.

### 2165 Quasi-maximum-likelihood estimation for $H$

2166 As we mentioned before, the MLE for the fluctuation expo-  
 2167 nent,  $\hat{H}_t$ , is obtained by maximizing  $\mathcal{L}_{\max}(H)$  (Eq. (51)). The

process of optimization of  $\mathcal{L}_{\max}(H)$  could easily be compu- 2168  
 2169 tationally expensive for large values of  $N$ . To avoid this,  
 2170 many approximate methods have been developed. We can  
 2171 use Eq. (9) to obtain  $\hat{H}_s = (\beta_l - 1)/2$  from the spectral expo-  
 2172 nent at low frequencies. This method, as well as the Haar  
 2173 wavelet analysis to obtain an estimate  $\hat{H}_h$  from the exponent  
 2174 of the Haar fluctuations, was used in Lovejoy and Schertzer  
 2175 (2013) and Lovejoy et al. (2015) to obtain estimates of  $H$  for  
 2176 average global and Northern Hemisphere anomalies. These  
 2177 two methods depend on the range selected for the linear  
 2178 regression and, when the graphs are noisy, it could result in  
 2179 poor estimates of the exponents. They, nevertheless, have  
 2180 the advantage of being more general; they yield  $H$  estimates  
 2181 even for highly nonGaussian processes. In the present case,  
 2182 a more accurate approximation is based on quasi-maximum-  
 2183 likelihood estimates (QMLE) from autoregressive approxi-  
 2184 mations (Palma 2007).

Suppose we have a series of  $N$  observations,  $\{T_t\}_{t=1,\dots,N}$ ,  
 2185 we can build the one-step predictor for  $T_t$ ,  $\hat{T}_t^p(1)$  from  
 2186 Eq. (22) using a memory of  $p$  steps in the past with  
 2187  $p + 1 < t \leq N$ :  
 2188

$$2189 \hat{T}_t^p(1) = \sum_{j=-p}^0 \phi_{p,j}(k) T_{t+j-1} = \phi_{p,-p}(k) T_{t-p-1} + \dots + \phi_{p,0}(k) T_{t-1}. \quad (65)$$

Then, the approximate QMLE,  $\hat{H}_q$ , is obtained by mini- 2190  
 2191 mizing the function

$$2192 \mathfrak{L}_1(H) = \sum_{t=p+2}^N [T_t - \hat{T}_t^p(1)]^2 \quad (66)$$

$$= \sum_{t=p+2}^N [T_t - \phi_{p,-p}(1) T_{t-p-1} - \dots - \phi_{p,0}(1) T_{t-1}]^2.$$

Remember that the coefficients  $\phi_{p,j}$  only depend on  $H$ . An 2193  
 2194 added advantage of this method is that, by construction, it is  
 2195 done as part of the verification process based on hindcasts.  
 2196 The actual mean square error (MSE) of our one-step predic-  
 2197 tor with memory  $p$  is  $\mathcal{L}_1(H)/(N - p - 1)$ , so in practice, we  
 2198 perform the one-step hindcasts for different values of  $H$  in  
 2199 the specified range and select the value that gives the mini-  
 2200 mum MSE. The computation of the coefficients  $\phi_{p,j}$  is fast,  
 2201 since we do not need to take very large values of  $p$  to achieve  
 2202 nearly the asymptotic skill, as we showed in Sect. 2.2.1.

In order to compare these different estimation meth- 2203  
 2204 ods, we performed some numerical experiments. By using  
 2205 Eq. (46) for the exact method with parameters  $\mu = 0$  and  
 2206  $\sigma_T = 1$ , we generated fGn ensembles of one hundred mem-  
 2207 bers of length  $N = 1656$  (see Sect. 3) for each value of  
 2208  $H \in \{-0.45, -0.40, -0.35, -0.30, -0.25, -0.20, -0.15, -0.10, -0.05\}$ .  
 2209 Then, we estimated  $H$  from the four previously mentioned  
 2210 methods for each realization. The results are summarized in  
 2211 Table 4. The values in parentheses represent the standard

deviations for each ensemble. The maximum likelihood, the Haar fluctuation and the spectral methods allow for direct estimates of the ensemble values (shown with the subscript “ens” in Table 4) by considering the maximum likelihood of the vector process, the ensemble of all the fluctuations or the average of all the spectra, respectively from all the paths instead of from each of the series independently. We could say, for example that  $\hat{H}_s$  is the mean of all the  $\hat{H}_s$ 's obtained from each realization spectrum, while  $\hat{H}_{s,\text{ens}}$  is the value obtained from the mean of all the spectra. This ensemble estimate reduces the error due to dispersion of each of the ensemble members. For the QMLE, a memory  $p = 20$  was used.

As we can see from Table 4, for the MLE method, there is good agreement between the average of the estimates for each realization and the direct ensemble estimate. This is not the case for the less accurate methods of Haar fluctuation and spectral analysis in the member-by-member cases. Comparatively, the standard deviation of these two methods (without considering the estimation error for each specific realization) is much larger than for the MLE. Nevertheless, the ensemble estimates for the Haar are very accurate because the dispersion for the ensemble is much lower than for each individual graph. In practice, it is almost always the case that we only have a given time series to analyze instead of multiple realizations of an ensemble. In that sense, unless we have more theoretical or empirical justifications for the scaling, estimates based on these graphical methods should be considered cautiously.

A direct comparison of the second and third columns in Table 4 shows the accuracy of the QMLE method if we take the MLE as reference. The average values and the standard deviations for the two methods are very close for small values of  $H$ , but as we move to values close to zero there is a systematic bias in the QMLE method towards slightly smaller values than those obtained with the MLE. Nevertheless, the presence of this bias is of little consequence from the point of view of forecasting and can be reduced by increasing the memory used. As we mentioned before, the QMLE method is based on minimizing the MSE—or what is the same—maximizing the MSSS obtained from hindcasts. Near the extreme, a small variation of the value of  $H$  used to perform the forecast will produce almost no change on the MSSS obtained.

## Model adequacy

The final step after finding the parameters  $\mu$ ,  $\sigma_T^2$  and  $H$ , is to check the adequacy of the fitted model to the data. Imagine we have a time series  $\{T_t\}_{t=1,\dots,N}$ . The residuals of our fGn model are obtained from inverting Eq. (46) and calculating the vector

$$\mathbf{e}_N = \left( \mathbf{M}_{H,\sigma_T}^N \right)^{-1} \tilde{\mathbf{T}}_{N,\mu}. \quad (67)$$

If the model provides a good description of the data, the elements of the residual vector  $\mathbf{e}_N = [e_1, \dots, e_N]^T$  should be white noise, i.e. they should be NID(0, 1) with autocorrelation function  $\langle e_i e_j \rangle = \delta_{ij}$ . Many statistical tests for whiteness of  $\{e_i\}$  could be performed, the more descriptive one being based on the examination of the graph of the residual autocorrelation function (RACF). The RACF at lag  $l$  is calculated as:

$$r_l(\mathbf{e}_N) = \frac{\sum_{i=1}^{N-l} e_i e_{i+l}}{\sum_{i=1}^N e_i^2}. \quad (68)$$

Asymptotically,  $r_l(\mathbf{e}_N) \sim \text{NID}(0, 1/N)$  for any lag  $l \geq 1$  and  $r_0(\mathbf{e}_N) = 1$ . In the graph of  $r_l(\mathbf{e}_N)$  vs.  $l$ , there should not be any point significantly far outside the 95% confidence interval given by the horizontal lines  $\pm 1.96/\sqrt{N}$ , and the number of points outside this range, should represent around 5% of the total number of points. As additional tests, we could verify that the estimates of the fluctuation exponent of  $\{e_i\}$ , using the previous graphical methods, are  $\hat{H}_s \approx \hat{H}_h \approx -0.5$ , which is the value for white noise as a particular case of fGn. The less important Gaussianity assumption could also be verified by visualizing the empirical probability distribution against a normal distribution and checking for the presence of extremes.

## Appendix 2: Checking the fGn model fit to global temperature data

In Table 5 we show the values of the parameters obtained for the ten datasets and the corresponding mean series for the globe and for land:

As we can see in Table 5, there is relatively good agreement between the more robust estimates of the fluctuation exponent,  $\hat{H}_l$  and  $\hat{H}_q$  (see Appendix 1 for the notation), with the small bias of  $\hat{H}_q$  towards smaller values (we used a memory  $p = 20$  months for estimating  $\hat{H}_q$ ). The estimates  $\hat{H}_h$  and  $\hat{H}_s$ , obtained using the general methods, also roughly agree with the MLE and QMLE considering their relatively wide one-standard deviation confidence interval (given in parentheses in Table 5). Notice the difference between the parameter  $\hat{\sigma}_T$  and the amplitude of each series,  $SD_T$ . The former is an unbiased estimate of the standard deviation for the ensemble process using maximum likelihood, while the latter is a biased estimate, where the bias is because of the limited time series and autocorrelated samples (see Ergodicity in Appendix 1). We also include the values of  $SD_T/\sqrt{1 - N^{2H}}$  for confirmation of Eq. (25) ( $N = 1656$

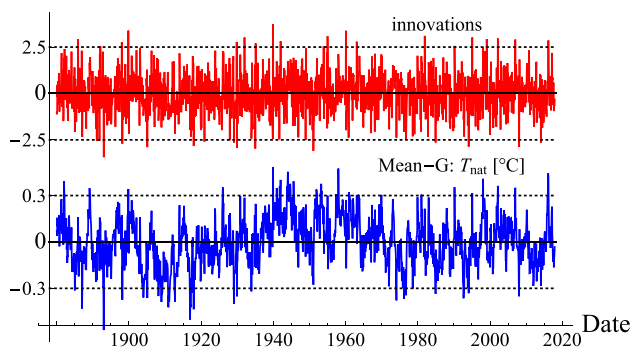


**Fig. 22** Natural variability component for the Mean-G dataset, together with its corresponding series of residual innovations,  $\{e_i\}$ , obtained using Eq. (67). The units for the  $T_{nat}$  series are  $^{\circ}\text{C}$ , while the innovations are unitless

2306 months). The last two columns show the climate sensitivity,  
 2307  $\lambda_{2\times\text{CO}_2\text{eq}}$ , and the parameter  $T_0$  (Eq. (27)) used to remove the  
 2308 anthropogenic trend in each global series. The value  $T_0$  was  
 2309 chosen to obtain  $\bar{T}_{nat} = 0$  for each dataset, but this condition  
 2310 does not imply that  $\hat{\mu} = 0$  in Eq. (49), as this last one is an  
 2311 estimate for the ensemble mean. Nevertheless, the values  
 2312 obtained for  $\hat{\mu}$  were too small compared to  $\hat{\sigma}_T$  and they were  
 2313 not included in Table 5.

2314 With the parameters shown in Table 5 for global temper-  
 2315 ature series, we can check the fit of the model to the data  
 2316 as described at the end of Appendix 1. As an example, in  
 2317 Fig. 22 we show the natural variability component for the  
 2318 Mean-G dataset, together with its corresponding series of  
 2319 residual innovations,  $\{e_i\}$ , obtained using Eq. (67). The first  
 2320 series should be Gaussian with standard deviations  $SD_T$   
 2321 while the residuals should be white noises, i.e. they should be  
 2322 NID(0, 1) with autocorrelation function  $\langle e_i e_j \rangle = \delta_{ij}$ . To verify  
 2323 the whiteness of the innovations, we should check that the  
 2324 residual autocorrelation function (RACF, (Eq. (68))) satisfies  
 2325  $r_l(\mathbf{e}_N) \sim \text{NID}(0, 1/N)$  for any lag  $l \geq 1$  (for  $l = 0, r_0(\mathbf{e}_N) = 1$ ).

2326 The graph of the RACF for the innovations of the Mean-G  
 2327 dataset is shown in Fig. 23 for  $0 \leq l \leq N/4$ , where  $N = 1656$   
 2328 is the total number of points. The inset was obtained by  
 2329 dropping the point for zero lag and zooming in the y-axis.  
 2330 The theoretical 95% confidence interval, given by the values  
 2331  $\pm 1.96/\sqrt{N}$ , is shown in dashed lines. From a direct inspec-  
 2332 tion, we can see that there are not too many points that fall  
 2333 outside the band considered and the extreme values are not  
 2334 too far from these thresholds.

2335 With the purpose of checking the Gaussianity hypoth-  
 2336 esis of the series represented in Figs. 22 and 23, a detailed  
 2337 statistical analysis was performed. Extremes in temperature  
 2338 natural variability are an important issue for the prediction  
 2339 of catastrophic events. Its presence would show as large tails  
 2340 in the distributions of temperature anomalies and their corre-  
 2341 sponding innovations. If this were the case, the model could  
 2342 be fixed by assuming white noise with a different distribution

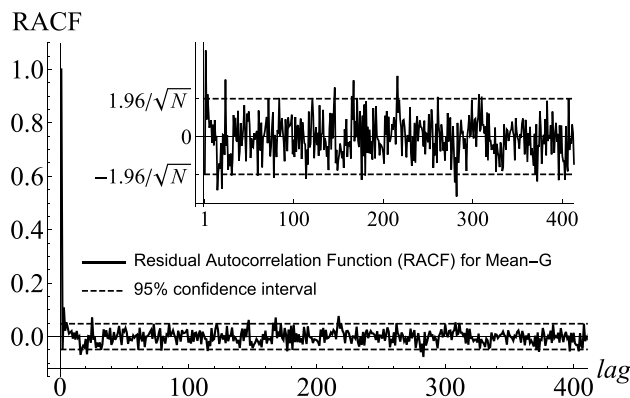


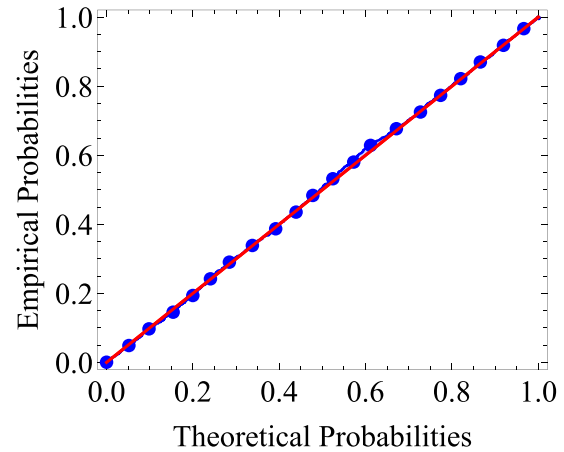
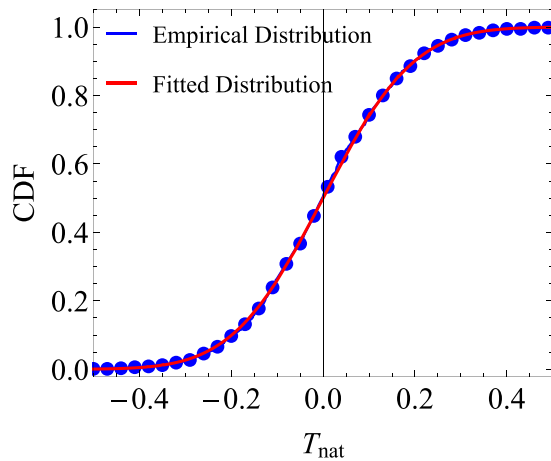
**Fig. 23** RACF for the innovations of the Mean-G dataset. The theoretical 95% confidence interval, given by the values  $\pm 1.96/\sqrt{N}$ , is shown in dashed lines ( $N = 1656$  is the total number of points)

2343 for the innovations (e.g. a Levy distribution or one from a  
 2344 multifractal process). On the other hand, deviations from  
 2345 Gaussianity in the RACF distributions would imply a differ-  
 2346 ent correlation structure and would automatically invalidate  
 2347 the applicability of the fGn model.

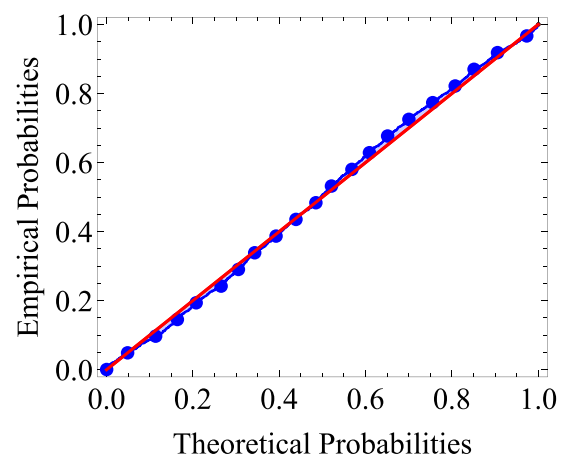
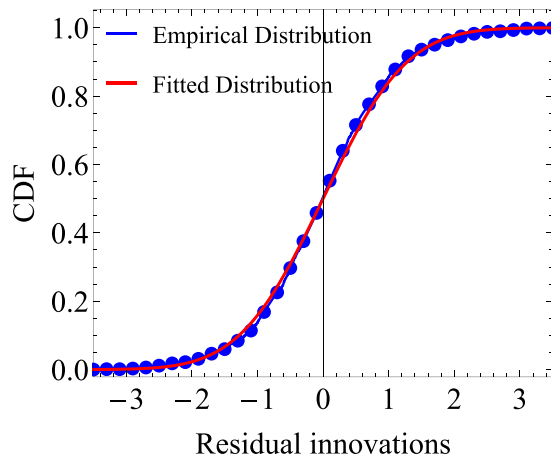
2348 As an example, in Fig. 24, we show, from top to bottom,  
 2349 the results of this analysis for the natural variability compo-  
 2350 nent of the Mean-G dataset, for its corresponding series of  
 2351 residual innovations and for the RACF. In the left, there is a  
 2352 visual comparison of the empirical cumulative distribution  
 2353 functions, CDF, (blue) to that of the respective fitted Gauss-  
 2354 ian distributions (red) and in the right the more enlighten-  
 2355 ing probability graphs where the empirical probabilities  
 2356 obtained from the graphs in the left are plotted against the  
 2357 theoretical probabilities (blue curve). The reference line  
 2358 shown in red corresponds to a perfect fit. The Kolmogorov–  
 2359 Smirnov (K–S) test can be used to create a measure  
 2360 that quantifies the behavior in probability graphs. The K–S  
 2361 test statistic is equivalent to the maximum vertical distance  
 2362 between a point in the plot and the reference line. The closer  
 2363 the points are to the reference line, the more probable is the  
 2364 data satisfies the fitted theoretical distribution.

2365 In Table 6 we summarize the standard deviations of the  
 2366 normal distributions obtained for the series of anomalies  
 2367 ( $SD_T$ ), the series of residual innovations ( $SD_{\text{innov}}$ ) and the  
 2368 RACF ( $SD_{\text{RACF}}$ ) for each dataset. The mean values of the  
 2369 distributions were very small compared to the respective  
 2370 standard deviations and they were omitted. The K–S test sta-  
 2371 tistics with the corresponding  $p$ -values are also shown. More  
 2372 powerful statistical tests for normality could be performed,  
 2373 like the Shapiro–Wilk or the Anderson–Darling tests. How-  
 2374 ever, these other tests have their own disadvantages, and,  
 2375 for the purpose of this work, the conclusions obtained from the  
 2376 K–S test to check the Gaussianity hypothesis of the original  
 2377 anomalies and the adequacy of the fGn process fit, are good  
 2378 enough.

## Natural Component, Mean-G:



## Residual Innovations:



## Residual Autocorrelation Function:

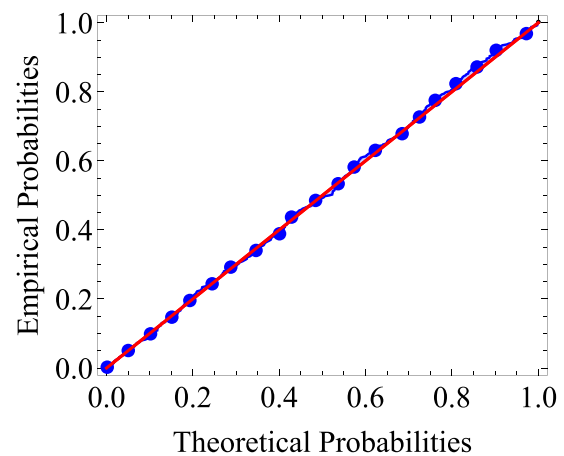
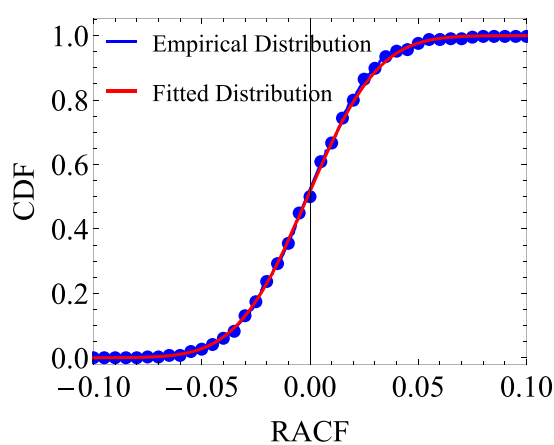


**Fig. 24** From top to bottom, graphs for the natural variability component of Mean-G dataset, for the series of residual innovations and for the RACF. In the left, a comparison of the empirical CDF's (blue line with circles) to that of the respective fitted Gaussian distributions

(red) and in the right the more detailed probability graphs where the empirical probabilities obtained from the graphs in the left are plotted against the theoretical probabilities (blue line with circles). The reference line shown in red corresponds to a perfect fit



**Table 6** Normality tests and standard deviations of the distributions obtained for the series of anomalies ( $SD_T$ ), the series of residual innovations ( $SD_{\text{innov}}$ ) and the RACF ( $SD_{\text{RACF}}$ ) for each global dataset

| Dataset | Temperature anomalies |       |           | Residual innovations |       |           | RACF               |       |           |
|---------|-----------------------|-------|-----------|----------------------|-------|-----------|--------------------|-------|-----------|
|         | $SD_T$                | K-S   | $p$ value | $SD_{\text{innov}}$  | K-S   | $p$ value | $SD_{\text{RACF}}$ | K-S   | $p$ value |
| NASA    | 0.155                 | 0.020 | 0.497     | 1.001                | 0.024 | 0.277     | 0.026              | 0.026 | 0.939     |
| NOAA    | 0.144                 | 0.029 | 0.114     | 1.000                | 0.044 | 0.003     | 0.025              | 0.033 | 0.747     |
| HAD4    | 0.159                 | 0.016 | 0.775     | 1.000                | 0.041 | 0.006     | 0.025              | 0.021 | 0.992     |
| CowW    | 0.163                 | 0.013 | 0.951     | 1.000                | 0.016 | 0.752     | 0.025              | 0.022 | 0.982     |
| Berk    | 0.174                 | 0.013 | 0.922     | 1.000                | 0.02  | 0.485     | 0.026              | 0.022 | 0.986     |
| Mean-G  | 0.153                 | 0.016 | 0.755     | 1.001                | 0.026 | 0.193     | 0.026              | 0.023 | 0.979     |
| NASA-L  | 0.371                 | 0.041 | 0.008     | 0.999                | 0.039 | 0.011     | 0.029              | 0.04  | 0.511     |
| NOAA-L  | 0.325                 | 0.040 | 0.009     | 1.000                | 0.051 | 0.000     | 0.029              | 0.063 | 0.072     |
| HAD4-L  | 0.285                 | 0.036 | 0.028     | 1.000                | 0.047 | 0.001     | 0.028              | 0.032 | 0.774     |
| CowW-L  | 0.333                 | 0.032 | 0.065     | 1.000                | 0.036 | 0.027     | 0.03               | 0.047 | 0.317     |
| Berk-L  | 0.342                 | 0.034 | 0.043     | 1.000                | 0.033 | 0.056     | 0.032              | 0.041 | 0.486     |
| Mean-L  | 0.321                 | 0.035 | 0.038     | 1.000                | 0.039 | 0.013     | 0.03               | 0.032 | 0.767     |

The mean values for each distribution were very small compared to the standard deviations and they were omitted. The K-S test statistics with the corresponding  $p$  values are also shown

**Table 7** Skill scores  $RMSE_{\text{raw}}$  and  $ACC_{\text{nat}}$  for forecast horizons  $k = 1, 3, 6$  and 12 months for the twelve datasets, including the mean series for the global and the land surface

| Dataset | Normalization factor (°C) |        |                   | $RMSE_{\text{raw}}$ (°C) |         |         |          | $ACC_{\text{nat}}$ |         |         |          |
|---------|---------------------------|--------|-------------------|--------------------------|---------|---------|----------|--------------------|---------|---------|----------|
|         | $\hat{\sigma}_T$          | $SD_T$ | $SD_{\text{raw}}$ | $k = 1$                  | $k = 3$ | $k = 6$ | $k = 12$ | $k = 1$            | $k = 3$ | $k = 6$ | $k = 12$ |
| NASA    | 0.183                     | 0.149  | 0.315             | 0.108                    | 0.128   | 0.139   | 0.148    | 0.688              | 0.515   | 0.373   | 0.218    |
| NOAA    | 0.183                     | 0.140  | 0.301             | 0.093                    | 0.113   | 0.127   | 0.137    | 0.744              | 0.587   | 0.434   | 0.264    |
| HAD4    | 0.194                     | 0.152  | 0.276             | 0.100                    | 0.120   | 0.133   | 0.145    | 0.752              | 0.612   | 0.487   | 0.340    |
| CowW    | 0.183                     | 0.158  | 0.285             | 0.107                    | 0.126   | 0.137   | 0.147    | 0.738              | 0.601   | 0.497   | 0.377    |
| Berk    | 0.197                     | 0.163  | 0.301             | 0.109                    | 0.131   | 0.142   | 0.151    | 0.741              | 0.597   | 0.497   | 0.391    |
| Mean-G  | 0.195                     | 0.147  | 0.293             | 0.098                    | 0.119   | 0.131   | 0.142    | 0.743              | 0.588   | 0.459   | 0.314    |
| NASA-L  | 0.373                     | 0.338  | 0.509             | 0.305                    | 0.327   | 0.332   | 0.333    | 0.435              | 0.257   | 0.204   | 0.174    |
| NOAA-L  | 0.331                     | 0.327  | 0.521             | 0.296                    | 0.318   | 0.324   | 0.325    | 0.429              | 0.238   | 0.167   | 0.140    |
| HAD4-L  | 0.297                     | 0.268  | 0.449             | 0.223                    | 0.248   | 0.256   | 0.261    | 0.554              | 0.375   | 0.296   | 0.239    |
| CowW-L  | 0.337                     | 0.327  | 0.503             | 0.286                    | 0.311   | 0.317   | 0.320    | 0.482              | 0.313   | 0.249   | 0.205    |
| Berk-L  | 0.348                     | 0.331  | 0.506             | 0.293                    | 0.318   | 0.325   | 0.326    | 0.462              | 0.277   | 0.206   | 0.168    |
| Mean-L  | 0.327                     | 0.312  | 0.492             | 0.274                    | 0.299   | 0.305   | 0.307    | 0.476              | 0.293   | 0.224   | 0.184    |

The values  $MSSS_{\text{nat}}$  and  $MSSS_{\text{raw}}$  can be obtained from Eqs. (34) taking  $MSE = RMSE^2$  and the respective  $MSE_{\text{ref}} = SD_T^2$  or  $MSE_{\text{ref}} = SD_{\text{raw}}^2$ . The values of  $\hat{\sigma}_T$ , were included for reference

2379 The values of  $SD_T$  are the same shown previously in  
 2380 Table 5. As expected from the theory,  $SD_{\text{innov}} = 1$  for all  
 2381 dataset and the values obtained for  $SD_{\text{RACF}}$  are close to  
 2382 the theoretical value  $1/\sqrt{N} = 0.025$  ( $N = 1656$ ). With the  
 2383 exceptions of the residual innovations of NOAA and HAD4  
 2384 for the global datasets, the  $p$ -values are above 0.05, so there  
 2385 is not enough evidence to reject normality at that level.  
 2386 Moreover, the  $p$ -values obtained are, in general, larger than  
 2387 those obtained for series of the same length based on pseu-  
 2388 dorandom number generators [for a numerical experiment  
 2389 using 10000 samples, the  $p$ -values were uniformly distrib-  
 2390 uted in the range (0–1)]. For the land surface datasets, the  
 2391  $p$ -values for the temperature anomalies and the innovations

2392 are low and a different distribution for the white noise inno-  
 2393 vations could be proposed.

2394 As we mentioned before, the normality of the innova-  
 2395 tions is less important to confirm the adequacy of the model  
 2396 than its whiteness, which is confirmed by the Gaussianity  
 2397 of the RACF in all cases (see the large  $p$ -values in the last  
 2398 column of Table 6). A main deviation from normal behav-  
 2399 ior is the existence of extremes in the original data. This  
 2400 “fat-tailed” property of the probability distributions was evi-  
 2401 denced in Lovejoy (2014) in a paper of statistical hypothesis  
 2402 testing of anthropogenic warming. In the present work, it  
 2403 does not have major implications or compromise the appli-  
 2404 cability of the model to the global data.

## 2405 Appendix 3: Forecast and validation for all 2406 datasets

2407 Some results of the hindcast validation are summarized in  
2408 Table 7 for the twelve datasets, including the mean series  
2409 for the global and the land surface. Only the error,  $RMSE_{nat}$ ,  
2410 and the  $ACC_{nat}$ , for the natural variability component were  
2411 presented for horizons  $k = 1, 3, 6$  and 12 months. The val-  
2412 ues  $MSSS_{nat}$  and  $MSSS_{raw}$  can be obtained from Eq. (34)  
2413 taking  $MSE = RMSE^2$  and the respective  $MSE_{ref} = SD_T^2$  or  
2414  $MSE_{ref} = SD_{raw}^2$ . Also, we can use the values of  $ACC_{nat}$  to  
2415 obtain very good approximations of  $MSSS_{nat}$  for these hori-  
2416 zons thanks to the relationship  $MSSS_{nat} \approx ACC_{nat}^2$  (Eq. (38)).  
2417 Only the spurious values of  $ACC_{raw}$  cannot be obtained from  
2418 this table, but it is worth mentioning that, even for  $k = 12$   
2419 months, they are higher than 0.75 for all datasets. Notice  
2420 the large difference between the values of  $SD_T$  and  $SD_{raw}$ ,  
2421 for the detrended and the raw anomalies respectively, due to  
2422 the presence of the anthropogenic trend. The values of  $\hat{\sigma}_T$ ,  
2423 were included for reference.

## 2424 References

- 2425 Baillie RT, Chung S-K (2002) Modeling and forecasting from trend-  
2426 stationary long memory models with applications to climatol-  
2427 ogy. *Int J Forecast* 18:215–226. [https://doi.org/10.1016/S0169-](https://doi.org/10.1016/S0169-2070(01)00154-6)  
2428 [-2070\(01\)00154-6](https://doi.org/10.1016/S0169-2070(01)00154-6)
- 2429 Berkeley Earth (2018) Land + Ocean (1850–Recent). <http://berkeleyearth.org/data/>. Accessed 21 May 2018
- 2430 Berner J, Achatz U, Batté L et al (2017) Stochastic parameterization:  
2431 toward a new view of weather and climate models. *Bull Am Meteorol Soc* 98:565–588. [https://doi.org/10.1175/BAMS-D-15-00268](https://doi.org/10.1175/BAMS-D-15-00268.1)  
2432 [.1](https://doi.org/10.1175/BAMS-D-15-00268.1)
- 2433 Biagini F, Hu Y, Øksendal B, Zhang T (2008) Stochastic calculus for  
2434 fractional brownian motion and applications. Springer, London
- 2435 Blender R, Fraedrich K, Hunt B (2006) Millennial climate variability:  
2436 GCM-simulation and Greenland ice cores. *Geophys Res Lett* 33:L04710. <https://doi.org/10.1029/2005GL024919>
- 2437 CanSIPS (2016) CanSIPS data in GRIB2 format. [https://weather.gc.ca/grib/grib2\\_cansips\\_e.html](https://weather.gc.ca/grib/grib2_cansips_e.html). Accessed 16 Feb 2016
- 2438 Cowtan K, Way RG (2014) Coverage bias in the HadCRUT4 temper-  
2439 ature series and its impact on recent temperature trends. *Q J R Meteorol Soc* 140:1935–1944. <https://doi.org/10.1002/qj.2297>
- 2440 Cowtan and Way (2018) Coverage bias in the HadCRUT4 temperature  
2441 record. <http://www-users.york.ac.uk/~kdc3/papers/coverage2013/series.html>. Accessed 21 May 2018
- 2442 Crochemore L, Ramos M-H, Pappenberger F (2016) Bias correcting  
2443 precipitation forecasts to improve the skill of seasonal stream-  
2444 flow forecasts. *Hydrol Earth Syst Sci* 20:3601–3618. <https://doi.org/10.5194/hess-20-3601-2016>
- 2445 Franzke C (2012) Nonlinear trends, long-range dependence, and cli-  
2446 mate noise properties of surface temperature. *J Clim* 25:4172–  
2447 4183. <https://doi.org/10.1175/JCLI-D-11-00293.1>
- 2448 Franzke CLE, O’Kane TJ, Berner J et al (2014) Stochastic climate  
2449 theory and modeling. *Wiley Interdiscip Rev Clim Chang* 6:63–78.  
2450 <https://doi.org/10.1002/wcc.318>
- 2451 Garcia LE, Dawdy DR, Mejia JM (1972) Long memory monthly  
2452 streamflow simulation by a broken line model. *Water Resour Res* 8:1100–1105. <https://doi.org/10.1029/WR008i004p01100>

- GISTEMP Team (2018) GISS Surface Temperature Analysis (GIS-  
2461 TEMP). NASA Goddard Institute for Space Studies. <https://data.giss.nasa.gov/gistemp/>. Accessed 21 May 2018  
2462
- Gleason B, Williams C, Menne M, Lawrimore J (2015) GHCN-M  
2463 Technical Report No. GHCNM-15-01 Modifications to GHCN-  
2464 Monthly (version 3.3.0) and USHCN (version 2.5.5) processing  
2465 systems. Asheville, NC  
2466
- Gneiting T, Raftery AE, Westveld AH, Goldman T (2005) Calibrated  
2467 probabilistic forecasting using ensemble model output statistics  
2468 and minimum CRPS estimation. *Mon Weather Rev* 133:1098–  
2469 1118. <https://doi.org/10.1175/MWR2904.1>  
2470
- Gripenberg G, Norros I (1996) On the prediction of fractional brownian  
2471 motion. *J Appl Probab* 33:400–410. <https://doi.org/10.2307/3215063>  
2472
- Hansen J, Ruedy R, Sato M, Lo K (2010) Global surface temperature  
2473 change. *Rev Geophys* 48:RG4004. <https://doi.org/10.1029/2010rg000345>  
2474
- Hasselmann K (1976) Stochastic climate models Part I. Theory. *Tellus*  
2475 28:473–485. <https://doi.org/10.1111/j.2153-3490.1976.tb00696.x>  
2476
- Hébert R, Lovejoy S, Tremblay B (2019) An observation-based scaling  
2477 model for climate sensitivity estimates and global projections to  
2478 2100. *Clim Dyn* (under review)  
2479
- Hersbach H (2000) Decomposition of the continuous ranked prob-  
2480 ability score for ensemble prediction systems. *Weather Forecast*  
2481 15:559–570. [https://doi.org/10.1175/1520-0434\(2000\)015%3c0559:DOTCRP%3e2.0.CO;2](https://doi.org/10.1175/1520-0434(2000)015%3c0559:DOTCRP%3e2.0.CO;2)  
2482
- Hipel KW, McLeod AI (1994) Time series modelling of water resources  
2483 and environmental systems, 1st edn. Elsevier, Amsterdam  
2484
- Huybers P, Curry W (2006) Links between annual, Milankovitch and  
2485 continuum temperature variability. *Nature* 441:329  
2486
- Jeong H-DJ, Pawlikowski K, McNickle DC (2003) Generation of  
2487 self-similar processes for simulation studies of telecommunica-  
2488 tion networks. *Math Comput Model* 38:1249–1257. [https://doi.org/10.1016/S0895-7177\(03\)90127-0](https://doi.org/10.1016/S0895-7177(03)90127-0)  
2489
- Keller JD, Hense A (2011) A new non-Gaussian evaluation  
2490 method for ensemble forecasts based on analysis rank histo-  
2491 grams. *Meteorol Zeitschrift* 20:107–117. <https://doi.org/10.1127/0941-2948/2011/0217>  
2492
- Kharin VV, Zwiers FW (2003) Improved seasonal probability fore-  
2493 casts. *J Clim* 16:1684–1701. [https://doi.org/10.1175/1520-0442\(2003\)016%3c1684:ISPF%3e2.0.CO;2](https://doi.org/10.1175/1520-0442(2003)016%3c1684:ISPF%3e2.0.CO;2)  
2494
- Kharin VV, Teng Q, Zwiers FW et al (2009) Skill assessment of sea-  
2495 sonal hindcasts from the Canadian historical forecast project.  
2496 *Atmos Ocean* 47:204–223. <https://doi.org/10.3137/AO1101.2009>  
2497
- Kharin VV, Merryfield WJ, Boer GJ, Lee W-S (2017) A postprocess-  
2498 ing method for seasonal forecasts using temporally and spatially  
2499 smoothed statistics. *Mon Weather Rev* 145:3545–3561. <https://doi.org/10.1175/MWR-D-16-0337.1>  
2500
- Koscielny-Bunde E, Bunde A, Havlin S et al (1998) Indication of a  
2501 universal persistence law governing atmospheric variability. *Phys Rev Lett* 81:729–732. <https://doi.org/10.1103/PhysRevLett.81.729>  
2502
- Lettenmaier DP, Burges SJ (1977) Operational assessment of hydro-  
2503 logic models of long-term persistence. *Water Resour Res* 13:113–  
2504 124. <https://doi.org/10.1029/WR013i001p0113>  
2505
- Lorenz EN (1963) Deterministic nonperiodic flow. *J Atmos Sci* 20:130–141. [https://doi.org/10.1175/1520-0469\(1963\)020%3c0130:DNF%3e2.0.CO;2](https://doi.org/10.1175/1520-0469(1963)020%3c0130:DNF%3e2.0.CO;2)  
2506
- Lorenz EN (1972) Predictability; does the flap of a butterfly’s wings in  
2507 Brazil set off a tornado in Texas? Presented before the American  
2508 Association for the Advancement of Science, December 29, 1972.  
2509 [http://eaps4.mit.edu/research/Lorenz/Butterfly\\_1972.pdf](http://eaps4.mit.edu/research/Lorenz/Butterfly_1972.pdf)  
2510
- Lovejoy S (2014) Scaling fluctuation analysis and statistical hypothesis  
2511 testing of anthropogenic warming. *Clim Dyn* 42:2339–2351. <https://doi.org/10.1007/s00382-014-2128-2>  
2512  
2513  
2514  
2515  
2516  
2517  
2518  
2519  
2520  
2521  
2522  
2523  
2524

- 2525 Lovejoy S (2015) Using scaling for macroweather forecasting including the pause. *Geophys Res Lett* 42(17):7148–7155. <https://doi.org/10.1002/2015GL065665>
- 2526
- 2527 Lovejoy S (2017) How accurately do we know the temperature of the surface of the earth? *Clim Dyn* 49:4089–4106. <https://doi.org/10.1007/s00382-017-3561-9>
- 2528
- 2529 Lovejoy S, de Lima MIP (2015) The joint space-time statistics of macroweather precipitation, space-time statistical factorization and macroweather models. *Chaos An Interdiscip J Nonlinear Sci* 25:075410. <https://doi.org/10.1063/1.4927223>
- 2530
- 2531 Lovejoy S, Schertzer D (2012) Low-frequency weather and the emergence of the climate. *Extrem Events Nat Hazards Complex Perspect* 196:231–254
- 2532
- 2533 Lovejoy S, Schertzer D (2013) The weather and climate: emergent laws and multifractal cascades. Cambridge University Press, Cambridge
- 2534
- 2535 Lovejoy S, Schertzer D, Varon D (2013) Do GCMs predict the climate... or macroweather? *Earth Syst Dyn* 4:439–454. <https://doi.org/10.5194/esd-4-439-2013>
- 2536
- 2537 Lovejoy S, del Rio Amador L, Hébert R (2015) The ScaLIng Macroweather Model (SLIMM): using scaling to forecast global-scale macroweather from months to decades. *Earth Syst Dyn* 6:637–658. <https://doi.org/10.5194/esd-6-637-2015>
- 2538
- 2539 Lovejoy S, Del Rio Amador L, Hébert R (2018) Harnessing butterflies: theory and practice of the stochastic seasonal to interannual prediction system (StocSIPS) BT. In: Tsonis AA (ed) *Advances in nonlinear geosciences*. Springer, Cham, pp 305–355
- 2540
- 2541 Mandelbrot BB (1971) A fast fractional gaussian noise generator. *Water Resour Res* 7:543–553. <https://doi.org/10.1029/WR007i003p00543>
- 2542
- 2543 Mandelbrot BB (1972) Broken line process derived as an approximation to fractional noise. *Water Resour Res* 8:1354–1356. <https://doi.org/10.1029/WR008i005p01354>
- 2544
- 2545 Mandelbrot BB, Van Ness JW (1968) Fractional Brownian motions, fractional noises and applications. *SIAM Rev* 10:422–437. <https://doi.org/10.1137/1010093>
- 2546
- 2547 Mandelbrot BB, Wallis JR (1969) Computer Experiments with fractional gaussian noises: part 3, mathematical appendix. *Water Resour Res* 5:260–267. <https://doi.org/10.1029/WR005i001p00260>
- 2548
- 2549 Matalas NC, Wallis JR (1971) Statistical properties of multivariate fractional noise processes. *Water Resour Res* 7:1460–1468. <https://doi.org/10.1029/WR007i006p01460>
- 2550
- 2551 Meinshausen M, Smith SJ, Calvin K et al (2011) The RCP greenhouse gas concentrations and their extensions from 1765 to 2300. *Clim Change* 109:213–241. <https://doi.org/10.1007/s10584-011-0156-z>
- 2552
- 2553 Mejia JM, Rodriguez-Iturbe I, Dawdy DR (1972) Streamflow simulation: 2. The broken line process as a potential model for hydrologic simulation. *Water Resour Res* 8:931–941. <https://doi.org/10.1029/WR008i004p00931>
- 2554
- 2555 Merryfield WJ, Bertrand D, Fontecilla J-S et al (2011) The Canadian Seasonal to Interannual Prediction System (CanSIPS)—an overview of its design and operational implementation—technical Note
- 2556
- 2557 Merryfield WJ, Lee W-S, Boer GJ et al (2013) The Canadian Seasonal to Interannual Prediction System. Part I: models and initialization. *Mon Weather Rev* 141:2910–2945. <https://doi.org/10.1175/MWR-D-12-00216.1>
- 2558
- 2559 Met Office Hadley Centre (2018) Met Office Hadley Centre observations datasets. <http://www.metoffice.gov.uk/hadobs/hadcrut4/data/current/download.html>. Accessed 21 May 2018
- 2560
- 2561 Morice CP, Kennedy JJ, Rayner NA, Jones PD (2012) Quantifying uncertainties in global and regional temperature change using an ensemble of observational estimates: the HadCRUT4 data set. *J Geophys Res Atmos*. <https://doi.org/10.1029/2011jd017187>
- 2562
- 2563 Newman M, Sardeshmukh PD, Winkler CR, Whitaker JS (2003) A study of subseasonal predictability. *Mon Weather Rev* 131:1715–1732. <https://doi.org/10.1175/2558.1>
- 2564
- 2565 NOAA-NCEI (2018) Global Surface Temperature Anomalies. NOAA National Center for Environmental Information. <https://www.ncdc.noaa.gov/monitoring-references/faq/anomalies.php>. Accessed 21 May 2018
- 2591
- 2592
- 2593
- 2594
- 2595 Norros I (1995) On the use of fractional Brownian motion in the theory of connectionless networks. *IEEE J Sel Areas Commun* 13:953–962. <https://doi.org/10.1109/49.400651>
- 2596
- 2597 O’Connell PE (1974) Stochastic modelling of long-term persistence in streamflow sequences. Doctoral Thesis. Imperial College, London
- 2598
- 2599 Palma W (2007) Long-memory time series. Wiley, Hoboken
- 2600
- 2601 Palmer T, Buizza R, Hagedorn R et al (2006) Ensemble prediction: a pedagogical perspective. *ECMWF News1* 2:10–17. <https://doi.org/10.21957/ab129056ew>
- 2602
- 2603 Papoulis A, Pillai SU (2002) Probability, random variables and stochastic processes, 4th edn. McGraw-Hill, New York
- 2604
- 2605 Pasternack A, Bhend J, Liniger MA et al (2018) Parametric decadal climate forecast recalibration (DeFoReSt 1.0). *Geosci Model Dev* 11:351–368. <https://doi.org/10.5194/gmd-11-351-2018>
- 2606
- 2607 Paxson V (1997) Fast, approximate synthesis of fractional Gaussian noise for generating self-similar network traffic. *ACM SIGCOMM Comput Commun Rev* 27:5–18. <https://doi.org/10.1145/269790.269792>
- 2608
- 2609 Penland C, Matrosova L (1994) A balance condition for stochastic numerical models with application to the El Niño–Southern oscillation. *J Clim* 7:1352–1372. [https://doi.org/10.1175/1520-0442\(1994\)007%3c1352:ABCFNS%3e2.0.CO;2](https://doi.org/10.1175/1520-0442(1994)007%3c1352:ABCFNS%3e2.0.CO;2)
- 2610
- 2611 Penland C, Sardeshmukh PD (1995) The optimal growth of tropical sea surface temperature anomalies. *J Clim* 8:1999–2024. [https://doi.org/10.1175/1520-0442\(1995\)008%3c1999:TOGOT%3e2.0.CO;2](https://doi.org/10.1175/1520-0442(1995)008%3c1999:TOGOT%3e2.0.CO;2)
- 2612
- 2613 Rodriguez-Iturbe I, Mejia JM, Dawdy DR (1972) Streamflow Simulation: 1. A new look at Markovian Models, fractional Gaussian noise, and Crossing Theory. *Water Resour Res* 8:921–930. <https://doi.org/10.1029/WR008i004p00921>
- 2614
- 2615 Rohde R, Muller RA, Jacobsen R et al (2013) A new estimate of the average earth surface land temperature spanning 1753 to 2011. *Geoinform Geostat Overv*. <https://doi.org/10.4172/2327-4581.1000101>
- 2616
- 2617 Rypdal K, Østvang L, Rypdal M (2013) Long-range memory in Earth’s surface temperature on time scales from months to centuries. *J Geophys Res Atmos* 118:7046–7062. <https://doi.org/10.1002/jgrd.50399>
- 2618
- 2619 Sardeshmukh PD, Sura P (2009) Reconciling non-Gaussian climate statistics with linear dynamics. *J Clim* 22:1193–1207. <https://doi.org/10.1175/2008JCLI2358.1>
- 2620
- 2621 Smith TM, Reynolds RW, Peterson TC, Lawrimore J (2008) Improvements to NOAA’s historical merged land-ocean surface temperature analysis (1880–2006). *J Clim* 21:2283–2296. <https://doi.org/10.1175/2007JCLI2100.1>
- 2622
- 2623 Stanski HR, Wilson LJ, Burrows WR (1989) Survey of common verification methods in meteorology. WWO Tech. Rep. 8, WMO/TD 358. Ontario
- 2624
- 2625 Van Schaeybroeck B, Vannitsem S (2018) Postprocessing of long-range forecasts. *Statistical postprocessing of ensemble forecasts*. Elsevier, Oxford, pp 267–290
- 2626
- 2627 Winkler CR, Newman M, Sardeshmukh PD (2001) A linear model of wintertime low-frequency variability. Part I: formulation and forecast skill. *J Clim* 14:4474–4494. [https://doi.org/10.1175/1520-0442\(2001\)014%3c4474:ALMOWL%3e2.0.CO;2](https://doi.org/10.1175/1520-0442(2001)014%3c4474:ALMOWL%3e2.0.CO;2)
- 2628
- 2629 Wold H (1938) A study in the analysis of stationary time series. Almqvist und Wiksell, Uppsala
- 2630
- 2631 Yuan N, Fu Z, Liu S (2015) Extracting climate memory using fractional integrated statistical model: a new perspective on climate prediction. *Sci Rep* 4:6577. <https://doi.org/10.1038/srep06577>
- 2632
- 2633
- 2634
- 2635
- 2636
- 2637
- 2638
- 2639
- 2640
- 2641
- 2642
- 2643
- 2644
- 2645
- 2646
- 2647
- 2648
- 2649
- 2650
- 2651
- 2652
- 2653
- 2654
- 2655